Investigations of Reduced Equations for Rotating, Stratified and Non-hydrostatic Flows

by

David J. Nieves

B.A., University of Minnesota Morris, 2010

M.S., University of Colorado Boulder, 2013

A thesis submitted to the

Faculty of the Graduate School of the

University of Colorado in partial fulfillment

of the requirements for the degree of

Doctor of Philosophy

Department of Applied Mathematics

2016

This thesis entitled:
Investigations of Reduced Equations for Rotating, Stratified and Non-hydrostatic Flows
written by David J. Nieves
has been approved for the Department of Applied Mathematics

_____

Keith Julien

_____

Prof. Ian Grooms

_____

Prof. Bengt Fornberg

_____

Prof. Mark Hoefer

_____

Prof. Jeffrey Weiss

Date _____

The final copy of this thesis has been examined by the signatories, and we find that both the content and the form meet acceptable presentation standards of scholarly work in the above mentioned discipline.

Nieves, David J. (Ph.D., Applied Mathematics)

Investigations of Reduced Equations for Rotating, Stratified and Non-hydrostatic Flows

Thesis directed by Prof. Keith Julien

This thesis is a collection of studies concerning an asymptotically reduced equation set derived from the Boussinesq approximation describing rotationally constrained geophysical flow.

The first investigation is concerned with a statistical identification of coherent and long-lived structures in rotationally constrained Rayleigh-Bénard convection. Presently, physical laboratory limitations challenge experimentalists while spatio-temporal resolution requirements challenges numericists performing direct numerical simulations of the Boussinesq equations. These challenges prevent an exhaustive analysis of the flow morphology in the rapid rotating limit. In this study the flow morphologies obtained from simulations of the reduced equations are investigated from a statistical perspective. Auto- and cross-correlations are computed from temporal and spatial signals that synthesize experimental data that may be obtained in laboratory experiments via thermistor measurements or particle image velocimetry. The statistics used can be employed in laboratory experiments to identify regime transitions in flow morphology, capture radial profiles of coherent structures, and extract transport properties belonging to these structures. These results provide a foundation for comparison and a measure for understanding the extent to which rotationally constrained regime has been accessed by laboratory experiments and direct numerical simulations.

A related study comparing the influence of fixed temperature and fixed heat flux thermal boundary conditions on rapidly rotating convection in the plane layer geometry is also investigated and briefly summarized for the case of stress-free mechanical boundary conditions. It is shown that the difference between these thermal boundary conditions on the interior geostrophically balanced convection is asymptotically weak. Through a simple rescaling of thermal variables, the leading order reduced system is shown to be equivalent for both thermal boundary conditions. These results imply that any horizontal thermal variation along the boundaries that varies on the scale

of the convection has no leading order influence on the interior convection, thus providing insight into geophysical and astrophysical flows where stress-free mechanical boundary conditions are often assumed.

The final study presented here contrasts the previous investigations. It presents an investigation of rapidly rotating and *stably* stratified turbulence where the stratification strength is varied from weak (large Froude number) to strong (small Froude number). The investigation is set in the context of the asymptotically reduced model which efficiently retains anisotropic inertia-gravity waves with order-one frequencies and highlights a regime of wave-eddy interactions. Numerical simulations of the reduced model are performed where energy is injected by a stochastic forcing of vertical velocity. The simulations reveal two regimes: one characterized by the presence of well-formed, persistent and thin turbulent layers of locally-weakened stratification: the other characterized by the absence of layers at large Froude numbers. Both regimes are characterized by a large-scale barotropic dipole in a sea of small-scale turbulence. When the Reynolds number is not too large a direct cascade of barotropic kinetic energy is observed and leads to an equilibration of total energy. We examine net energy exchanges that occur through vortex stretching and vertical buoyancy flux and diagnose the horizontal scales active in these exchanges. We find that baroclinic motions inject energy directly to the largest scales of the barotropic mode governed by the two-dimensional vorticity equation, and implies that the large-scale barotropic dipole is not the end result of an inverse cascade within the two-dimensional barotropic mode. An additional yet brief look into the linear vortical and wave modes is considered.

Dedication

To my Mother, and wife Alaina ... and Stella

Acknowledgements

I owe thanks to the many people who have given their support over the last few years. I owe a special thanks to my advisor Dr. Keith Julien for sharing his expertise in geophysical fluids. In addition to many research lessons, he has provided helpful advice regarding my career and has been generous in allowing me to finish my thesis work from Washington, D.C. For this I am forever thankful. I also want to thank my committee members for their constructive criticisms. Thanks to Bengt Fornberg, Dr. Jeffrey Weiss for his continued input on the stable layer problem, to Dr. Annick Pouquet for her insights and guidance especially during my time at IPAM, and to Mark Hoefer for his energizing encouragement. I also owe particular thanks to Ian Grooms for his perceptive and instructive collaboration.

I would also like to thank Antonio Rubio who was extraordinarily helpful as well as patient in aiding me in the process of learning the functionality of the code used to perform our research and Joe Werne for his help with some of the detailed aspects of the code. I owe thanks to Jon Aurnou for opening up his laboratory at UCLA and sharing his experimental studies of Rayleigh-Bénard convection. I owe thanks to Michael Calkins, Philippe Marti, and Ben Miquel for insightful discussions on various mathematical and fluid dynamical problems.

I would like to thank all the applied math staff for their hard work. Without them certainly nothing would be accomplished. I would like to thank Anne Dougherty for all her hard work, providing me the opportunity to teach a summer course, and for all her great teaching and career advice.

I owe a special thanks to fellow past/present graduate students Tony Wong, Nate Monnig,

Contents

Chapter

Figures

Figure

Chapter 1

Introduction

The dynamical processes characterizing atmospheric and oceanic flow span an enormous range of scales: from the smallest scales at which kinematic viscosity dissipates fluid motion, to intermediate scales (or mesoscale) on which weather systems exist, and finally to the largest scales (or synoptic scales) over which slowly evolving geostrophically balanced flow endure. This picture of geophysical flows, as just described, is not entirely distinguishable from two or three dimensional turbulence where fluid motions also inhabit a vast range of temporal and spatial scales. While homogeneous two- and three-dimensional flows are dominated by nonlinear effects and are observed to vary unpredictably, the same may also be said of geophysical flows. However, it is the additional dynamical constraints imposed by the introduction planetary rotation and density stratification that characterize the nature of geophysical flows. The presence of such constraining effects provides a degree of simplification in the sense that flows tend to organize into coherent and oftentimes long-lived structures; embedding physical features not present in homogeneous three-dimensional turbulence. Therefore, the effects of rotation and stratification may be exploited for the purposes of gaining insight into the fundamental features of geophysical fluid dynamics.

Beyond the scope of planetary atmospheres and oceans, system rotation and density stratification are ubiquitous features in our universe. In fact, these effects are suspected to play a significant role in remote objects within our galaxy (and others) called protoplanetary accretion disks. These are rotating sheet-like structures comprised of cold gas that typically surround young stars. Within these disks fluid turbulence is suspected to contribute significantly to the evolution of

accretion disks. While not well-understood, it is believed that planet formation is due to the combined effects of turbulent motions and gravitational forces that result in accretion of disk material to form planetismals. Indeed, our solar system is believed to evolved from such beginnings.

Additionally, effects of system rotation and density stratification play a role in stellar and planetary interiors. For example, Earth's iron-rich liquid outer core is constrained by effects of rotation and is likely convectively driven by thermo-chemical buoyancy forces resulting in interior dynamics responsible for Earth's geomagnetic field and self-sustaining dynamo (see figure 1.1(a)). Observational data of the radial component Earth's magnetic field serves as a proxy to visualizing the core's convecting flow. At present, in addition to these observations another method by which core convection is studied occurs through the numerical simulation of the equations for convectively-driven magnetohydrodynamic induction. The ensuing flow that develops in numerical simulations is axially-aligned and columnar, bearing resemblance to non-magnetic rapidly rotating Rayleigh-Bénard convection (see figure 1.1(b)). This qualitative similarity to core convection is one inspiration for a detailed study of rapidly rotating convection. However, a major challenge resides in attaining realistic parameters defining planetary interior core convection. For example, if one wishes to simulate Earth's core then the appropriate parameters are orders of magnitude above and beyond what can be reasonably accomplished using physical experimentation and direct numerical simulation of the governing equations. To illustrate, approximate values for the Ekman number, Rayleigh number, and the Reynolds number for Earth's core are $\sim 10^{-15}$, $\sim 10^{25}$, and $\sim 10^8$, respectively. While the values for the Ekman number, Rayleigh number, and the Reynolds number that can be obtained in laboratory experiments are merely $\gtrsim 10^{-8}$, $\lesssim 10^{13}$, and $\lesssim 10^5$ (presently, direct numerical simulations struggle to attain these experimental values). This elucidates the severe deficiencies in our ability to realistically study core convection by artificial methods. However, within the class of methods used to study core convection (.e.g. laboratory experimentation and numerical simulation) reduced asymptotic models have distinguished advantages both numerically and theoretically. For the reduced model studied here, attainable values for the Ekman number, Rayleigh number, and the Reynolds number are $\lesssim 10^{-5}$, $\lesssim 20Ra_c$, and $\lesssim 20E^{-1/3}$, where E is the

(a) (b)
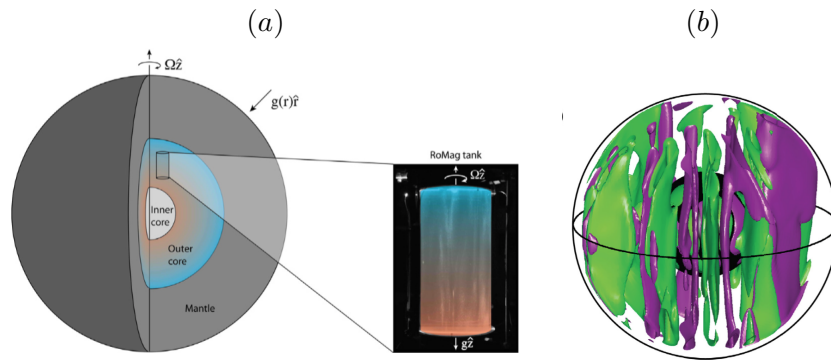
Figure 1.1: Figure (a) gives a schematic of Earth's interior (left) and a laboratory experiment of rotating convection (right). The outer core is shaded with regions of red and blue to illustrate the thermal gradient responsible for driving convective motions. Figure (b) shows isosurfaces of vertical vorticity $\zeta = \hat{\boldsymbol{z}} \cdot \nabla \times \boldsymbol{u}$ in the outer core taken from numerical simulations by Soderlund et al. (2012) where the thermal forcing is twice the critical value required for the onset of convection ($Ra = 1.9Ra_c$) and the rotation rate is parameterized by the nondimensional Ekman number ($E = 10^{-4}$).

Ekman number and Ra_c represents a critical value at which convective motions begin. Clearly if E is a small parameter then the system that may be represented by the reduced model more closely resembles realistic core-convection parameters for Earth's interior.

Examples of geophysical fluid constrained by rotation and influenced by thermal forcing are also present in Earth's oceans. Normally the ocean surface (depths down to 1km) is strongly stratified, that is, a sharp vertical density gradient exists (called the thermocline) inhibiting vertical mixing with and insulating the ocean abyss (see figure 1.2). However, observations of regions in the Atlantic ocean (Labrador and Greenland Seas, in particular) have found the strongly density stratified thermocline to lose surface buoyancy to cold atmospheric conditions in the winter, resulting in an ocean surface that is prone to mixing with deep ocean waters. When ocean surface temperatures cool the process of mixing occurs as convection and extends to great depths, placing an emphasis on locally (or small horizontal scale) non-hydrostatic effects. Characteristics of this deep-convection include buoyancy timescales that are long compared to planetary rotation and horizontal scales that are near a state of geostrophic balance. We may further question the resulting dynamics of the ocean abyss (forced by convective mixing with surface waters) once the insulting effects of surface stratification recovers and the the ocean layer restratifies. Observations by the World Ocean Circulation Experiment show abyssal oceans to be only weakly stratified and bring into question the dynamics of such a layer (see figure 1.2). This differs from from what is observed in the atmosphere and ocean surface where stratification effects dominate over effects due to planetary rotation. However, the extent to which scientific inquiry has probed abyssal ocean dynamics does not compare to the somewhat mature understanding of the ocean surface. If deep oceans, like waters at the ocean surface, retain dynamics with timescales long enough to be affected by Earth's rotation then interesting interactions occur between slow internal waves and eddies (the topic of investigation in §3).

These physically relevant examples in which system rotation plays a significant role in constraining the motions of geophysical fluids is the focus of this thesis. Geophysical phenomena, as we have seen, are also influenced by the effects of density stratification, and may come in two
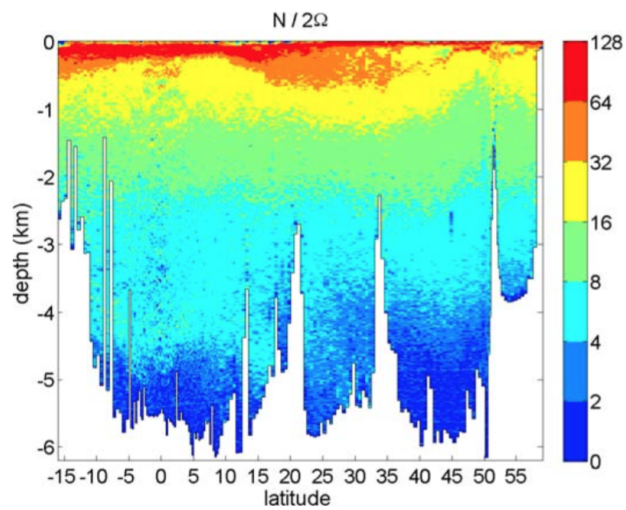
Figure 1.2: A map of the ratio of N/f conveying the relative importance of density stratification to planetary rotation as given by Nikurashin and Vallis (2011). The map illustrates the significance of stratification over rotation near the ocean surface and, in contrast, the dominance of system rotation over stratification in the ocean abyss.

forms: (i) stable stratification and (ii) unstable stratification. The former is suitable in modeling the behavior of, for example, synoptic-scale atmospheric and oceanic motions which are on average near a state of hydrostatic balance. The hydrostatic approximation is taken in the classical quasi-geostrophic (QG) equations, however, we have seen that small horizontal scale ocean dynamics are inherently non-hydrostatic, however near a state geostrophic balance, therefore with increasing interest in smaller scale ocean dynamics non-hydrostatic effects must also play an increased role. The scenario of an unstably stratified plane-layer fluid is useful in describing thermally-driven convective phenomena, and therefore clearly non-hydrostatic. A classical and canonical framework used to study such convective phenomena is referred to as the Rayleigh-Bénard convection problem, named in recognition of Henri Bénard for his experiments illuminating thermal instability and the theoretical foundations provided by Lord Rayleigh (for which the nondimensional number is named). Therefore, in addition to the dominant role of rotation the focus here is on these two very different stratification frameworks: (i) rapidly rotating and stably stratified flows and (ii) rapidly rotating Rayleigh-Bénard convection. In both frameworks a priority is given to non-hydrostatic motions which, admittedly, seems at odds with a model that is simultaneously as labeled quasi-geostrophic. This point of conflict is a non-issue and stems from the association of the classical quasi-geostrophic equations with an assumed state of hydrostatic balance. This point is discussed (and hopefully clarified) again in §3.2.1 where we consider the consequences of rapid rotation for non-hydrostatic flow.

1.1 Preliminaries

Before presenting the investigations of each particular framework (stable layer or convective layer) the general mathematical equations governing the fluid motions are presented. No attempt is made to detail specifics regarding stratification stability. The main purpose here is to introduce definitions for nondimensional flow parameters. In the chapters discussing investigations of either framework the appropriate definitions (or amendments to definitions) will be given and will largely pertain to the choice of scales characteristic to the working fluid. Additionally, the obvious choice

regarding stratification stability is made clear for each of the investigations presented. Upon describing the Boussinesq equations a summary of the reduced equations is given and their detailed asymptotic derivation is provided in the appendix. This will be the starting point for chapters on rapidly rotating Rayleigh-Bénard convection and stably stratified and rapidly rotating turbulence.

1.1.1   Equations of motion

We consider an incompressible fluid subject to an imposed constant gravitational field $\boldsymbol{g} = -g\hat{\boldsymbol{z}}$ and system rotation with constant angular velocity $\boldsymbol{\Omega} = \Omega\hat{\boldsymbol{z}}$. Here, there is no attempt to generalize the problem to one in which the axis of system rotation is not aligned with the gravitational force, however, such a generalization would result in a modified vertical momentum, tilted dynamics aligned with the rotation axis, and a modification to the linear dispersion relation (Gerkema et al., 2008; Julien et al., 2006). The fluid is stratified in the vertical with an ambient density profile $\hat{\rho}^*(z^*) = \rho_0^* + \delta\hat{\rho}^*(z^*)$ consisting of a constant reference density ρ_0^* and a vertical density variation profile $\delta\hat{\rho}^*(z^*)$ occurring over characteristic scale height H^* (where asterisks denote dimensional quantities). The total buoyancy of a fluid parcel is given by

$$\mathrm{b}^* = -\frac{g}{\rho_0^*}(\rho_0^* + \delta\hat{\rho}^*(z^*)) + b^{*\prime}(\boldsymbol{x}^*, t^*), \tag{1.1}$$

and is decomposed as the sum of the imposed ambient buoyancy field and a fluctuating component $b^{*\prime}$ associated with fluid motions. In the convective setting the buoyancy perturbations are related to temperature perturbations through a thermal expansion coefficient, (see §2.2.1). Pressure is decomposed in a fashion similar to buoyancy where in the absence of fluid motions, i.e. $b^{*\prime} = 0$, the layer satisfies hydrostatic balance

$$\partial_{z^*}\delta\hat{p}^*(z^*) = -g(\rho_0^* + \delta\hat{\rho}^*(z^*)). \tag{1.2}$$

The *dimensional* Boussinesq equations governing fluid motions for a fluid with constant kinematic viscosity ν and buoyancy diffusivity κ are given by

$$D_t^* \boldsymbol{u}^* + 2\Omega \hat{\boldsymbol{z}} \times \boldsymbol{u}^* \quad = \quad -\nabla p^{*\prime} + b^{*\prime}\hat{\boldsymbol{z}} + \nu\nabla^{*2}\boldsymbol{u}^*, \tag{1.3a}$$

$$D_t^* b^{*\prime} + N^2[z^*]w^* \quad = \quad \kappa\nabla^{*2}b^{*\prime}, \tag{1.3b}$$

$$\nabla^* \cdot \boldsymbol{u}^* \quad = \quad 0, \tag{1.3c}$$

where $D_t^* \equiv \partial_t^* + \boldsymbol{u}^* \cdot \nabla^*$ is the total (Eulerian) derivative, and $\boldsymbol{u}^* = (u^*, v^*, w^*)$ is the space- and time-dependent velocity field. The ambient stratification is now characterized by the buoyancy (Brunt-Väisälä) frequency $N^2[z^*] = -g\partial_{z^*}(\delta\hat{\rho}^*(z^*)/\rho_0^*)$. When the layer is stably stratified then $N^2[z^*] > 0$, whereas when the layer is unstable $N^2[z^*] < 0$. In the absence of external forcing the stably stratified system lacks a natural source of instability for exciting fluid motions. In contrast, the Rayleigh-Bénard problem, once supplied with a sufficiently adverse temperature gradient to overcome stabilizing viscous effects, gives way to convective instability that supplies a natural source for exciting fluid motions. As will be discussed in §3, investigations of the stable layer problem will introduce mechanical forcing to induce fluid motions in a fashion similar to previous studies (Whitehead and Wingate, 2014; Marino et al., 2013).

1.1.2 Non-dimensionalization

Moving forward the aim is to work with a nondimensional form of the Boussinesq equations. The means by which a nondimensional form of the governing equations is acquired depends on the particular problem of interest. If we wish to study either rapidly rotating convection or stably stratified dynamics then, for example, a particular choice of length and velocity scales appropriate to one problem are not necessarily appropriate for the study of the other. The choice of scales used must be motivated by the physics relevant to the problem of interest. Non-dimensionalization of the governing equations aims to simplify the mathematical description of the fluid by scaling fluid variables by relevant reference values characteristic of the flow under investigation. Here, a generic non-dimensionalization is given and we pose generic characteristic length, velocity, fluctuation

buoyancy and pressure scales U^*, L^*, B^*, and P^* respectively. Using these scales we express the dimensional variables as

$$\boldsymbol{x}^* = L^*\boldsymbol{x}, \qquad \boldsymbol{u}^* = U^*\boldsymbol{u}, \qquad b^{*\prime} = B^*b, \qquad p^{*\prime} = P^*p, \tag{1.4}$$

and the dimensionless gradient

$$\nabla^* = \frac{1}{L^*}\nabla, \tag{1.5}$$

where $\boldsymbol{x}$, $\boldsymbol{u}$, b, and p are the nondimensional variables. The nondimensional variables are nominally of order-one we note that here the length scales are treated isotropically. Note that primes are no longer present and it is understood that hydrostatic balance has been subtracted from the equations of motion. Therefore, the pressure and buoyancy fields we are concerned with are the dynamic fluctuations about the hydrostatic state. Making these substitutions into the governing equations (1.3) we arrive at the dimensionless equations

$$D_t\boldsymbol{u} + \frac{1}{Ro}\hat{\boldsymbol{z}} \times \boldsymbol{u} \;=\; -Eu\nabla p + \Gamma b\hat{\boldsymbol{z}} + \frac{1}{Re}\nabla^2\boldsymbol{u}, \tag{1.6a}$$

$$D_t b + \frac{S(z)}{\Gamma Fr^2}w \;=\; \frac{1}{Pe}\nabla^2 b, \tag{1.6b}$$

$$\nabla \cdot \boldsymbol{u} \;=\; 0. \tag{1.6c}$$

where the buoyancy frequency is now expressed as $N^{*2} = N_0^{*2}S(z)$ where $N_0^{*2} = g\rho_0^{*-1}\max|\partial_{z^*}\delta\hat{\rho}^*(z^*)|$ is the maximal buoyancy frequency and $S(z) = -\partial_z\delta\hat{\rho}(z)$ is the vertical and nondimensional stratification profile. Additionally, characteristic time scales are assumed to scale advectively, hence $T^* = L^*/U^*$. Here, the characteristic scales are collected into useful nondimensional parameters which are the Rossby number Ro, Euler number Eu, buoyancy number Γ, Froude number Fr, Péclet number Pe, and Reynolds number Re, defined as

$$Ro = \frac{U^*}{2\Omega L^*}, \quad Eu = \frac{P^*}{\rho_0^* U^{*2}}, \quad \Gamma = \frac{B^* L^*}{U^{*2}}, \quad Fr = \frac{U^*}{N_0^* L^*}, \quad Pe = \frac{U^* L^*}{\kappa}, \quad Re = \frac{U^* L^*}{\nu}. \tag{1.7}$$

The Rossby number is the ratio of the planetary rotation period, $T_\Omega^* = 1/2\Omega$, to the advective time scale, $T_U^* = L^*/U^*$. The Euler number measures the significance of the pressure gradient force relative to inertial accelerations. The buoyancy number is the ratio of accelerations due to buoyancy

to inertial accelerations. The Froude number is the ratio of the buoyancy period, $T_N^* = 1/N_0^*$, to T_U^* and measures the ratio of the smallest linear wave period to the nonlinear advective time scale. The Reynolds and Péclet numbers measure the importance of viscous and buoyancy dissipation, respectively.

We note that the non-dimensional set $(Ro, Eu, \Gamma, Fr, Re, Pe)$ is not minimal and may be reduced by rescaling the pressure and buoyancy fields by letting $p \to p/Eu$ and $b \to b/\Gamma$, resulting in the set (Ro, Fr, Re, Pe). However, all parameters are retained for a careful consideration of possible equation balances.

The content presented in §2 consist of two studies concerning rapidly rotating Rayleigh-Bénard convection. The first of these works takes a statistical approach to identifying regimes of flow morphology and the coherent structures that define them. This work was a collaborative effort with Antonio Rubio and Keith Julien. A subsequent study summarized in §2.5 addresses the effects of thermal boundary conditions on rapidly rotating Rayleigh-Bénard convection. As is discussed, two boundary conditions are considered (they are the fixed flux and fixed temperature conditions), and it is shown that the governing equations become identical upon a mapping thermal variables. Therefore the statistical identification of flow regimes and their coherent structures identified in the former study using fixed temperature thermal boundary conditions remains valid for fixed flux boundary conditions. This work was a collaborative effort with Mike Calkins, Kevin Hale, Keith Julien, Derek Driggs, and Philippe Marti.

The study presented in §3 considers rapidly rotating flow under an ambient stable stratification profile. At a glimpse this problem may seem altogether distinct from that presented in §2. However, such problems are in fact related. For example, and as mentioned above, regions of the Earth's oceans undergo temporary periods of convective dynamics during cool winter months due to cool surface temperatures. With changing surface temperatures due to changing seasons the ambient density profile of ocean layer undergoes a restratification and resembles the problem of interest in §3. This study is the first to use the reduced equations in numerical simulations of a stable fluid layer. In this preliminary investigation two regimes are identified: one display-

ing columnar fluid structures with distinct and sustained layering and the second displaying only columnar fluid structures. A main focus for investigations of rotating stratified flows is the manner in which energy transferred, in particular, the manner in which energy may flow upscale and/or downscale. These are commonly referred to as inverse and forward/direct cascades and much effort has been placed on understanding the physical mechanisms responsible for such behavior in a fully three-dimensional Boussinesq fluid. A particular distinction for flows studied in this chapter is the presence of slow waves, or equivalently, the absence of a clear time scale separation between wave dynamics and order-one eddy dynamics. For this reason current and future work with the reduced equations is focused on the decomposition of periodic solutions into wave modes and vortical eddy modes. This work is an ongoing collaborative effort with Ian Grooms, Keith Julien, and Jeffrey Weiss.

Chapter 2

Statistical Classification of Flow Morphology in Rotating Rayleigh-Bénard Convection

2.1   Introduction

The main focus for the study of rapidly rotating Rayleigh-Bénard convection is the identification of coherent structures found in numerical solutions of the NH-QG equations by means which experimentalists may find useful. Specifically, in rapidly rotating convection four distinct flow regimes with uniquely identifying characteristics have been found using the NH-QG equations by varying the reduced Rayleigh number $RaE^{4/3}$ and Prandtl number σ (the origin of these non-dimensional parameters will be discussed below) and outlined by Julien et al. (2012a). In each regime the flow organizes, with varying intensity, into coherent vertical structures. The identified structures, in order of increasing $RaE^{4/3}$, consist of the cellular regime, the convective Taylor column (CTC) regime, the plume regime, and a regime characterized by geostrophic turbulence. Physical limitations in the laboratory make exhaustive experimentation of rapidly rotating convection difficult while spatio-temporal resolution challenges direct numerical simulations of the incompressible Navier-Stokes equations. These difficulties inhibit a thorough analysis of the flow morphology in the rapid rotating limit. In this chapter the flow morphologies obtained from simulations of the reduced equations are investigated from a statistical perspective. Auto- and cross-correlations of temporal and spatial signals are utilized to synthesize experimental data obtained from thermistor measurements or particle image velocimetry (PIV). Such statistics can be employed in laboratory experiments to identify transitions in flow morphology, capture the radial profiles of coherent struc-

tures, and extract transport properties of these structures. These results provide a foundation for comparison and a measure for understanding the extent to which rotationally constrained regime has been accessed by laboratory experiments and direct numerical simulations.

Rotating Rayleigh-Bénard convection is a canonical framework used to study many fluid phenomena characterized by rotation and thermal forcing. Physical systems whose dynamics are strongly influenced by these forces include the interiors of giant planets and rapidly rotating stars, the Earth's outer liquid core, and open ocean deep convection (Hubbard et al., 2002; Proctor, 1994; Marshall and Schott, 1999). In many situations the dominant influence of rotation results in geostrophy and the Proudman-Taylor constraint (Proudman, 1916; Taylor, 1923), restricting fluid motions to be invariant in the direction of the rotation axis (see §3.2.1). Due in large part to the Proudman-Taylor effect, coherent columnar structures are common to these flows and have been observed and studied experimentally (Boubnov and Golitsyn, 1986; Vorobieff and Ecke, 2002; King and Aurnou, 2012) and simulated numerically (Sprague et al., 2006; Julien et al., 2012a).

The classical Rayleigh-Bénard convection problem describes thermal convection in a fluid layer confined between two rigid, infinitely conductive, horizontal plates separated by a vertical distance H^*. The two boundaries maintain a fixed destabilizing temperature difference $\Delta T > 0$ where the lower boundary temperature is higher than that of the upper boundary. In rotating Rayleigh-Bénard convection the fluid layer rotates at a fixed rate about an axis parallel to gravity. The lower and upper nondimensional boundary temperatures are taken to be $T = 1$ and $T = 0$, respectively, resulting in the pure conduction state, $T = 1 - z$, when the destabilizing temperature drop is unable to overcome viscous effects in the fluid layer. The nondimensional parameters defining the state of the system are the Rayleigh number Ra, the Ekman number E, and the Prandtl number σ:

$$Ra = \frac{g\alpha\Delta T H^{*3}}{\nu\kappa}, \qquad E = \frac{\nu}{2\Omega H^{*2}}, \qquad \sigma = \frac{\nu}{\kappa}. \tag{2.1}$$

Ra measures the intensity of thermal forcing, E measures the importance of the rotation rate relative to viscous effects, and σ is the ratio of the thermal time scale L^{*2}/κ to the viscous time

scale L^{*2}/ν (why these time scales are relevant is explained in §2.2.1). Here g is gravity, α is the thermal expansion coefficient, ΔT is the temperature drop across the fluid layer, ν is kinematic viscosity, κ is thermal diffusivity, and Ω is the rotation rate of the system. An additional parameter of importance is the convective Rossby number $Ro = E\sqrt{Ra/\sigma}$ which is the ratio of the rotation period to the buoyancy free-fall time and measures the relative significance of rotation compared to buoyancy.

The flows of interest here are those that develop from the onset of stationary convection which occurs for $Ra > Ra_c(E)$ and $\sigma > \sigma^*$, where $Ra_c(E) \approx 8.6956E^{-4/3}$ is the Ekman dependent critical Rayleigh number and $\sigma^* \approx 0.6766$ is the critical value above which stationary convection is preferred (Chandrasekhar, 1961; Julien and Knobloch, 1999). A major challenge in studying rotationally constrained convection is avoiding the conflicting constraints imposed by the extreme values of the nondimensional parameters, i.e., maintaining $E, Ro \ll 1$ while $Ra \gg 1$. These parameter extremities are associated with thin Ekman boundary layers occurring on $\mathcal{O}(E^{1/2}H^*)$ vertical scales and fast inertial waves with $\mathcal{O}(E^{-1}\nu/H^{*2})$ frequencies occurring on $\mathcal{O}(E^{1/3}H^*)$ length scales. Numerically, this imposes prohibitive spatiotemporal resolution requirements on simulations. The range of Ekman and Rayleigh numbers accessible to recent numerical simulations of Navier-Stokes equations are $10^3 \lesssim Ra \lesssim 10^9$ and $10^{-7} \leq E \leq \infty$, respectively (King et al., 2012). For the largest rotation rates accessible to these numerical simulations, the range of reduced Rayleigh numbers becomes $RaE^{4/3} \lesssim 10$. In the laboratory, one typically selects sufficiently large rotation rates in meeting the requirement $E \ll 1$ while limiting the effects of centrifugal acceleration. The latter is measured by the rotational Froude number $Fr_\Omega = \Omega^2 L^*/g \ll 1$ which imposes an upper bound on Ω for a given lateral length scale L^* characterizing the laboratory system (typically a cylindrical tank). Additionally, the range of permissible Ra is constrained by the convective Rossby numbers $Ro_c = E^{1/3}\sqrt{8.6956/\sigma} \leq Ro < 1$. By definition, given that $Ro \propto \Delta T^{1/2}H^{*3/2} < 1$, a particular challenge then resides in the disparate temperature range required across the layer at $E \ll 1$, i.e., $\Delta T_{Ro=Ro_c}/\Delta T_{Ro=1} \propto Ro_c^2$. Specifically, $\Delta T_{Ro=Ro_c}$ is typically below the attainable resolution of experiments. For instance, for current experimental values of $E \sim 10^{-7}$, $\Delta T_{Ro=1} \sim$

$10°C$, and $\sigma = 7$, one finds $\Delta T_{Ro=Ro_c} \sim 10^{-5}°C$. Therefore the laminar convective state just above critical onset is prohibitively hard to acquire as evident in King and Aurnou (2012) and Ecke and Niemela (2013).

Presently, for the reasons stated above, laboratory experiments and direct numerical simulations are unable to completely explore, qualitatively or quantitatively, the flow morphology of rotationally constrained fluid motions from the onset of convection to geostrophic turbulence. Given the resurgent interest and that a full exploration of this regime still remains elusive, an investigation into its dynamics by alternative means is pertinent. Moreover, it is important to identify quantifiable statistical measures that are of utility to experimentalists and simulators alike. The aim here is to provide such measures that aid in understanding the rotationally constrained limit. Since the approach taken to solve these issues utilizes the NH-QG equations the flow which automatically satisfies the requirement that Ro, $E \ll 1$ while Ra is increased (Sprague et al., 2006). The resulting equations accent the prominent influence of *rotation*, i.e., geostrophy, and describe the consequential dynamics of convective motion. A brief overview of the flow morphology from the onset of convection, through the cellular, columnar, plume, and geostrophic turbulence regimes is now outlined from the investigations of Julien et al. (2012a) and Sprague et al. (2006). The flow morphology evolves from a steady conduction state with no fluid motion just before the onset of convection to unsteady cellular structures having strong vertical coherence. With increasing Ra, thermal boundary layers develop and the flow organizes into a more dilute population of convective Taylor columns (CTCs) (defined by the existence of oppositely signed shields surrounding convective cores). At higher Ra, CTCs eventually break-up into short-lived plumes that display intermittent vertical coherence across the fluid layer. An ultimate state of geostrophic turbulence is finally obtained where a turbulent interior separates two decoupled plume-emitting thermal boundary layers.

The vertical coherence of the flow structure from the cellular regime to geostrophic turbulence has been a topic of interest among theorists and experimentalists alike. For instance, determining how the heat transport (as measured by the non-dimensional Nusselt Number Nu) and its scaling

laws depend upon the flow regime. Moreover, the degradation of heat transport efficiency has been seen to coincide with diminishing vertical coherence (Julien et al., 2012b), making the study of coherent structures pertinent to understanding such global processes. Therefore, this study tracks regime transitions of the flow from the perspective of vertical coherence across the fluid layer. This is quantified by collecting horizontal slices of scalar field variables (e.g., temperature, although vertical velocity or vertical vorticity can be used) at different vertical locations in time and computing spatial and temporal cross-correlations between these slices. By pursuing this statistical avenue of analysis the following are recovered: (i) temporal scales, horizontal length scales, and velocity scales of the coherent vertical structures, (ii) the radial structure and (iii) transport properties of the flow. The novelty of this numerical study is that this statistical analysis can be readily performed experimentally. For instance, data acquired through thermistor measurements (King and Aurnou, 2012) or PIV measurements on a laser sheet(Bordes et al., 2012) give the necessary data needed for an experimental duplication of this numerical study. Given the aforementioned experimental challenges, the approach taken here using the NH-QG equations can provide a more precise means of discerning flow regimes in the rotationally constrained limit.

In the following, connection to the NH-QG equations for the purposes of studying rapidly rotating Rayleigh-Bénard convection is given by introducing physically relevant characteristic scales yielding the appropriate equations for use in numerical simulations of rotating convection. An explanation of the statistical techniques used to study the flow morphology is then provided. In §2.3, a presentation of the results of the statistical analysis is given. In §2.4.1, a comparisons between azimuthally averaged radial profiles (similar to those studied by Grooms et al. (2010)) and ensemble averaged spatial auto-correlations are considered. Since strong agreement is found between radial profiles and spatial auto-correlations, spatial auto-correlation functions are used in computing net circulation and mass flux in §2.4.2. Using temporal and spatial auto-correlations characteristic scales describing the flow in §2.4.3 are presented. Finally, in §2.4.4, estimates describing how experimental ensemble averaged correlation functions with increasing samples converge to the numerical ensemble-averaged correlation functions are discussed.

2.2 Governing equations and methodology

2.2.1 Governing equations and characteristic scales

Before giving the reduced equations used for studying rotating convection it is important to make a physically sensible choice for the characteristic scales used. The onset of convection occurs when the destabilizing temperature drop across the layer is severe enough to overcome viscous effects that initially act to inhibit fluid motions. For this reason, the dissipation term in the vorticity equation

$$D_t \boldsymbol{\omega} = \left(\boldsymbol{\omega} + \frac{1}{Ro} \hat{\boldsymbol{z}} \right) \cdot \nabla \boldsymbol{u} + \nabla \times b \hat{\boldsymbol{z}} + \frac{1}{Re} \nabla^2 \boldsymbol{\omega}. \tag{2.2}$$

must be involved in the dominant balance with vortex stretching by planetary rotation. When $Ro \ll 1$, Taylor-Proudman constraints restrict vertical variations on small scales, therefore vertical modulations due to convective motions must occur on large scales, i.e., $H^* \gg L^*$ in such a way that brings a leading-order balance between dissipation and vortex stretching due to planetary rotation in equation (3.15). Requiring such a balance demands that

$$\frac{L^*}{RoH^*} = \frac{1}{Re} \implies L^* = E^{1/3} H^*, \tag{2.3}$$

informing us of how horizontal scales L^* relate to the large vertical scale H^*. How this leads to a sensible choice for the velocity scale U^* may be understood as follows. With the above relation (2.3) for H^* and L^* and the understanding that viscous effects are important, the balance in the vorticity equation (3.15) between the dissipation and stretching by system rotation implies

$$\frac{E^{1/3}}{Ro} = \frac{1}{Re} \implies U^* \equiv \frac{\nu}{L^*} = \frac{(fL^*)L^*}{H^*}. \tag{2.4}$$

The last relation here relates the viscous velocity scale ν/L^* to the rescaled rotational velocity fL^*. The obvious choice for a velocity scale is $U^* \equiv \nu/L^*$ since f makes no appearance in the NH-QG equations (valid in for $Ro \ll 1$). Moreover, this gives us the relation $L^* = RoH^*$ by substituting fL^{*2}/H^* into the expression for Ro, therefore in this context of rapidly rotating Rayleigh-Bénard convection $Ro = E^{1/3}$. We may now deduce the relationship between the Froude number as defined

in equation (1.7) with the Rayleigh number defined in (2.1). Specifically, if we take $U^* = \nu/L^*$, $L^* = E^{1/3}H^*$, and relate the scale for density fluctuations to temperature fluctuations by the use of the thermal expansion coefficient α (dimensionless relative change in density per unit change in temperature) by

$$\frac{\alpha \Delta T}{H^*} = \frac{\max|\partial_{z^*}\delta\hat{\rho}^*(z^*)|}{\rho_0^*}, \tag{2.5}$$

then from the definition of Fr in (1.7) it follows that

$$Fr^{-2} = \frac{N_0^{*2}L^{*4}}{\nu^2} = \frac{g\max|\partial_{z^*}\delta\hat{\rho}^*(z^*)|L^{*4}}{\rho_0^*\nu^2} = \frac{RaE^{4/3}}{\sigma}, \tag{2.6}$$

valid when the nondimensional stratification profile $S(Z) = -\partial_Z\hat{\rho}(Z) < 0$, necessary for the layer to be in an unstable configuration and for the validity of relation (2.3). Upon rescaling buoyancy variables $((b,\bar{b}) \to RaE^{4/3}(b,\bar{b})/\sigma)$ such that the mean buoyancy profile in a pure conduction state is linear we arrive at the reduced equations given below.

In the limits $E \ll 1$ and $Ro \ll 1$, the NH-QG equation set that results from the rigorous multiple scales asymptotic reduction of the incompressible Navier-Stokes equations (given in appendix B) for a convecting plane-layer fluid (Julien et al., 1998; Sprague et al., 2006) take the form

$$\partial_t\zeta + J[\psi,\zeta] - \partial_Z w = \nabla_\perp^2\zeta, \tag{2.7a}$$

$$\partial_t w + J[\psi,w] + \partial_Z\psi = \frac{RaE^{4/3}}{\sigma}\theta + \nabla_\perp^2 w, \tag{2.7b}$$

$$\partial_t\theta + J[\psi,\theta] + w\partial_Z\overline{T} = \frac{1}{\sigma}\nabla_\perp^2\theta, \tag{2.7c}$$

$$\partial_\tau\overline{T} + \partial_Z(\overline{w\theta}) = \frac{1}{\sigma}\partial_Z^2\overline{T}. \tag{2.7d}$$

With viscous scalings used for non-dimensionalization with L^{*2}/ν and ν/L^* giving the time and velocity scales, respectively, these reduced equations capture balanced geostrophic convective motions and slow inertial waves while filtering the computationally prohibitive fast inertial waves (Julien et al., 2012a) and the thin Ekman layers at the upper and lower boundaries (Niiler and Bisshopp, 1965; Julien et al., 2012a). Motion is driven by a destabilizing temperature drop as measured by the reduced Rayleigh number $\widetilde{Ra} = E^{4/3}Ra$. Just as before, ψ is the first-order pressure, or equivalently,

the geostrophic streamfunction. The streamfunction ψ is related to the vertical vorticity through the relation $\zeta = \nabla_\perp^2 \psi$. The Jacobian remains as before $J[\psi, f] = \partial_x \psi \partial_y f - \partial_y \psi \partial_x f = \boldsymbol{u}_\perp \cdot \nabla_\perp f$, giving the horizontal advection of the fluid variable f. The temperature field is decomposed into mean and fluctuating components, $T(x, y, Z, t, \tau) = \overline{T}(Z, \tau) + Ro\, \theta(x, y, Z, t, \tau)$, where $\varepsilon \equiv Ro = E^{1/3}$ is the small asymptotic expansion parameter used in the derivation given in appendix B. Impenetrable fixed-temperature boundary conditions are used, specifically

$$w \;=\; 0, \quad T = 1, \quad \Rightarrow \partial_Z \psi = 0, \quad \theta = 0, \quad \text{at} \quad Z = 0, \tag{2.8}$$

$$w \;=\; 0, \quad T = 0, \quad \Rightarrow \partial_Z \psi = 0, \quad \theta = 0, \quad \text{at} \quad Z = 1. \tag{2.9}$$

Note that a stress-free surface is such that $\partial_Z \zeta = 0$, however, in this framework $\partial_Z \zeta = \nabla_\perp^2 \partial_Z \psi = 0$. Therefore the above boundary conditions imply stress-free horizontal velocity at the top and bottom boundaries. The aforementioned passive Ekman layers corresponding to no-slip boundary conditions can be recovered at a higher asymptotic order.

It is reassuring to note that the above length, velocity, and time scales ($L^* = E^{1/3} H^*$, $\nu E^{-1/3}/H$, and $E^{2/3} H^2/\nu$, respectively) of the asymptotic model are identical to those observed in linear theory and laboratory experiments for both plane-parallel (Chandrasekhar, 1961; Kunnen, 2008; Sakai, 1997) and spherical geometries (Jones et al., 2000; Olson, 2011; Garcia et al., 2008). However, the later has additional complexities due to spherical boundaries. Furthermore, despite many numerical and experimental investigations on the topic of rotating Rayleigh-Bénard convection there remains a insufficiency of quantitative data in the rotationally constrained regime detailing nonlinear flow morphology and any associated scaling laws.

2.2.2 Numerical solver

The reduced equations are simulated in a horizontally periodic domain where all fields are represented by a Fourier expansion in the horizontal directions and a Chebyshev expansion in the vertical. The use of Chebyshev discretization in the vertical is in contrast to the use of Fourier expansions in all three coordinate directions for the simulation of triply-periodic rotating and

stably stratified flows (for details on this, see in §3). The physical reason for this difference is due to the presence of thin thermal boundary layers that form in regions immediately adjacent to top and bottom boudaries in the convection setting. Near these boundaries the flow must quickly change and adjust to satisfy the stress-free conditions (2.9). The spectral expansions are dealiased according to the standard 2/3's rule and time discretization is handled via a mixed implicit/explicit third-order Runge-Kutta scheme (Spalart et al., 1991b). Buoyancy, diffusion, and rotation terms are treated implicitly while the advection terms and $w\partial_Z\overline{T}$ are treated explicitly. For numerical simulations performed for this investigation of thermal convection the size of the domain is set to $20L_cE^{1/3}H^* \times 20L_cE^{1/3}H^* \times H^*$ where $L_c = 2\pi/k_c \approx 4.8154$ is the nondimensional critical length scale for the onset of convection in the E, $Ro \ll 1$ limit (Chandrasekhar, 1961). The numerical resolution used is Ra-dependent and is identical to the resolutions used in previous studies utilizing the NH-QG equations (Julien et al., 2012a); the maximum resolution used at $RaE^{4/3} = 140$ and $\sigma = 1$ is $N_x \times N_y \times N_z = 512 \times 512 \times 385$. Finally, acknowledging that a horizontal domain containing a large number of fluctuations suffices for time and horizontal averaging to become statistically equivalent, we set $\partial_\tau\overline{T} \equiv 0$ and replace averaging over x, y and t by spatial averaging over x and y only, as earlier studies have shown their equivalence in a sufficiently large domain as $t \to \infty$ (Julien et al., 1998).

2.2.3 Computation of auto- and cross-correlations

To identify coherent structures and discern morphological transitions in rotating convective flow the aim here is to quantify the vertical coherence in the fluid. This is achieved by computing cross-correlations between a pair of signals obtained at two different vertical locations: temporal signals are extracted at the same horizontal spatial locations whilst spatial signals are extracted at a fixed time and fixed y (or fixed x). The temporal cross-correlation between two signals of finite-length T is defined (Proakis and Manolakis, 2007) as

$$(f \star g)(l) = \frac{\int_0^T \overline{f(t)}g(t+l)dt}{\sqrt{\int_0^T |f(t)|^2dt \int_0^T |g(t)|^2dt}}, \tag{2.10}$$

where l is the lag or temporal shift between the signals and the overbar denotes complex-conjugation. The Fourier convolution theorem is utilized to compute the cross-correlation

$$(f \star g)(l) = \frac{\mathcal{F}^{-1}\left(\overline{\mathcal{F}(f)}\mathcal{F}(g)\right)(l)}{\sqrt{\sum |\mathcal{F}(f)|^2 \sum |\mathcal{F}(g)|^2}}, \tag{2.11}$$

where $\mathcal{F}$ denotes the Fourier transform. The cross-correlations computed are normalized such that auto-correlations satisfy $(f \star f)(0) = 1$ and are bounded in the usual way, i.e., $-1 \le (f \star g)(l) \le 1$. This normalization treats small and large amplitude signals similarly and extracts the collinearity of the signals for varies values of the lag variable l. By definition the auto-correlation of a real-valued finite-duration function is even and thus only positive lag values need be considered. An identical definition for the spatial cross-correlation is used where t is replaced by a variable in a spatial direction.

Flows studied here are statistically isotropic in horizontal directions and statistically stationary in time. Temporal auto- and cross-correlations are computed for signals sampled at $N_x \times N_y$ independent horizontal numerical grid points from which an ensemble average (or mean) is calculated. The result of ensemble averaging is a one-dimensional function of the lag variable l with reduced noise to signal errors. Similarly, spatial auto- and cross-correlations are computed for signals sampled at N_y (or N_x) independent locations for roughly 5% to 10% of the N_t time-steps performed (i.e. $N_y \times N_t \times 0.05$ or $N_x \times N_t \times 0.05$ samples) from which an ensemble average is calculated.

Since finite duration signals are used, cross-correlations in equation (2.10) are biased due to diminishing signal overlap $(0 < t < T - l)$ with increasing lag l. This diminishing overlap implies that the integral in equation (2.10) becomes dominated by the trivial product $f(t)g(t+l) = 0$ for values of $t \notin [0, T - l]$ and for large values of l, thus biasing the integral towards 0. Corrected (unbiased) cross-correlations take the form $\frac{N}{N-|l|}(f \star g)(l)$, where N is the length of the signal. The relative error between the biased and unbiased signal is $|l|/N$. We find that the information pertaining to vertical coherence are contained in lag values $l \ll N$, such that unbiased corrections are negligible. For spatial half-width cross-correlation values discussed below the average relative

error ratio is $|l|/N \in [0.0063, 0.0072]$. For temporal half-width cross-correlation values the average relative error ratio is $|l|/N \in [0.0020, 0.0486]$, the largest of these ratios occurs at the lowest reduced Rayleigh number $RaE^{4/3} = 9$.

2.3 Results

In the following, we describe the spatial and temporal structure of the four flow regimes found in rapidly rotating Rayleigh-Bénard convection via the correlation measures outlined above. The flow regimes have been identified in $(RaE^{4/3}, \sigma)$ parameter space and laid out in a previous investigation (Julien et al., 2012a). Here we restrict our investigations to $Ra_c E^{4/3} < RaE^{4/3} \leq 80$ for fixed Prandtl number, $\sigma = 7$, (an experimentally relevant value similar to that of water (King and Aurnou, 2012)) focusing on flow transitions from near stationary convective onset through convective Taylor columns and plumes. The case for geostrophic turbulence at $\sigma = 7$ is numerically expensive, so this case is considered separately for $\sigma = 1$ and $RaE^{4/3} = 140$. Two sets of vertically separated locations are used in constructing the cross-correlation functions of thermal perturbations, i.e., of simulated thermistor data that emulates experimental thermal readings. The first is a set of interior points at fixed (x, y) and with vertical coordinates $Z = 0.2, 0.4, 0.6, 0.8$ (labeled with subscripts $0.2, 0.4, 0.6, 0.8$). This setup is easily implemented in a laboratory and results are robust provided that thermistor locations are uniformly distributed over the layer depth. The second set of Z-locations used are associated with the thermal boundary layers. Specifically, these locations are where conduction and convection contribute equally to heat transport (these are labeled with subscripts + and -, respectively) (Julien et al., 2012a). The thermal boundary layer (TBL) locations, found at $\max(\overline{|\nabla_\perp \theta|^2})$ and well approximated by $\max(\overline{\theta^2})$, vary with $RaE^{4/3}$ and σ and are difficult to attain *a priori* in a laboratory setting. However, TBL locations are only considered here to investigate the extent of vertical coherence across the fluid layer (King and Aurnou, 2012). We find that results obtained at interior and TBL locations yield similar measures of vertical coherence and, hence, similar measures for the classification of flow morphology in rapidly rotating Rayleigh-Bénard convection.

The configuration of thermistor locations described here and the calculation of ensemble averaged correlations described in section 2.2.3 amount to very modest memory requirements of roughly 400 GB. However, this amount of memory consists of superfluous data not needed to provide the essential results.

2.3.1 Spatial structure of thermal fluctuations

Figure 2.1 shows 3D volume renders of thermal fluctuations θ at fixed times for parameters in the four different flow regimes along with planar slices for each case at $Z = 0.2$ and $Z = 0.8$. The cellular solution at $RaE^{4/3} = 10$, $\sigma = 7$ shown in figure 2.1(a) closely resembles single-mode (or single-wavenumber) solutions (Julien and Knobloch, 1999; Sprague et al., 2006) in that they share the same vertical structure for (θ, w, ζ) along with a vertical coherence that spans the layer depth. The associated auto- and cross-correlations are shown in figure 2.2. Near onset, linear stability sets the length scales of the flow and accordingly the first maximum in the correlation signals occur at the critical length scale ($d_x/L_c \approx 1$), indicating the ability of ensemble averaged spatial cross-correlations to capture horizontal structure of the flow. In fact, and as we shall see in §2.4.1, these spatial correlation functions have the ability to recover radial structure. The vertical coherence can be seen directly by inspecting the two planes of data at $Z = 0.2$ and $Z = 0.8$ in figure 2.1(a) and is reflected in the spatial cross-correlation $(\theta_{0.8} \star \theta_{0.2})(d_x/L_c)$ in figure 2.2(b) giving the spatial auto- and cross-correlation across the fluid layer, comparing fluid at height $Z = 0.2$ to fluid at height $Z = 0.8$. The correlation coefficients for these cross-correlations at zero horizontal displacement $d_x/L_c = 0$ is 0.9874. The trend of strong vertical coherence continues for larger horizontal displacements in both the auto-correlation (figure 2.2(a)) and the cross-correlation (figure 2.2(b)). Notably, the correlations have slowly decaying oscillatory tails indicative of a spatially modulated cellular pattern. Very similar correlations are found in the vertical vorticity and the vertical velocity fields. Additionally, the auto-correlation functions in figure 2.2(a) give a measure of the characteristic width of the central core of these vertically coherent structures, is illustrated in figure 2.4 and will be discussed further below.
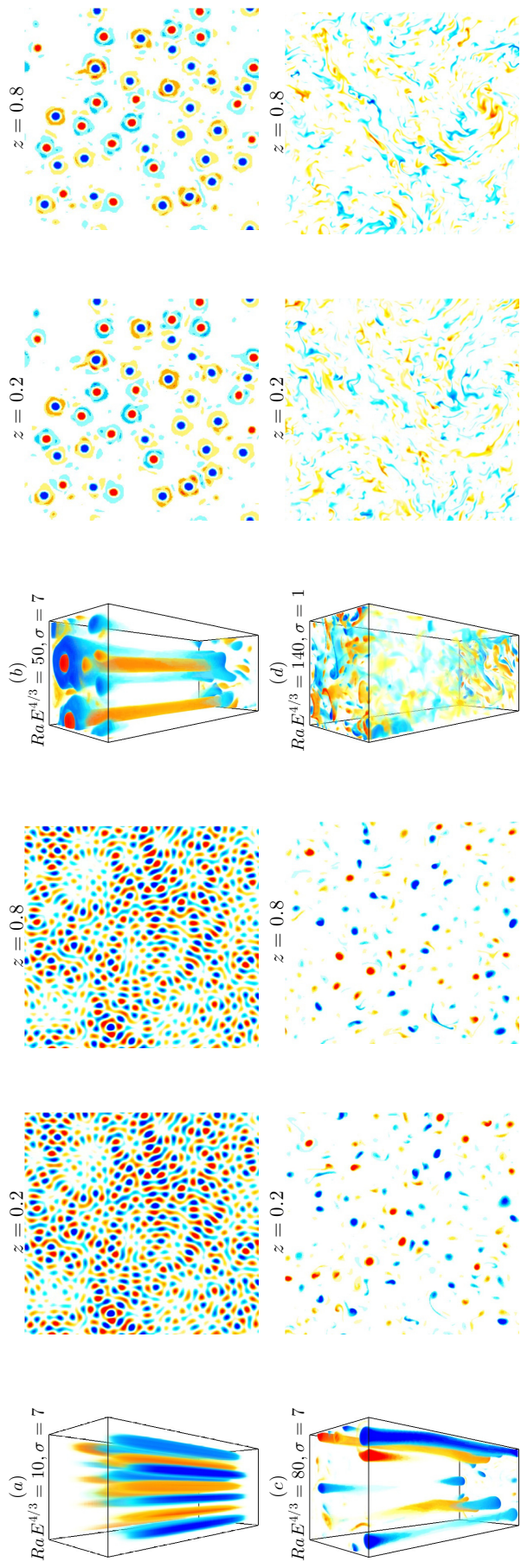
Figure 2.1: Volume renders of θ in a $4L_c \times 4L_c \times 1$ subregion and planar renders of θ in a $20L_c \times 20L_c$ ($L_c = 4.8154E^{1/3}$) region at $Z = 0.2$ and $Z = 0.8$. The first three renders are shown for $\sigma = 7$, (a) $RaE^{4/3} = 10$ (cellular), (b) $RaE^{4/3} = 50$ (columnar), and (c) $RaE^{4/3} = 80$ (plume) solutions along with (d) $\sigma = 1$, $RaE^{4/3} = 140$ (geostrophic turbulence). Warm (cold) fluid is visualized as red (blue).
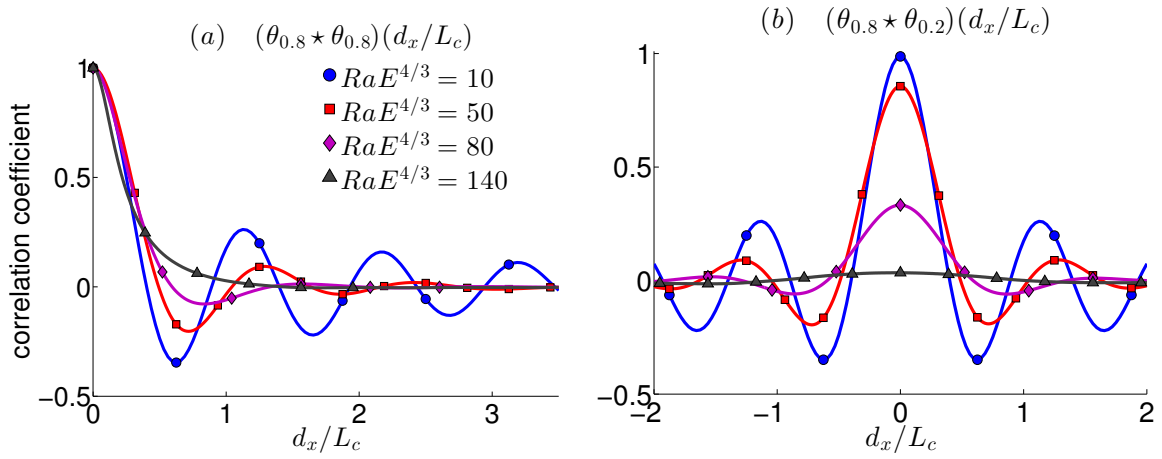
Figure 2.2: Ensemble averaged spatial auto-correlations (a) at $z = 0.8$ and cross-correlations (b) between signals at $Z = 0.2$ and $Z = 0.8$ for θ and for the parameters shown in figure 2.1. By definition auto-correlations are even functions and thus only positive displacement are shown for (a). Similar correlation functions are found for vertical velocity and vorticity fields.

The regime of shielded convective Taylor columns (CTC's) is illustrated in the volume rendering figure 2.1(b) for $RaE^{4/3} = 50$, $\sigma = 7$. In addition to CTCs the rendering also illustrates the presence of some weaker thermal plumes near the top and bottom boundaries. Again, the ensemble averaged spatial auto-correlation (figure 2.2(a)) captures the radial structure of the flow, i.e., the strong thermal cores and oppositely signed shield seen in figure 2.1(b) are associated with a central peak at zero displacement and a minimum occurring within the displacement interval $d_x/L_c \in [0, 1]$, respectively, in figure 2.2(a). The spatial correlations also identify an additional shield (i.e., a local maximum) occurring within the displacement interval $d_x/L_c \in [1, 1.5]$. This indicates the presence of an additional secondary shield whose signal is of the same magnitude as the ambient fluctuations outside the region of coherence identified as CTCs, as such, these secondary shields are less coherent and not discernible in the volume rendering but captured in the ensemble averaged correlations. The two thermal planes in figure 2.1(b) show a strong vertical (top-to-bottom) *visual* similarity for the CTC cores and a weaker similarity for the shields. Correspondingly, the cross-correlation in figure 2.2(b) shows a strong correlation (≈ 0.86) at zero displacement and a weaker anti-correlation (≈ -0.2) for the minimum within the displacement interval $d_x/L_c \in [0, 1]$. The overall similarity between the auto- and cross-correlation shows evidence of rigid vertically coherent structures.

The plume state, illustrated for $RaE^{4/3} = 80$ and $\sigma = 7$ in figure 2.1(c), has thermal structure that stretches throughout the layer but lacks the rigid vertical structure of the cellular and CTC solutions. The characteristic width of the central core remains almost unchanged as is evident from auto-correlations in figure 2.2(a) while the oppositely signed shielding (i.e., the minimum correlation value) is much less pronounced and the secondary shielding (i.e., the local maximum correlation value) of the CTC's has now disappeared. This is a reflection that the shields that were quite strong for the CTC case are now much weaker. A look at the cross-correlation in figure 2.2(b) shows a decreased vertical coherence at all displacements with increased $E^{4/3}Ra$.

Finally, the volume render of the geostrophic turbulence state at $RaE^{4/3} = 140$ and $\sigma = 1$ shows no top-to-bottom organization on the L_c scale, however, the planes in figure 2.1(d) of θ at $z = 0.2$ and 0.8 show evidence of smaller scale plumes and of a large-scale circulation (Julien et al.,

2012a; Rubio et al., 2014) (LSC) in the form of a dipole vortex that is a characteristic of geostrophic turbulence. The corresponding spatial auto-correlation in figure 2.2(a) shows a sharper drop off at displacements from $d_x/L_c = 0$ to 0.4 but a continuing positive correlation throughout (i.e., no extrema other than the maximum at zero displacement).

We find that results for spatial-correlations of the vertical vorticity and velocity are qualitatively similar in all four regimes to those of the thermal perturbation with the exception of a sign change for vertical vorticity correlation functions (easily understood from equation (2.7) and from the tendency of a fluid parcel with positive temperature to spin-up while accelerating away from the bottom plate and spin-down whilst decelerating towards the upper plate).

In figure 2.3 we illustrate spatial auto- and cross-correlations as a continuous function of $RaE^{4/3}$. The transition from cells to CTC is evident at $RaE^{4/3} \approx 22$ and the transition from CTCs to the plume regime is clearly identified at $RaE^{4/3} \approx 55$. Up to this point we have only discussed results from the interior ($Z = 0.2, 0.8$) auto- and cross-correlations and have so far avoided discussing results associated with the TBL that are extremely challenging to obtain experimentally. However, both approaches yield strikingly similar results although the TBL correlations give a slightly clearer picture of the regime transitions from cells to CTCs, and from CTCs to plumes. The transition between these regimes can be seen as a sharp transition in the correlation gradient in the $RaE^{4/3}$-direction of both panels in figure 2.3 which show color scaled maps of the auto-correlation data (left panel) and cross-correlation data (right panel). Additionally, indications of half-widths for the primary peak, zeros, and extrema are also given. While a number of these measures can be used to identify regime transitions we focus on that with the highest signal to noise ratio: the maximum of the spatial cross-correlation at zero displacement (note the strong gradient in the $RaE^{4/3}$-direction at zero displacement in the color scale in the right panel).

From figure 2.3(a) and 2.3(b) we see that auto-correlations and cross-correlations in the interior share qualitatively similar features. Similar results are found for auto- and cross-correlations for data taken from TBL locations. At onset the linear stability problem sets the length scales of the flow and accordingly the first zero (denoted by the first dashed line where $(\theta_{0.8} \star \theta_{0.2})(d_x/L_c) = 0)$)
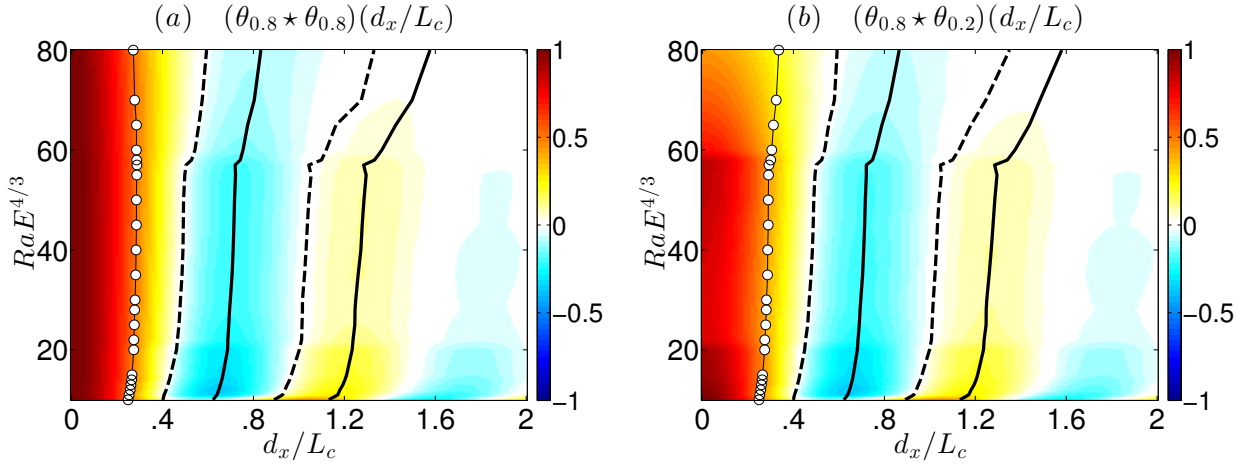
Figure 2.3: (*a*) Spatial auto- and (*b*) cross-correlations displayed over a continuous range for $RaE^{4/3} \in [10, 80]$ which illuminates the radial flow structure. Correlation function half-widths (circles), extrema (solid lines), and zeros (dashed lines) are indicated. The transition from the cellular regime to the CTC regime is evident at $RaE^{4/3} \approx 22$ while the transition from the CTC to the plume regime is clearly evident at $RaE^{4/3} \approx 55$; each transition is denoted by a horizontal line where the color gradient drops sharply in the $RaE^{4/3}$-direction.
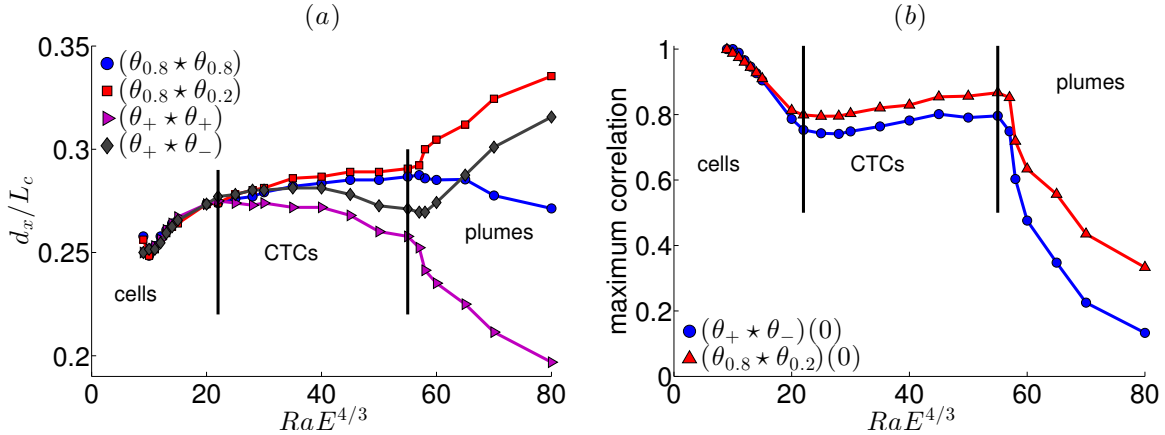
Figure 2.4: (*a*) Half-width of spatial auto- and cross-correlations for equispaced and TBL cases, (*b*) maximum spatial cross-correlation values at zero displacement as a function $RaE^{4/3}$ for equispaced and TBL cases. Transitions between the cellular and CTC regimes (at $RaE^{4/3} \approx 22$) and CTC and plume regimes (at $RaE^{4/3} \approx 55$) are identified. TBL data is denoted by $+$ and $-$ to indicate signals taken from top and bottom TBLs, respectively. Data here is taken from simulations with $\sigma = 7$.

occurs at $d_x/L_c \approx 0.4$. This length scale increases with $RaE^{4/3}$ and smoothly joins the CTC scaling at $RaE^{4/3} \approx 22$ of roughly $d_x/L_c \approx 0.5$. While it is difficult to identify the regime change using half-widths from either the spatial auto-correlation or cross-correlation, the transition is clear by comparing the two methods as shown in figure 2.4. For the cellular regime the half-widths of the correlation functions are almost identical while they diverge for the CTC regime. This divergence is quite small when measured at interior heights $Z = 0.2$ and $Z = 0.8$ but quite pronounced when measurements are made in the TBL. For both interior and TBL cases the cross-correlation half-widths (figure 2.4(a)) increase throughout the plume regime. This behavior can be understood by inspecting the volume render in figure 2.1(c) where the centroids of columnar structures are seen to meander with depth (thus, lacking the rigid vertical structure seen in the cellular and CTC regimes). As a result, top-to-bottom cross-correlation half-widths convey strong correlations at larger displacements due to structures meandering in the horizontal directions.

Another method for discerning the transitions between regimes is to consider the spatial cross-correlation functions at zero displacement shown in figure 2.4(b), where both TBL and interior cross-correlations are the focus. At $Ra_cE^{4/3}$ we see that the correlation coefficient at zero displacement for measurements in the interior or TBL is one, that is, $(\theta_+ \star \theta_-)(0) = 1$ and $(\theta_{0.8} \star \theta_{0.2})(0) = 1$, showing perfect vertical coherence. As $RaE^{4/3}$ increases the correlation coefficient at zero displacement decreases, achieving a local minima at the smooth transition from cellular solutions to CTC-dominated solutions. After this transition away from cellular structures towards CTCs a steady increase in vertical coherence is observed, indicating a strengthening of coherence of CTCs with increased thermal forcing. However, this steady increases gives way to a steep dive at the transition to plume solutions where the loss of the CTC shields leads to a steep drop in vertical coherence. The cause for the breakdown or instability of CTC structures is not known, however any analytic theory can giving a critical value of $RaE^{4/3}$ for this transition can certainly utilize figure 2.4(b) as a bases for comparison. Similar results for identifying regime transitions from temporal cross-correlations are considered below in §2.3.2.

Thus far spatial correlation functions have been computed using one-dimensional signals sam-
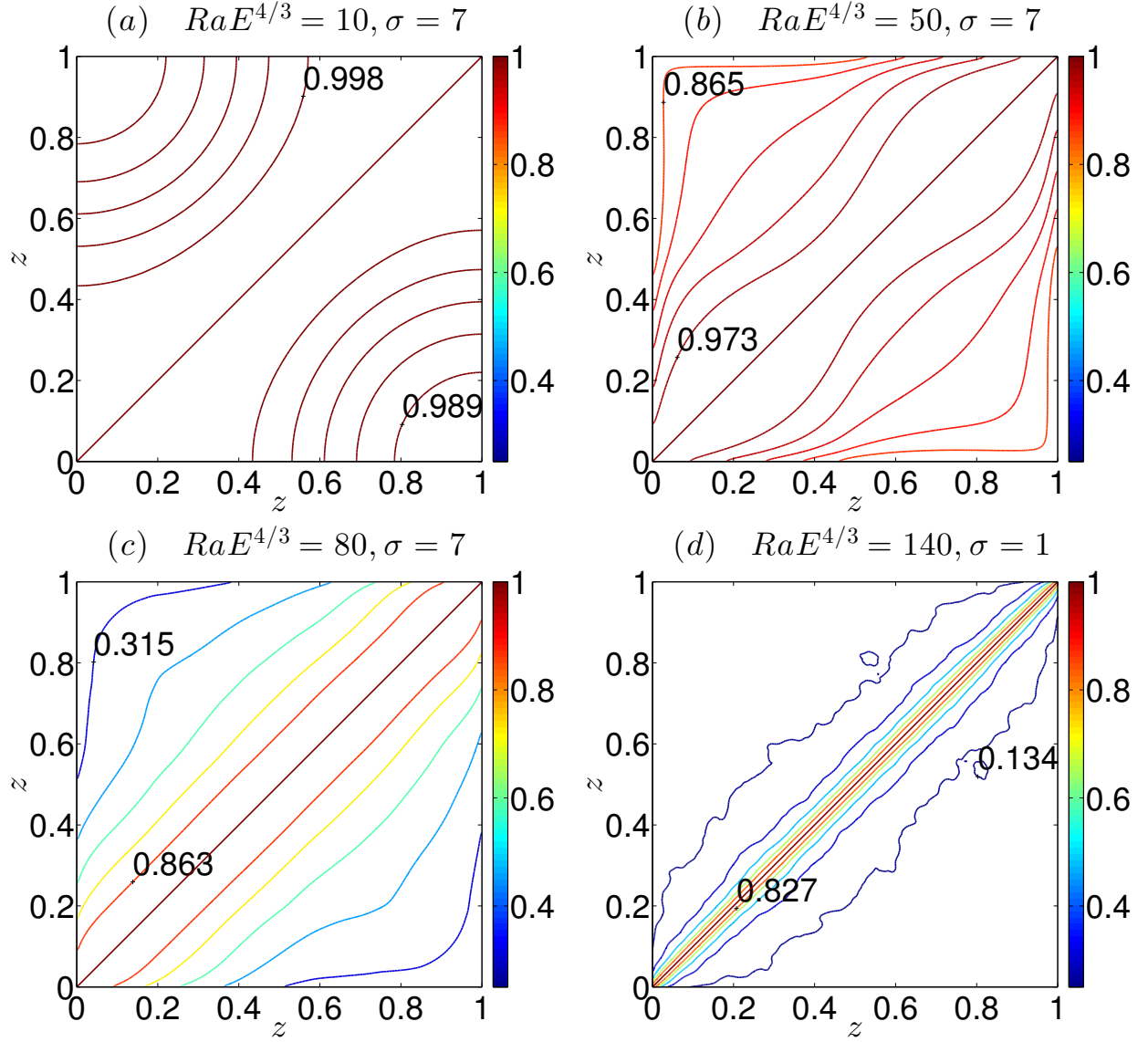
Figure 2.5: Correlation contours of the correlation surface Π corresponding to two-dimensional inner-products defined by equation (2.12) between all pairs of horizontal planes from the numerical simulation of the NH-QG equations. Diagrams $(a) - (d)$ indicate lowest and highest correlation contour values (excluding correlation values of 1 along the diagonal) and show decreasing vertical length scales corresponding to overall decreased vertical coherence with increasing $RaE^{4/3}$. Note that the indicated diagonal corresponds to $\Pi = 1$, which results from the inner-product of $p_i(\boldsymbol{x})$ with itself.

pled with a single horizontal plane at fixed Z. In the following we consider the correlation between each horizontal plane with all other horizontal planes which provides a continuous interpretation of the vertical coherence length scale. This approach takes a horizontal plane of fluid data (call this plane of data $p_i(\boldsymbol{x})$, where i denotes the vertical grid point and where $\boldsymbol{x} = (x, y)$) in physical space and finds the correlation with all other horizontal planes $p_j(\boldsymbol{x})$. Since the domain is two-dimensional we employ the following two-dimensional inner-product in determining the degree of collinearity between horizontal planar flows

$$\Pi \equiv \frac{1}{\|p_i\|\|p_j\|} \int_{\mathbb{T}^2} p_i(\boldsymbol{x})p_j(\boldsymbol{x})d\boldsymbol{x}, \tag{2.12}$$

where $i, j = 1, 2, \ldots, N_Z$, where N_Z is total the number of grid points in the vertical, and $\mathbb{T}^2$ denotes the periodic horizontal domain. As with the cross-correlation functions, we normalize by the L^2-norm of the functions under consideration. Performing these calculations yields a correlation surface comprised of N_z^2 values describing the collinearity between all horizontal planar solutions. Given the symmetry of equation (2.12) the correlation surface Π becomes symmetric about the vertical plane $i = j$ where $\Pi = 1$. The resulting symmetric contour plots of Π are given in figure 2.5 where values for the highest and lowest correlation-contour values are provided.

The vertical coherence identified in figure 2.2 for the four regimes is now apparent in figure 2.5. Given the strong spatial cross-correlations for the cellular and CTC regimes (see figure 2.4(b)) it is unsurprising that Π is near unitary between all pairs of z-locations in figure 2.5(a, b). This indicates that the structures are coherent across the entire layer. Also evident in figure 2.5(a, b) is the variability in the vertical coherence length scale measured by the distance between two contours. It is evident that the vertical coherence of a plane with any other plane depends on their vertical locations in the fluid layer. For $RaE^{4/3} = 10$ and $\sigma = 7$ the largest coherent intervals reside near the boundaries at $z = 0$ and $z = 1$, while for $RaE^{4/3} = 50$ these regions reside both away from the boundaries and away from the mid-plane at $z = 1/2$. The vertical coherence deteriorates significantly with increasing $RaE^{4/3}$ (figures 2.5(c, d)). To measure the extent of vertical coherence we use the threshold value of $\Pi = 0.5$, therefore classifying two planes separated by some distance

Table 2.1: Summary of characteristic length, time, and velocity scales for coherent structures. The lateral length scales L_{hw}, time scales T_{hw} (based on spatial and temporal half-widths of auto-correlations, respectively), and resulting advective Lagrangian structure-velocities $U_{coh} = L_{hw}/T_{hw}$ are outlined. For comparison, lateral Eulerian RMS fluid velocities U_{rms} are provided. Time and velocity scales are in terms of buoyancy times T_b. Note that, roughly, $U_{coh} \to U_{rms}$ as $RaE^{4/3}$ increases and the flow approaches the geostrophic turbulence regime.

	L_{hw}	T_{hw}	U_{coh}	U_{rms}	U_{coh}/U_{rms}
$RaE^{4/3} = 10$, $\sigma = 7$ (cells)	1.1963	72.4697	0.0165	0.2302	0.0717
$RaE^{4/3} = 50$, $\sigma = 7$ (columns)	1.3731	11.3918	0.1205	0.7475	0.1612
$RaE^{4/3} = 80$, $\sigma = 7$ (plumes)	1.3067	3.0203	0.4326	1.0150	0.4262
$RaE^{4/3} = 140$, $\sigma = 1$ (turbulence)	1.0459	0.1665	6.2802	7.1708	0.8758

to be vertically coherent if their corresponding inner-product is such that $\Pi > 0.5$. Moreover, the distance at which Π transitions from being larger than $1/2$ to less than this critical value is deemed the vertical correlation length scale. In the plume regime (figure 2.5(c)) we find vertical correlation length scales of $\approx 0.6H$ for $\Pi > 0.5$. In the geostrophic turbulence regime (figure 2.5(d)) where $RaE^{4/3} = 140$ and $\sigma = 1$ we find vertical coherence length scales of $\approx 0.06H$ for $\Pi > 0.5$. Therefore, the vertical correlation length scale suffers an order of magnitude decline when moving from the plume regime to geostrophic turbulence.

2.3.2 Temporal structure of thermal fluctuations

While the previous section detailed the spatial structure of the different flow regimes and provided clear measures for the determination of transitions in the flow, however as of this writing horizontal planes of data can be difficult to obtain in laboratory experiments. For most convection experiments the primary observables are the global heat flux through the layer and pointwise temperature measurements at a limited number of locations. Due to the experimental challenges in capturing the rotationally constrained branch of convection at $E, Ro \ll 1$ while $Ra \gg 1$, heat flux measurements remain inconclusive as a proxy measure for regime transitions (Ecke and Niemela, 2013; King and Aurnou, 2012). We therefore look to determine the temporal structure of the four regimes using auto- and cross-correlations between two vertically separated thermal time signals (thermistor signals). The temporal auto-correlation describes how long a coherent structure takes to cross a
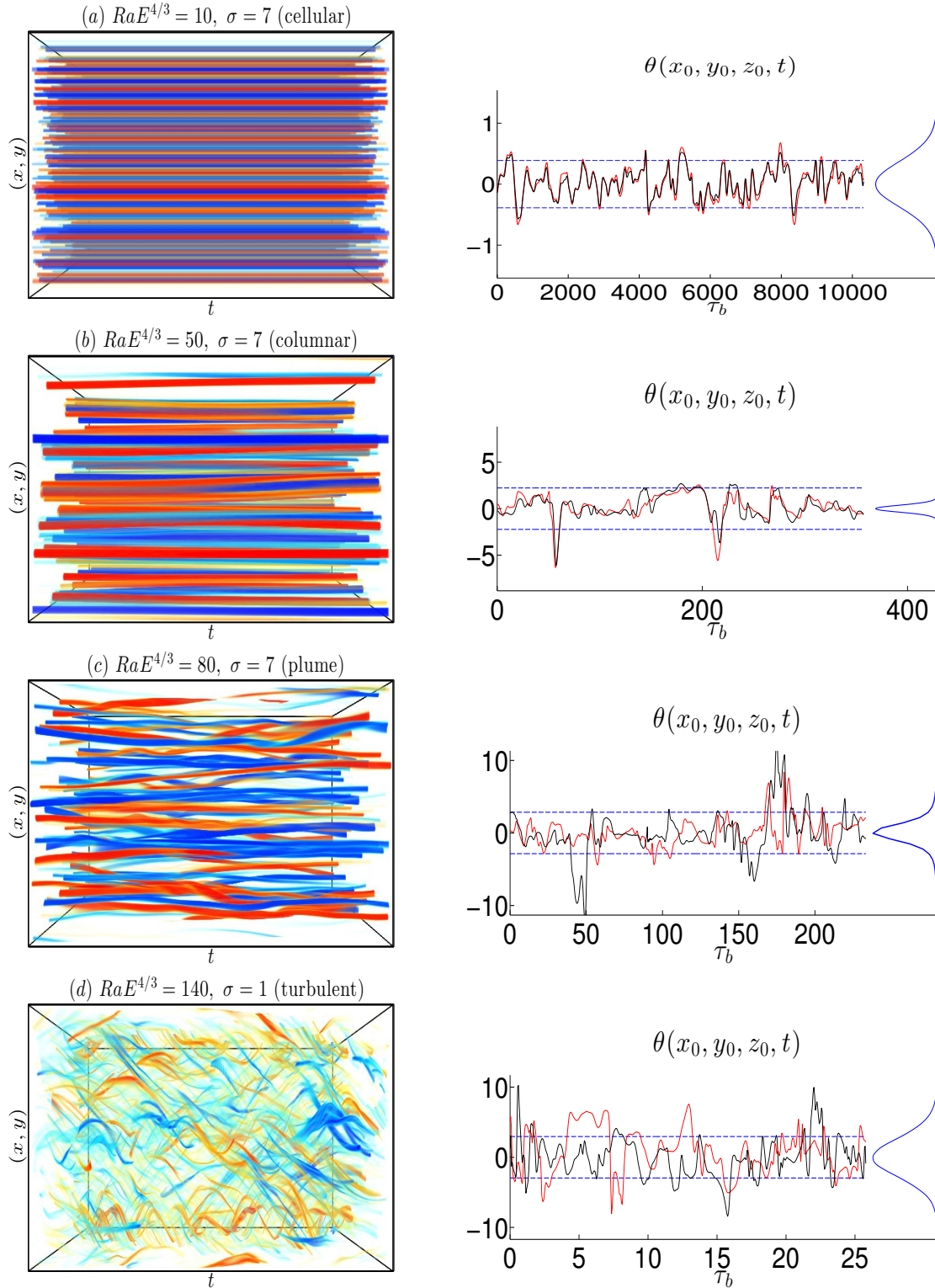
Figure 2.6: Space-time volume rendering of $\theta(x, y, z = 0.8, t)$ evolving in time from left to right for approximately 25 buoyancy times along with sample thermistor data for fixed horizontal positions (x_0, y_0) at $z = 0.2, 0.8$ shown as red and black lines, respectively. Dashed blue lines show the $\pm$ RMS. We note that the time series data for θ (shown on the right) corresponds to the $\mathcal{O}(E^{1/3})$ fluctuating quantity, i.e., experimental fluctuating values should resemble $E^{1/3}\theta$. At the right hand side of each time series a PDF formed from all thermistors at $z = 0.2$ is shown.
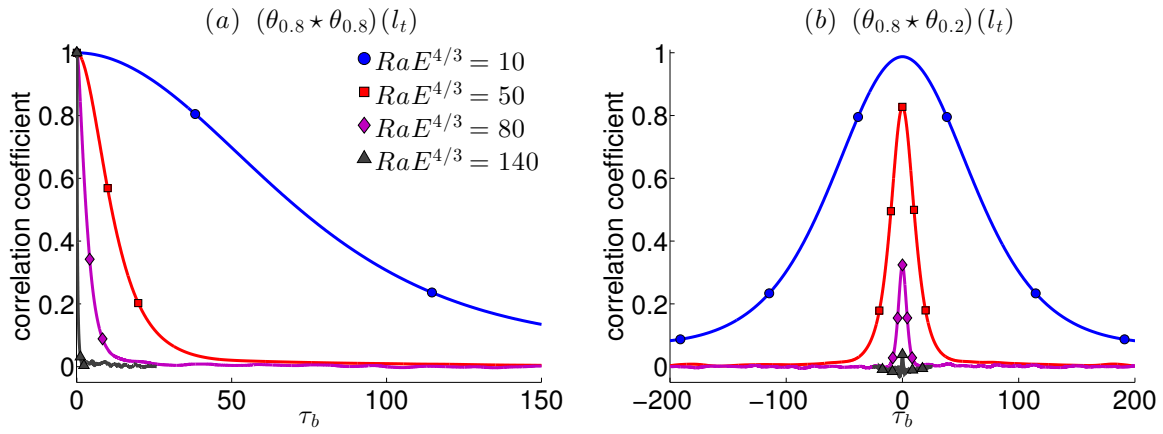
Figure 2.7: Ensemble averaged temporal auto-correlations (a) for signals at $z = 0.8$ and cross-correlations (b) between signals at $z = 0.2$ and 0.8 for θ and for parameters shown in figure 2.1. Decreasing duration of coherence (a) as well as decreased vertical coherence (b) is evident. In this case auto-correlations are even functions and thus only positive displacements are shown for (a). Similar correlation functions are found for vertical velocity and vorticity fields.

thermistor (i.e., structure width divided by the advective velocity U_{coh} of the structure). Table 2.1 summarizes the comparison between advective structure velocities (U_{coh}) to RMS fluid velocities (U_{rms}). For convenience temporal cross-correlations are measured in terms of a relative buoyancy time scale (T_b) which is related to the horizontal viscous time scale $T_\nu = ((Ra - Ra_c)E^{4/3}/\sigma)^{1/2}T_b$, where in this expression the term $Ra - Ra_c$ acts to collapse large viscous times when $Ra - Ra_c < \sigma$ or expand short viscous times when $Ra - Ra_c > \sigma$. The temporal cross-correlation describes the duration of the vertical coherence. For rigid vertical CTC structures we expect these correlations to be near unity at zero lag while we expect a rapid drop in cross-correlation at the transition to plumes through geostrophic turbulence. Spatio-temporal renders in figure 2.6 show the time evolution of a single horizontal plane, $\theta(x, y, 0.8, t)$, for the same parameters as the volume renders in figure 2.1. Displayed beside each render is sample time histories from a pair of thermistors at $Z = 0.2$ and 0.8 along with accompanying probability distribution functions (PDFs). Figure 2.7 shows the auto- and cross-correlations resulting from ensemble averaging across a large number of thermistors or pairs of thermistors, respectively, as described in section 2.2.3. We find very similar temporal correlation functions for vertical velocity and vorticity fields.

The cellular case at $RaE^{4/3} = 10$, $\sigma = 7$ shown in figure 2.6(a) lacks strong horizontal advective motions and coherent structures remain stagnant in time, therefore the duration of vertical coherence is relatively long-lived. The wide auto-correlation in figure 2.7(a) and strong cross-correlation in figure 2.7(b) describe the cellular regime as one of slow modulations in time and space, additionally the PDF of the time series is Gaussian with a kurtosis of 3.14. The CTC flow at $RaE^{4/3} = 50$, $\sigma = 7$ in figure 2.6(b) shows the characteristic physical structure, namely strong thermal cores shielded in a weaker envelope of opposite sign. The cross-correlations in figure 2.7(b) indicates continued strong vertical coherence across the entire fluid layer, however the temporal duration of vertical coherence is significantly decreased from that of the cellular regime. For CTCs the PDF of the time series is no longer Gaussian with kurtosis of approximately 15. From table 2.1 the RMS fluid velocities are seen to be roughly 3 times larger than in the cellular regime. Notably, with exception of the turbulent regime, all advective structure velocities are significantly smaller than the

RMS velocities. At $RaE^{4/3} \approx 55$ the flow transitions from CTCs to plumes and a marked change in the temporal behavior of the flow is seen as the plume regime is reached (figure 2.6(c)). At this point the CTCs have lost their strong oppositely signed shields and the resulting weakly shielded plume structures interact strongly with one another as evident in figure 2.6(c). Figure 2.7(b) shows evidence of vertical coherence across the fluid layer albeit weaker than that measured in the cellular and CTC regimes. Plume ejections from one boundary layer now only weakly synchronize with the opposing boundary layer resulting in columnar structures that are now intermittent in time. Thermal cross-correlations are therefore only registered when an intermittent column is present, hence the small temporal cross-correlation coefficient at zero lag $(\theta_{0.8} \star \theta_{0.2})(l_t = 0)$ in figure 2.7(b). For the turbulent case $(RaE^{4/3} = 140, \sigma = 1)$ the large scale circulation mixes the flow strongly as can be seen in the space-time diagram in Fig 2.6(d). Time signal data across the layer at $Z = 0.2$ and $Z = 0.8$ is uncorrelated $((\theta_{0.8} \star \theta_{0.2})(l_t = 0) = 0.04)$ and the PDF shows fews signs of extreme events, having a kurtosis of 3.15.

As a way of discerning flow regimes the maximum cross-correlation values at zero lag are plotted as a function of $RaE^{4/3}$ in figure 2.8(a) and are similar to the spatial cross-correlations of figure 2.4(b). The cross-correlations between thermal boundary layers are the most sensitive to regime transitions: from figure 2.8(a) we can identify $Ra_c E^{4/3} < RaE^{4/3} \lesssim 20$ as the cellular regime, $20 \lesssim RaE^{4/3} \lesssim 55$ as the CTC regime, and $RaE^{4/3} \gtrsim 55$ as the plume regime. The abrupt transition at $RaE^{4/3} \approx 55$ marks the location where CTCs become unstable and where cross-correlations undergo a sharp decline due to a loss of vertical coherence. This sharp transition is also evident in figure 2.11 where the advective structure velocity scales are given. Figure 2.8(b) shows half-width measurements of the averaged temporal auto-correlations in terms of buoyancy times, along with power-law fits to the regimes shown in figure 2.8(a) and summarized in table A.1 (Appendix). The half-width measurements decrease monotonically within the cellular regime and then the rate of decrease slows within the CTC regime before dropping off rapidly within the plume regime.
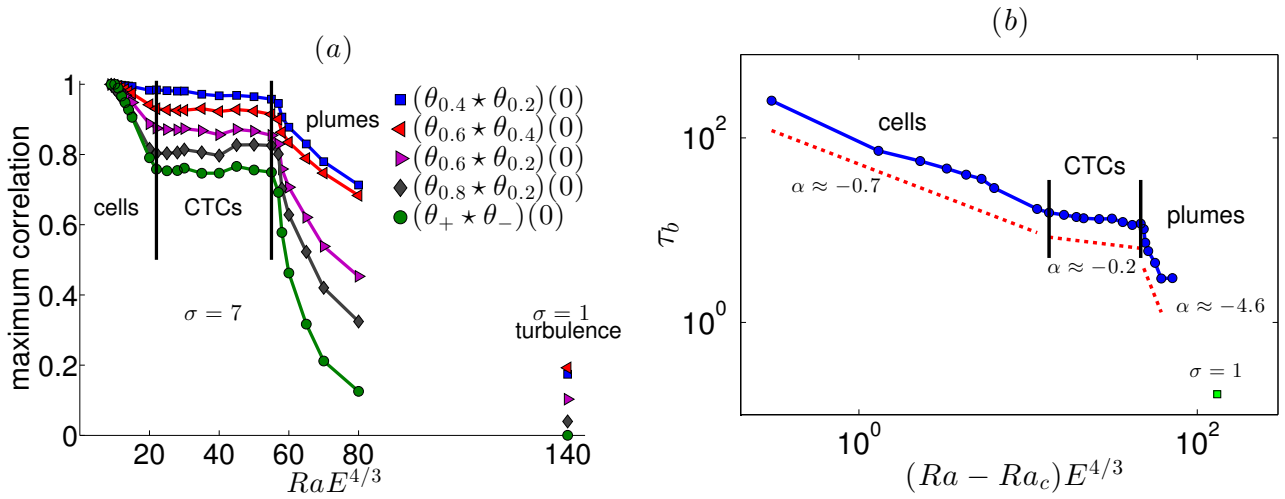
Figure 2.8: (*a*) Temporal cross-correlations at zero time lag as a function $RaE^{4/3}$ clearly marking regimes and regime transitions. (*b*) Half-width measurements of temporal auto-correlations as a function of $(Ra - Ra_c)E^{4/3}$ with power-law-fits (red dotted lines). As $(Ra - Ra_c) \to 0^+$, the time scale $\tau_b \to \infty$ in (*b*). Transitions from cellular to CTC regimes and CTC to plume regimes are identified, however are not so clearly obvious as (*a*).

2.4   Analysis

2.4.1   Direct comparison with spatial structure

A remarkable feature, mentioned in section 2.3.1, of the spatial auto-correlation functions is that they recover the radial structure of the flow (see figure 2.9). To illustrate this we compare ensemble averaged auto-correlations obtained in the four regimes to radial profiles of θ similar to those studied by Grooms et al. (2010). Radial profiles of θ are obtained by first identifying well-formed and well-separated columnar structures. These representative structures are then normalized with respect to the maximum value of θ at each Z-level and azimuthally averaged to obtain radial profiles in the horizontal (Grooms et al., 2010). From figure 2.9, we can see that spatial auto-correlations provide a means to reconstructing the spatial structure in rapidly rotating convection. From flow visualizations it has been observed that vertically coherent structures within a given regime are very similar in horizontal size, shape (i.e., columnar or cylindrical), and magnitude. Therefore, ensemble averaged correlation functions should resemble azimuthally averaged profiles. The variability between the two curves in figure 2.9 can be argued to arise as a consequence of several factors. First, the azimuthally averaged radial profiles are drawn from the mean of well-formed and well-separated columnar structures. Secondly, the profiles obtained from cross-correlating are a consequence of sampling only one spatial direction in the calculation for the ensemble averaged auto-correlation function. Despite minor differences illustrated in figure 2.9, the comparisons suggest a statistical and practical approach to extracting information about the lateral structure in rapidly rotating convection both numerically and experimentally.

2.4.2   Circulation, mass and heat flux

Given that the axisymmetric radial profiles are well resolved and well-approximated by the normalized ensemble averaged spatial auto-correlations, we determine the flow circulation and vertical mass flux by direct evaluation of the integral relations by quadrature. Specifically, within a horizontal plane at height Z we take auto-correlation functions as sufficiently good approximations
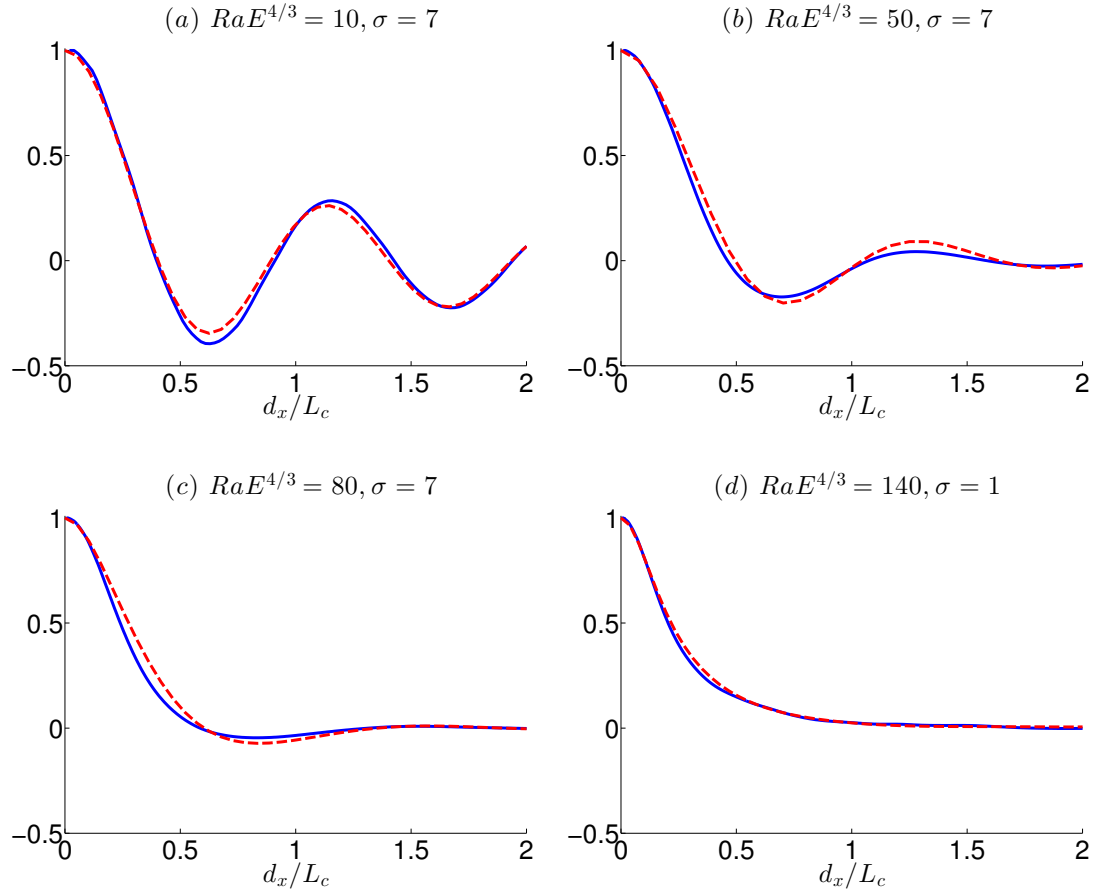
Figure 2.9: Spatial auto-correlation at $Z = 0.2$ (dashed red curve) and the azimuthally averaged radial structure (solid blue curve) for (a) the cellular regime, (b) the CTC regime for well-formed and well-separated CTCs (Grooms et al., 2010), (c) the plume regime, and (d) the geostrophic turbulence regime. For each regime auto-correlations closely resemble radial profiles found by azimuthally averaging well-formed and well-separated columnar structures. Hence, spatial auto-correlations extract the radial structure of the flow.
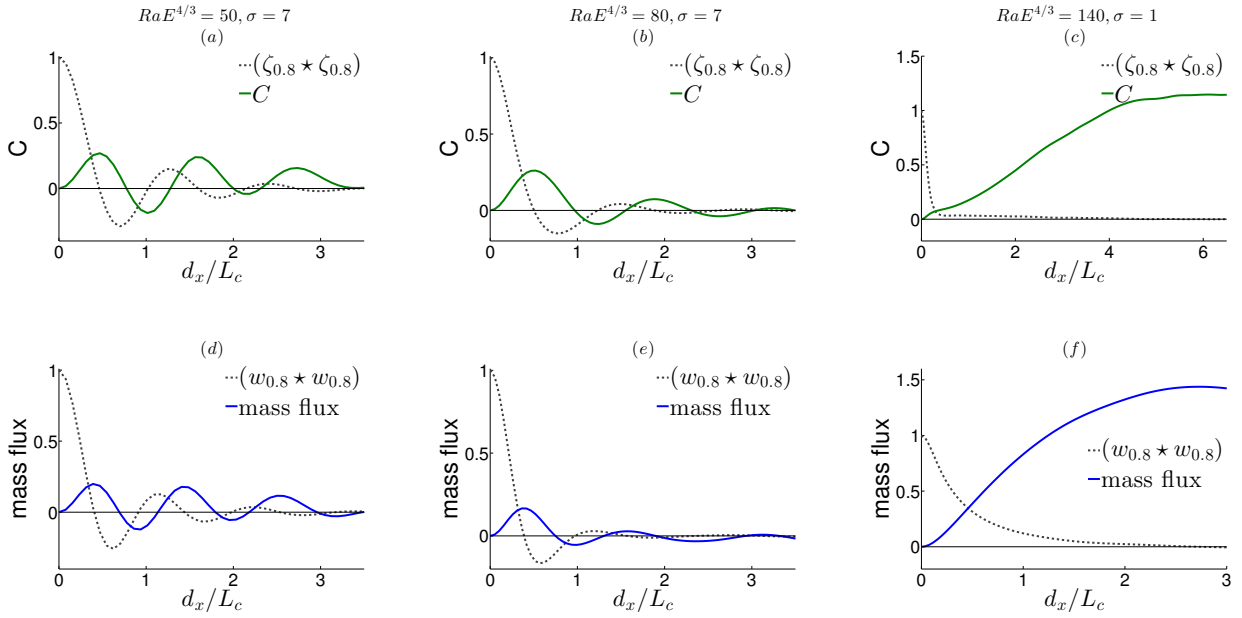
Figure 2.10: Transport properties of coherent structures. The rows show net circulation C and net vertical mass flux (solid lines) for the CTC regime ($RaE^{4/3} = 50$, $\sigma = 7$), the plume regime ($RaE^{4/3} = 80$, $\sigma = 7$), and the turbulent regime ($RaE^{4/3} = 140$, $\sigma = 1$). Each is calculated by interpreting spatial auto-correlations at $Z = 0.8$ for ζ and w as axisymmetric radial profiles. The dotted curves are the corresponding auto-correlations at $Z = 0.8$.

to radial profiles of vorticity and vertical velocity, i.e. $\zeta(x, y, Z) \approx (\zeta_Z \star \zeta_Z)(r, Z)$ and $w(x, y, Z) \approx (w_Z \star w_Z)(r, Z)$. With this approximation we may estimate fluid circulation and vertical mass flux by evaluating the integrals

$$\iint (\nabla \times \boldsymbol{u}) \cdot \hat{\boldsymbol{z}} dS = 2\pi \int_0^{d_x/L_c} r(\zeta_{0.8} \star \zeta_{0.8})(r) dr, \tag{2.13}$$

$$\iint \boldsymbol{u} \cdot \hat{\boldsymbol{z}} dS = 2\pi \int_0^{d_x/L_c} r(w_{0.8} \star w_{0.8})(r) dr, \tag{2.14}$$

respectively. Here, we present circulation and fluxes at $Z = 0.8$. Figure 2.10 shows these quantities for the CTC, plume and geostrophic turbulence regimes. Within the CTC and plume regimes the net circulation (figure 2.10(a, b)) goes to zero at about 3.5 critical length scales, indicative of isolated structure that weakly interacts with its surroundings (illustrated in figure 2.6(b, c)). Similar behavior is seen for vertical mass flux (figure 2.10(d, e)) indicating a balance between upwelling and downwelling flow over a lateral domain spanning about 3.5 critical lengths.

As the turbulent regime is approached net circulation becomes non-zero, saturating to a value of approximately 1.1 at roughly 5 critical lengths. In this regime CTCs and plumes have lost their shielding which results in vortices with strong velocity circulations that lead to strong vortex-vortex interactions. The vertical mass flux is non-trivial and saturates to approximately 1.4 at roughly 3 critical lengths. This indicates that columnar structures are no longer isolated entities and are connected to the global fluid flow. The scale at which net circulation saturates in comparison to mass flux communicates the scale disparity seen between the large scale circulation and the physical mechanisms that transport mass vertically (Julien et al., 2012a).

2.4.3 Characteristic scales

As mentioned above, temporal cross-correlations measures the time for coherent structure to be advected across a thermistor. Advective velocity scales may now be estimated by using the half-width measurements provided by spatial and temporal auto-correlations as representative width of a structure and advective structure time scales, respectively. An example of the advective velocity scale using data provided in figure 2.4(a) and figure 2.8(b) is shown in figure 2.11(a) along
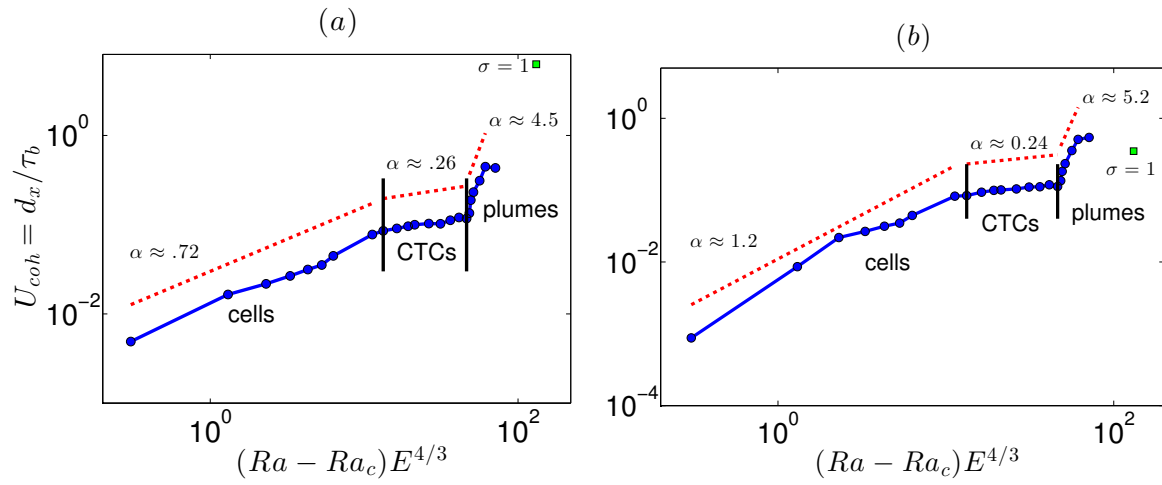
Figure 2.11: Advective structure-velocity scales based on spatial and temporal auto-correlations as a function of $(Ra - Ra_c)E^{4/3}$ at (a) the interior location $Z = 0.8$ and at (b) the top TBL with power-law-fits (red dotted lines) given for each regime outlined in table A.1 (Appendix) and identified in figure 2.8(a).

with scaling exponent fits (also, see tables A.1 and A.2 in the Appendix). These advective velocity scales are seen to increase monotonically across all regimes, however, we note the strong increase in advective velocity in the plume regime is a consequence of strong vortex-vortex interactions. A similar analysis yielding similar results is carried out for spatial and temporal half-widths taken at the top TBL (see figure 2.11(b)).

2.4.4   Correlation convergence

As mentioned in section 2.2.3, temporal cross-correlations considered are the result of ensemble averaging over a large number of thermistor (auto-correlation) or thermistor pair (cross-correlation) locations in the horizontal. The large number of spatial samples in (x, y) embedded in the ensemble averaging is equivalent to long duration samples in time at a single horizontal spatial location. Statistical stationarity and isotropy indicate that the accumulation of averages over large time intervals are equivalent to ensemble averages over many horizontal spatial locations (Sprague et al., 2006). If the number of thermistors or thermistor pair time signals of duration τ_e used in an ensemble average is N_t then we find that the uniform convergence of temporal cross-correlations goes roughly as $CN_t^{-\beta}$, where our fittings find values of C of about 0.7 and β of approximately 0.55 (with signal duration ranging from $\mathcal{O}(10^4)$ to $\mathcal{O}(10^0)$ viscous times from the cellular to geostrophic regime, respectively). Hypothetically, if a uniform error of $\varepsilon = 0.025$ is to be obtained then N_t must be chosen such that $N_t = (\varepsilon/C)^{-1/\beta}$. With the values of C and β above, such an error demands $N_t \approx 428$ in the ensemble average. To illustrate the total duration of an experimental time signal $(\tau_e \times N_t)$ needed to emulate results presented here, consider the experimentally accessible (King and Aurnou, 2012) parameters: $E = 2.5 \times 10^{-6}$, $H = 0.032m$, and $\nu = 1.5 \times 10^{-6} m^2/s$. With these choices the viscous time scale becomes $T = L^2/\nu = E^{2/3}H^2/\nu \approx .1257s$ (having used the anisotropic aspect ratio (Sprague et al., 2006; Julien et al., 2006) $A_Z = H^*/L^* = E^{-1/3}$). With the values of T and N_t as above one can determine the total duration of an experimental time signal $\tau_s = TN_t\tau_e$ (where τ_e is the signal duration in viscous times). Based on the duration of signals used to determine the results presented in this paper, values of τ_s are found and presented in table 2.2.

Table 2.2: Estimates for experimental signal duration based on flow regime and the experimentally accessible values $E = 2.5 \times 10^{-6}$, $H = 0.032m$, and $\nu = 1.5 \times 10^{-6} m^2/s$. Intervals for total signal duration τ_s (ensemble time signal duration times the number of thermistors or thermistor pairs, i.e., $\tau_e T \times N_t$) are shown for each regime: cellular ($RaE^{4/3} \in [8.6956, 22]$), CTC ($RaE^{4/3} \in [22, 55]$), and plume $RaE^{4/3} > 55$, each for $\sigma = 7$, and geostrophic turbulence for $RaE^{4/3} = 140$ and $\sigma = 1$.

regime	cellular	columnar	plume	geostrophic turbulence
τ_s	$[7.8, 2.6]$ days	$[2.6 \text{ days}, 4.7 \text{ hours}]$	$\lesssim 4.7$ hours	≈ 2.0 min

2.5   The effects of thermal boundary conditions

Here we briefly describe a related problem in which rapidly rotating Rayleigh-Bénard convection is again the focus, however with a modification to the thermal boundary conditions. In the above we have made use of fixed temperature boundary conditions which presumes the existence of physical boundaries that are perfectly conducting; this is likely not the case for geophysical and astrophysical applications and certainly not true for laboratory experiments. In fact, in laboratory settings the thermal boundary conditions more closely resemble fixed flux thermal boundary conditions where the temperature gradient normal to the boundary surface is very nearly held fixed. Such considerations naturally bring into question the validity and relevance of the identification of coherent structures provided above in the presence of fixed thermal boundary conditions. Motivated by this we consider the dynamical consequence on rapidly rotating Rayleigh-Bénard convection in the presence of fixed flux thermal boundary conditions and compare with results of fixed thermal boundary conditions.

To differentiate between discussions of these two problems we introduce notation regarding the definition of the Rayleigh number. For a fluid with thermal expansivity α, kinematic viscosity ν and thermal diffusivity κ, the non-dimensional Rayleigh number quantifies the strength of the buoyancy force. For the fixed temperature (FT) conditions and the fixed flux (FF) conditions we have, respectively, appropriate definitions for the Rayleigh number

$$Ra_{FT} = \frac{g\alpha\Delta T H^3}{\nu\kappa}, \quad Ra_{FF} = \frac{g\alpha\beta H^4}{\nu\kappa}, \tag{2.15}$$

as before ΔT is the fixed temperature difference between the top and bottom boundaries and β is

the fixed temperature gradient maintained at the boundaries. Upon defining the non-dimensional measure of heat transfer via the Nusselt number,

$$Nu = \frac{\text{total heat transfer}}{\text{conductive heat transfer}} = \frac{\beta H}{\Delta T}, \tag{2.16}$$

it is straightforward to show that the two Rayleigh numbers defined above are related simply by $Ra_{FF} = NuRa_{FT}$. We see that for linear convection in which $Nu \equiv 1$ the two Rayleigh numbers are equivalent. For nonlinear convection in which the critical Rayleigh number has been surpassed, $Nu > 1$ is achieved by adjustment of the temperature gradient β at fixed ΔT for FT boundaries, and vice versa for FF boundaries.

As before, a pure conduction state $\overline{T} = 1 - Z$ is used for both sets of thermal boundary conditions, therefore the fluctuating thermal boundary conditions become

$$\theta = 0, \quad \text{at} \quad Z = 0, 1, \quad (FT) \tag{2.17}$$

$$\partial_Z \theta = 0, \quad \text{at} \quad Z = 0, 1. \quad (FF) \tag{2.18}$$

Stress-free, impenetrable mechanical boundary conditions on the top and bottom boundaries are assumed throughout and given by

$$w = \partial_Z u = \partial_Z v = 0, \quad \text{at} \quad Z = 0, 1. \tag{2.19}$$

A boundary layer analysis given by Calkins et al. (2015) shows the leading-order system satisfies fixed temperature boundary conditions implicitly, however double boundary layer structure is necessary to satisfy fixed flux thermal boundary conditions. The boundary layers consist of an inner Ekman layer adjacent to the solid boundaries that adjust viscous stresses to zero, and a middle layer in thermal wind balance adjacent to the Ekman inner layers that adjusts the normal derivative of the temperature fluctuation to zero. The induced vertical mass flux via Ekman pumping is shown to be asymptotically weak and implies that studies employing FT thermal boundary conditions accurately describe FF thermal boundary conditions as long as the Rossby number remains small.

In light of the boundary layer analysis, we conclude that the leading order quasi-geostrophic dynamics are described by equations (2.7a)–(2.7d) for *both* FT and FF thermal boundary conditions.

Indeed, inspection of the system shows that it is invariant under the following rescaling of the Rayleigh numbers and temperature variables,

$$\widetilde{Ra}_{FT} = \frac{\widetilde{Ra}_{FF}}{Nu}, \quad \theta_{FT} = Nu\,\theta_{FF}, \quad \overline{T}_{FT} = Nu\,\overline{T}_{FF}. \tag{2.20}$$

Integrating the time-averaged mean heat equation with respect to Z yields

$$Pr\overline{(w\theta_{FT})} = \partial_Z \overline{T}_{FT} + Nu, \quad (FT) \tag{2.21}$$

$$Pr\overline{(w\theta_{FF})} = \partial_Z \overline{T}_{FF} + 1, \quad (FF) \tag{2.22}$$

for the FT and FF cases, respectively. The appropriate thermal boundary conditions have been applied at $Z = 0$ in the above relations. Taking either equation (2.21) or (2.22) and utilizing (2.20) shows that the mean interior temperature gradient is described by identical equations for the two cases. This leading order correspondence is the result of the anisotropic spatial structure of rapidly rotating convection.

The above results indicate that the findings of previous work on small Rossby number convection employing FT thermal boundary conditions can be accurately applied to the case of FF thermal boundary conditions by use of the rescalings given by equations (2.20). Julien et al. (2012a) identified four flow regimes that occur in rapidly rotating convection as a function of the Prandtl and (FT) Rayleigh numbers. The convective Taylor column (CTC) regime is distinguished by coherent, vertically aligned convective structures that span the depth of the fluid. Figure 2.12(a) shows a volumetric rendering of the temperature perturbation for $Pr = 7$ and $\widetilde{Ra}_{FT} = 46.74$, or $\widetilde{Ra}_{FF} = 1000$ and $Nu = 21.39$; this case was computed explicitly with FF thermal boundary conditions. The CTC regime occurs over the FT Rayleigh number range of $20 \lesssim \widetilde{Ra}_{FT} \lesssim 55$, corresponding to a FF Rayleigh number range of $82 \lesssim \widetilde{Ra}_{FF} \lesssim 1656$ (see figure 2.4a and 2.8b above). Figure 2.12(b) shows mean temperature profiles obtained utilizing the FT and FF thermal boundary conditions, along with the remapped FF mean temperature profile. The Nusselt number $Nu = 21.39$ corresponds to a mean temperature difference of 0.0468 between the top and bottom boundaries for the FF case. Given that the mapping defined by equation (2.20) is independent of
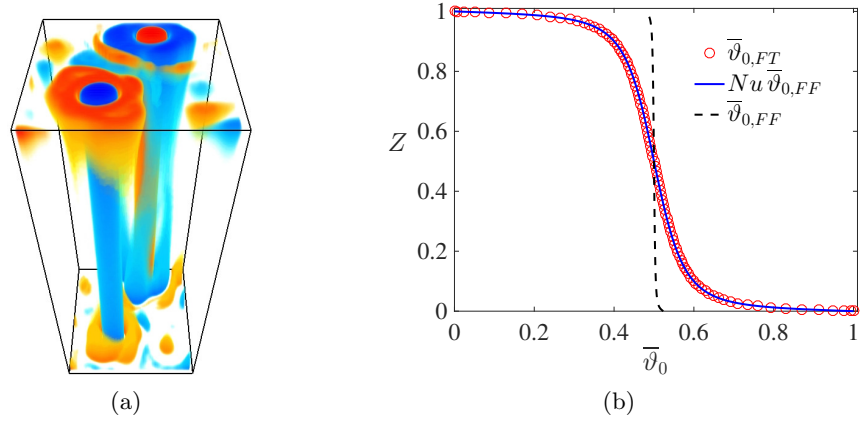
Figure 2.12: (a) An example volumetric rendering of the temperature perturbation from a simulation of the NH-QG convection equations showing the convective Taylor column (CTC) regime computed explicitly with FF boundary conditions. (b) Mean temperature profiles obtained with both FT (solid blue) and FF (dashed black) boundary conditions, and the rescaled FF temperature profile (red open circles). The parameters are Pr $= 7$, $\widetilde{Ra}_{FT} = 46.74$, $\widetilde{Ra}_{FF} = 1000$, and $Nu = 21.39$.

the Prandtl number, we note that the rescaling shown in Figure 2.12(b) can be carried out for any Prandtl number.

Of particular interest in convection studies is the dependence of the heat transfer scaling with the strength of the thermal forcing input via Nusselt-Rayleigh number scalings of the form $Nu \sim \widetilde{Ra}_{FT}^{\alpha}$. With the rescaling given in (2.20) the FF equivalent of this relation becomes $Nu \sim \widetilde{Ra}_{FF}^{\beta}$ where $\beta = \alpha/(\alpha + 1)$. For the CTC regime the exponent is $\alpha \approx 2.1$ (Julien et al., 2012a), yielding $\beta \approx 0.68$. Additionally, the final regime of geostrophic turbulence achieves a dissipation-free scaling law with $\alpha = 3/2$ such that $\beta = 3/5$ (Julien et al., 2012a). Similarly, the dependence of all other variables of interest on the Rayleigh number (e.g. mean temperature gradient, vorticity, etc.) can also be remapped to the case of FF thermal boundary conditions.

2.6   Conclusions

A statistical survey of auto- and cross-correlations that quantify the vertical coherence in rotationally constrained Rayleigh-Bénard convection has been presented. Notably, the strategies presented in this chapter can be utilized for both experimental and DNS data in the rotationally constrained regime, i.e., in the limit of $E, Ro \ll 1$. While these techniques have been employed in related studies on non-rotating convection (Kunnen, 2008) and electromagnetically forced rotating turbulence(van Bokhoven et al., 2009), these techniques are not presently used in rotationally constrained Rayleigh-Bénard convection where heat transport (i.e., the Nusselt number) still remains the most experimentally utilized investigative tool in assessing the flow morphology. Remarkably, the spatial auto-correlations capture the radial profile of coherent structures obtained from the numerical solutions of rapidly rotating Rayleigh-Bénard convection. The evolution of the flow morphology and the transition between flow regimes are readily identified in the analysis: the transition from the cellular regime to the CTC regime is seen to occur near $RaE^{4/3} \approx 20$, while the transition from the CTC regime to the plume regime is seen to occur at $RaE^{4/3} \approx 55$ (see figure 2.8(a)). The identification of these transitions in the flow morphology are observed from both ensemble averaged spatial and temporal cross-correlations and for each field variable θ, ζ, and w. Moreover,

the transitions are most easily identified by considering correlation values at zero lag for vertically well-separated fluid signals. These transitions provide a further refinement to the work of Julien et al. (2012a).

From half-width measurements of ensemble averaged spatial and temporal cross-correlations advective velocities for vertically coherent structures are obtained. These measurements are seen to follow a power-law $\beta(\widetilde{Ra} - \widetilde{Ra_c})^{\alpha}$, where α is seen to depend upon the $RaE^{4/3}$ as outlined in table A.1 and table A.2 in the appendix. Moreover, these advective velocities evolve from a state of nearly static motion towards the motions similar to the vigorous RMS velocities as the geostrophic turbulent regime is approached (see table 2.1 and figure 2.11).

Spatial auto-correlations are used to extract radial profiles and study net circulation and mass flux (figure 2.10). The transition from weakly interacting structures in the cellular, CTC, and plume regimes to strongly interacting structures in the geostrophic turbulent regime can be identified by a net circulation that saturates to zero to a net circulation that saturates to a non-zero value, respectively.

We have shown that the leading order dynamics of rapidly rotating convection in a plane layer geometry are equivalent for FT and FF thermal boundary conditions. FF thermal boundary conditions give rise to a double boundary layer structure in the limit of rapid rotation that induces a vertical mass flux, via Ekman pumping. The Ekman pumping velocity is asymptotically weak, therefore we conclude that previous work employing FT thermal boundary conditions also accurately describes FF thermal boundary conditions as long as the Rossby number remains small.

Recently, the influence of both thermal and mechanical boundary conditions on non-rotating convection has received significant attention (e.g. Johnston and Doering, 2009; van der Poel et al., 2014). For plane layer rotating convection investigations have shown that no-slip and stress-free mechanical boundary conditions yield similar convective dynamics (King et al., 2009; Schmitz and Tilgner, 2010), however, the presence of Ekman pumping occurs for no-slip boundary conditions and is now known to significantly enhance heat transfer relative to stress-free boundary conditions (Kunnen et al., 2006; Stellmach et al., 2014). At present, studies investigating the role of ther-

mal boundary conditions on nonlinear rotating convection have been focused solely on spherical geometries. Zhang and Gubbins (1993) showed that convection cells in a rotating spherical shell can resonate with spatially inhomogeneous temperature boundary conditions. A subsequent investigation by Davies et al. (2009) has shown that resonance is dependent upon both the rotation rate and the spatial scale of the thermal anomaly along the outer boundary, with resonance vanishing when the scale of the temperature variation is comparable to the most unstable wavelength and the rotation rate of the system is large. Our asymptotic analysis complements these previous numerical findings and rigorously shows that any horizontal thermal variation along the boundaries that varies on the scale of the convection, as allowed for with FF thermal boundary conditions, has no leading order influence on the interior convection. However, we note that resonance can occur when the spatial scale of the thermal anomaly is comparable to the vertical scale of convection (Davies et al., 2009); this is the mechanism likely to cause significant changes in the magnetic and velocity fields observed in spherical dynamo simulations with FF boundary conditions (Sakuraba and Roberts, 2009, 2011). For a complete description of the investigation on the effects of thermal boundary conditions for rapidly-rotating convection see Calkins et al. (2015). This work was done in collaboration with Mike Calkins, Keith Julien, Kevin Hale, and Derek Driggs.

Chapter 3

Investigations of Rapidly Rotating and Stably Stratified Flow

3.1   Introduction

The study of fluid turbulence connects bulk statistical properties like energy spectra, structure functions, and the energy dissipation rate to physical processes like vortex stretching and instabilities (Frisch, 1995). In the context of geophysical turbulence, the emphasis is on how rotation and density stratification affect the statistical and dynamical properties of the turbulent flow. At small scales rotation and buoyancy are expected to become dynamically unimportant, with statistics resembling those of non-rotating, constant-density flow. More specifically, rotation and buoyancy respectively are expected to become unimportant for length scales smaller than the Zeman scale $L_\Omega = \sqrt{\epsilon/(2\Omega)^3}$ (Zeman, 1994) and the Ozmidov scale $L_N = \sqrt{\epsilon/N^3}$ (Ozmidov, 1965) where ϵ is the mean rate of energy dissipation per unit mass, Ω is the rate of rotation, and $N = \sqrt{-g\partial_z\rho/\rho_0}$ is the buoyancy frequency in a density-stratified fluid under the Boussinesq approximation (g is the gravitational acceleration, ρ is the density, and ρ_0 is a constant reference density). Studies of geophysical turbulence therefore include scales larger than either the Ozmidov or Zeman scales, or both.

Rotation and stratification induce restoring forces that lead to wave dynamics; when the axis of rotation is parallel to gravity, the linear wave spectrum includes frequencies between N and 2Ω. Waves with no vertical vertical variability are pure gravity waves (where gravity alone acts as the restoring force) with frequency N. Waves with no horizontal variability are pure inertial waves (where the restoring force is the "fictitious" inertial Coriolis force) with frequency

2Ω. Rotation and stratification are expected to have a qualitative impact on turbulence when the period of wave dynamics is comparable to or less than the time scale of nonlinear advection. More precisely, rotation and stratification respectively are expected to strongly affect the dynamics when the Rossby number Ro $= U/(2\Omega L)$ and Froude number Fr $= U/(NL)$ are small, where U and L are characteristic velocity and length scales of the turbulent flow. Geophysical turbulence is characterized by small Rossby and/or Froude numbers.

The linear eigenfunctions of the Boussinesq system include two wave modes and a zero-frequency 'vortical' mode (Bartello, 1995). At low Rossby and Froude numbers there is a clear time scale separation between the slow, nonlinear evolution of the vortical mode and the fast, weakly-nonlinear evolution of the wave modes which can be exploited to derive asymptotically a reduced set of dynamics for the vortical modes; this reduced system is the celebrated quasigeostrophic equations (Eady, 1949; Charney, 1948; Pedlosky, 1987; Vallis, 2006b). Time scale separation was exploited by Embid and Majda to rigorously prove the validity of the quasigeostrophic system even in the presence of wave modes with amplitudes comparable to the vortical modes, in contrast to the asymptotic derivation which assumes that any waves have low amplitude (Embid and Majda, 1996, 1998; Majda and Embid, 1998). Temam and Wirosoetisno (2010, 2011) have also proven rigorously that, under mild assumptions, the small-Rossby, small-Froude dynamics eventually approaches a quasigeostrophic balance irrespective of the amplitude of wave modes in the initial condition. The quasigeostrophic system is thus a natural touchstone for geophysical turbulence, and the qualitative properties of turbulence in the quasigeostrophic system were presciently forecast by Charney (1971) based on an analogy with previous studies of two-dimensional turbulence.

The rigorous framework of Embid and Majda (1996) exploits an asymptotic time scale separation between the fast wave dynamics and the slow 'balanced' dynamics. Embid and Majda (1998) and Wingate et al. (2011) also used the framework to rigorously derive equations governing the slow limiting dynamics in the limits of low Froude and finite Rossby numbers, and low Rossby and finite Froude numbers, respectively. Because of the need for an asymptotic time scale separation, the slow limiting dynamics include a single pair of wave modes at the slowest linear frequency (2Ω for

Embid and Majda (1998) and N for Wingate et al. (2011)) and all other wave modes are assumed to be asymptotically fast by comparison, and do not appear in the slow limiting dynamics. Results analogous to those of Temam and Wirosoetisno (2010) for the quasigeostrophic system are lacking for these two systems of slow limiting dynamics, and it is not yet clear whether these systems have the same relevance for geophysical turbulence in their respective asymptotic regimes as the quasigeostrophic system has for the low-Froude, low-Rossby number regime.

If either the Rossby or Froude number is order-one, there is not a clear time scale separation between the linear wave dynamics and the nonlinear advective dynamics, so a reduced system that eliminates nearly all the wave dynamics is arguably inappropriate. Nevertheless, the smallness of one of the nondimensional numbers can still be exploited in both cases to reduce the complexity of the full Boussinesq system. When the Froude number is small but the Rossby number is order-one one can make the hydrostatic approximation to arrive at the so-called primitive equations. When the Rossby number is small but the Froude number is order-one one can make a geostrophic approximation and arrive at the non-hydrostatic quasigeostrophic equations (NHQGE; Julien et al., 1998, 2006). Both of these equation sets are significantly easier for both numerical simulation and mathematical analysis than the unreduced Boussinesq equations, and both sets of equations include linear wave dynamics with frequencies between either 2Ω (primitive equations) or N (NHQGE) and infinity. The quasigeostrophic equations can be recovered from both sets of equations in the limit where both the Rossby and Froude numbers are small.

As the Froude number is typically smaller than the Rossby number in atmospheric and oceanic turbulence, studies of rotating, stratified turbulence have primarily focused on strongly-stratified regimes where the Froude number is small. The regime of geostrophic turbulence with low-Rossby number and order-one Froude number has seen comparatively little study, though this regime is relevant to weakly stratified abyssal ocean dynamics at high latitudes and in the western Mediterranean (Emery et al., 1984; Timmermans et al., 2003; van Haren and Millot, 2005; Timmermans et al., 2007). The regime is also relevant to planetary and stellar interiors where the stratification transitions from unstable (imaginary N) to stable ($N \geq 0$). Examples include the

solar tachocline believed to be the origin of large scale solar magnetism (Miesch, 2005) and the Earth's outer liquid core where the existence of stably-stratified layers have been postulated (Pozzo et al., 2012). The present investigation focuses on rotating, stratified turbulence at low Rossby number, with Froude numbers varying from large to small.

The main points of comparison for the transitional regime of Froude numbers between zero and infinite are the 'quasigeostrophic' regime at small Froude numbers and pure rotation at large Froude numbers. Quasigeostrophic turbulence theory, by analogy with the theory of two-dimensional turbulence (Boffetta and Ecke, 2012), predicts a transfer of energy from the forcing scale to larger scales through an inertial range where the energy spectrum is proportional to $\tilde{k}^{-5/3}$, where $\tilde{k}^2 = k_h^2 + (2\Omega/N)^2 k_z^2$. At scales smaller than the energy forcing quasigeostrophic turbulence theory predicts an energy spectrum proportional to $\tilde{k}^{-3}$. The $-5/3$ (Smith and Waleffe, 2002; Marino et al., 2013) and -3 (Waite and Bartello, 2006) spectral slopes are evident in simulations of triply periodic Boussinesq dynamics in the regime of low Rossby and Froude numbers, and both Waite and Bartello (2006) and Whitehead and Wingate (2014) observed energy accumulating in the vortical modes. These results underscore the importance of quasigeostrophic dynamics, and demonstrate that the theorem of Temam and Wirosoetisno (2010) applies qualitatively even in this stochastically-forced regime.

In simulations of constant-density (infinite Froude number) low-Rossby number turbulence energy is transferred to scales larger than the forcing scale through an inertial range with spectrum proportional to k^{-3}; energy is also primarily transferred to a depth-independent horizontal velocity, the 'barotropic mode' (Smith and Waleffe, 1999; Smith and Lee, 2005). Marino et al. (2013) found transfer of energy into the barotropic mode to be less rapid in the purely rotating regime than in the quasigeostrophic regime. Sen et al. (2012) observed a $k^{-5/3}$ spectrum at large scales in a purely rotating system when the stochastic forcing was depth-independent; this case is somewhat degenerate and likely not indicative of universal behavior.

The transitional regime between pure rotation and quasigeostrophy has seen comparatively few simulations. In the experiments of Sukhatme and Smith (2008) the Froude and Rossby num-

bers are both comparatively small, though in some experiments the Froude number was larger by up to a factor of 5. In their experiments with Froude number larger than Rossby number the wave mode energy grows to dominate, in contrast to the behavior in both the quasigeostrophic and purely-rotating limits where energy accumulates primarily in the vortical and depth-independent components; this may be related to the fact that forcing was applied near the scale of the computational domain. They found that the vortical mode spectrum retained its quasigeostrophic k^{-3} behavior at scales smaller than the forcing, though it deviated towards a shallower slope at much smaller scales. In a single experiment with low Rossby number and moderate Froude number, also forced near the scale of the computational domain, Aluie and Kurien (2011) diagnosed a downscale transfer of both energy and potential enstrophy; spectral slopes were not reported. Whitehead and Wingate (2014) also forced near the scale of the computational box, and found energy accumulating in the barotropic mode; spectral slopes were not reported. These investigations leave open entirely the question of how the large scale dynamics transition between the quasigeostrophic and purely rotating regimes as the Froude number increases, which is the focus of the present investivation.

This chapter is organized as follows: §3.2 introduces preliminaries including discussions regarding Proudman-Taylor constraints and inertia-gravity waves, §3.3 provides an overview of the reduced equations used in our numerical simulations, §3.4 summarizes the numerical methods including the forcing scheme employed for numerical simulations, and §3.5 gives the results of our numerical experiments.

3.2   Governing Equations and Preliminaries

We consider an incompressible fluid subject to an imposed constant vertical gravitational field $\boldsymbol{g} = -g\hat{\boldsymbol{z}}$ and a system rotation with constant angular velocity $\boldsymbol{\Omega} = \Omega\hat{\boldsymbol{z}}$. The fluid is stably-stratified in the vertical with total density $\rho^* = \hat{\rho}^*(z^*) + \rho'^*(\boldsymbol{x}^*, t^*)$, where $\hat{\rho}^*(z^*) = \rho_0^* + \delta\hat{\rho}^*(z^*)$ is an ambient density profile consisting of a constant reference density ρ_0^* and a density variation $\delta\hat{\rho}^*(z^*)$ (where asterisks denote dimensional quantities). It follows that the total buoyancy of a

fluid parcel, given by

$$b^* = -\frac{g}{\rho_0^*}\left(\delta\hat{\rho}^*(z^*) + \rho'^*(\boldsymbol{x}^*, t^*)\right) = -\frac{g}{\rho_0^*}\delta\hat{\rho}^*(z^*) + b^{*\prime}(\boldsymbol{x}^*, t^*), \tag{3.1}$$

is decomposed as the sum of the ambient buoyancy field and a fluctuating component $b^{*\prime}$ associated with fluid motions. Pressure is decomposed in a fashion similar to buoyancy $p^* = \hat{p}^*(z^*) + p'^*(\boldsymbol{x}^*, t^*)$ with an ambient pressure component in hydrostatic balance with the ambient buoyancy

$$\partial_{z^*}\delta\hat{p}^*(z^*) = -g\hat{\rho}^*(z^*). \tag{3.2}$$

The governing equations in the Boussinesq approximation for a fluid with constant kinematic viscosity ν and buoyancy diffusion κ are given by

$$D_t^*\boldsymbol{u}^* + 2\Omega\hat{\boldsymbol{z}} \times \boldsymbol{u}^* = -\nabla p^{*\prime} + b^{*\prime}\hat{\boldsymbol{z}} + \nu\nabla^{*2}\boldsymbol{u}^*, \tag{3.3a}$$

$$D_t^*b^{*\prime} + N^2(z^*)w^* = \kappa\nabla^{*2}b^{*\prime}, \tag{3.3b}$$

$$\nabla^* \cdot \boldsymbol{u}^* = 0. \tag{3.3c}$$

where

$$D_t^*(\cdot) = \left[\partial_{t^*} + \boldsymbol{u}^* \cdot \nabla^*\right](\cdot). \tag{3.4}$$

The ambient stratification is now characterized by the buoyancy (Brunt-Väisälä) frequency $N^2(z^*) = -g\rho_0^{*-1}\partial_{z^*}(\delta\hat{\rho}^*(z^*))$.

An external forcing is required to excite fluid motions, and in the present investigation energy is generated by a stochastic vertical velocity forcing. Recent studies in a similar parameter regime have used stochastic buoyancy forcing (Whitehead and Wingate, 2014) while other studies perform simultaneous forcing of all components of velocity (Marino et al., 2013). The present investigation includes regimes of weak stratification (large Froude numbers) and initial tests with buoyancy forcing in the weakly-stratified regime led to frequent large-scale overturning. Vertical velocity forcing avoids these spurious dynamics in the weakly-stratified regime while also avoiding direct forcing of the slow quasigeostrophic dynamics in the strongly-stratified regime.

Characteristic scales determined from the energy injection rate ϵ_f^* and forcing length scale L_f^* are the forcing velocity, time, and buoyancy scales

$$U_f^* = \left(\epsilon_f^* L_f^*\right)^{1/3}, \quad T_f^* = \left(L_f^{*2}\epsilon_f^{*-1}\right)^{1/3}, \quad B_f^* = \left(\epsilon_f^{*2}L_f^{*-1}\right)^{1/3}. \tag{3.5}$$

This gives rise to the following nondimensional equations

$$D_t\boldsymbol{u} + \frac{1}{Ro_f}\hat{\boldsymbol{z}} \times \boldsymbol{u} = -Eu_f\nabla p + b\hat{\boldsymbol{z}} + \frac{1}{Re_f}\nabla^2\boldsymbol{u}, \tag{3.6a}$$

$$D_t b + \frac{1}{Fr_f^2}S(z)w = \frac{1}{\sigma Re_f}\nabla^2 b \tag{3.6b}$$

$$\nabla \cdot \boldsymbol{u} = 0, \tag{3.6c}$$

where

$$D_t(\cdot) = [\partial_t + \boldsymbol{u} \cdot \nabla](\cdot) \tag{3.7}$$

and $S(z)$ is the nondimensional stratification profile defined according to the relation $N^2(z^*) = N_0^2 S(z)$. We have defined $N_0 \equiv |g\rho_0^{*-1}(\partial_{z^*}\delta\hat{\rho}^*(z^*))_{max}|$ as the maximal buoyancy frequency and $S \equiv -\partial_z\delta\hat{\rho}$.

The nondimensional parameters that appear in (3.6) are determined a priori based on the energy injection rate ϵ_f^* and forcing length scale L_f^*. These parameters are the Rossby number Ro_f, Froude number Fr_f, Euler number Eu, and Reynolds number Re_f defined as

$$Ro_f = \frac{U_f^*}{2\Omega L_f^*}, \quad Fr_f = \frac{U_f^*}{N_0^* L_f^*}, \quad Eu_f = \frac{\delta p_0}{\rho_0 U_f^{*2}}, \quad Re_f = \frac{U_f^* L_f^*}{\nu} \equiv \left(\frac{\epsilon_f^* L_f^{*4}}{\nu^3}\right)^{1/3}. \tag{3.8}$$

The Rossby number is the ratio of rotation period, $T_\Omega^* = 1/2\Omega$, to the forcing time, $T_f^* = L_f^*/U_f^*$, and measures the rotational constraint of the fluid at the forcing scale. Hereafter, we focus solely on the rotationally constrained regime $Ro_f \ll 1$. The Froude number is the ratio of the Brunt-Väisälä time, $T_N^* = 1/N_0$, to T_f^* and measures the ratio of the slowest linear wave period to the nonlinear advective time scale. The Reynolds number provides a nondimensional measure of the energy injection rate into the system and therefore controls the degree of turbulence achieved at the forcing scale L_f^*. The Euler number measures the significance of the pressure gradient force relative

to inertial accelerations. The Prandtl number $\sigma = \nu/\kappa$ is the ratio of dissipation parameters and quantifies the thermometric properties of the working fluid.

In addition to the nondimensional forcing length scale $L_f = 1$ four internal length scales are also present: the dissipation (Kolmogorov) scale L_K, first Rossby radius of deformation L_D, the Zeman length scale L_Ω, and the Ozimodov length scale L_N. These *nondimensional* length scales are defined, respectively, as

$$L_K \equiv Re_f^{-3/4}, \qquad\qquad L_D \equiv \left(\frac{N_0 H^*}{2\Omega L_f^*}\right) = \frac{A Ro_f}{Fr_f}, \qquad (3.9)$$

$$L_\Omega \equiv \left(\frac{\epsilon_f^* L_f^{*-2}}{(2\Omega)^3}\right)^{1/2} = Ro_f^{3/2} \ll 1, \qquad L_N \equiv \left(\frac{\epsilon_f^* L_f^{*-2}}{N_0^3}\right)^{1/2} = Fr_f^{3/2}. \qquad (3.10)$$

The dissipation scale is the scale at which the nonlinear turnover time equals the time scale of viscous dissipation. The first Rossby radius of deformation is the scale where baroclinic instability converts potential to kinetic energy, and depends on H^*, the depth of the domain. The ratio $A = H^*/L_f^*$ is the nondimensional height of the domain. In quasigeostrophic dynamics the conversion of baroclinic to barotropic[1] energy occurs mainly at scales larger than L_D. Rotation influences the dynamics at scales larger than the Zeman scale, and the Ozimodov scale is that above which eddies are influenced by stratification.

In this investigation, we consider only the case $L_\Omega < L_K$ such that all fluid scales are influenced by rotation. This constraint places an upper bound for the Rossby number, namely

$$Ro_f = o\left(Re_f^{-1/2}\right). \qquad (3.11)$$

Given that the Rossby number is very small and the Euler number passively scales pressure, it becomes clear that there exist two primary control parameters Re_f, Fr_f. Varying these parameters causes the three dynamical length scales, L_D, L_N, and L_K to vary through seven distinct regimes shown in Figure 1.

---

[1] We adopt the convention that the 'barotropic' component of the system includes only the depth-independent part of the horizontal velocity; all other fields including vertical velocity and buoyancy are 'baroclinic.'
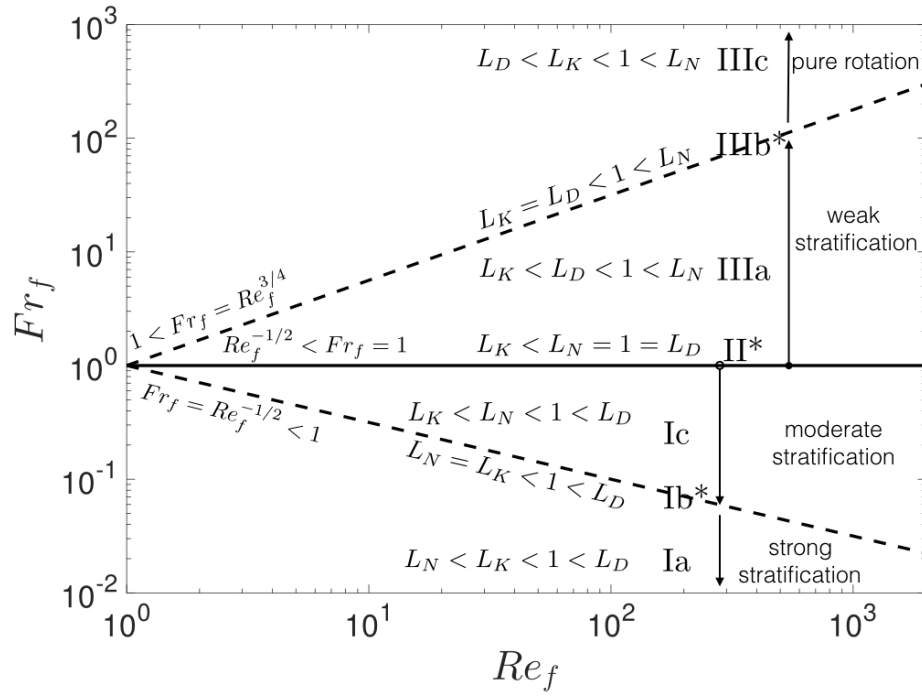
Figure 3.1: Distinguished Parameter Regimes from strong stratification (Ia) to weak stratification (IIIc). $*$ =boundary regimes.

3.2.1 Geostrophy and the Proudman-Taylor constraint

Motions under consideration occur on timescales much longer than the period of planetary rotation. Explicitly, we will be concerned with dynamics for which the Rossby number is a small parameter ε, i.e.,

$$\varepsilon \equiv Ro_f = \frac{U^*}{2\Omega L^*} = \frac{T_\Omega^*}{T_f^*} \ll 1. \tag{3.12}$$

For the Earth $2\Omega = \mathcal{O}(10^{-4})$ and motions observed to be affected by rotation in the atmosphere occur on $\mathcal{O}(10^3)$km horizontal scales while such dynamics in the ocean are observed to occur at relatively smaller $\mathcal{O}(10)$km horizontal scales. For this reason motions affected by Earth's rotation are referred to as "large-scale," however the notion of "large" is clearly not universal and length scales considered to be affected by system rotation depend on velocities characteristic of the dynamics we wish to describe. These examples place an emphasis on the manner in which Ro_f may be made small. Additionally, it is clear that 2Ω need not be extremely large in the context of discussions on "rapidly" rotating flows, however when flows are described as rapidly rotating what is meant is that $Ro_f \ll 1$.

When $Ro_f \ll 1$, the dominant force balance is geostrophy where the Coriolis force balances the pressure gradient force on $\mathcal{O}(L^*)$ length scales in equation (3.6), i.e.

$$\frac{1}{Ro}\hat{\boldsymbol{z}} \times \boldsymbol{u} \approx -Eu\nabla p, \tag{3.13}$$

where $Eu \sim Ro^{-1}$. Why this balances is to occur occur over others is made obvious by considering the other possible balances in equation (3.6) and their consequences. In making these considerations we remind ourselves of the types of flows we intend to study: rapidly rotating, stratified, and non-hydrostatic flows. A balance between the Coriolis term with relative accelerations leads us to conclude that $Ro_f \sim 1$, in contradiction to the rapidly rotating flows we have set out to study. When the Coriolis term balances the buoyancy term this leads to geostrophic and hydrostatic balance (involving fluctuating pressure and buoyancy fields), referred to as the thermal-wind balance, where buoyancy is large and stratification is strong, however our interests reside with non-hydrostatic flows such that $\Gamma = o(Ro_f^{-1})$ and $w = \mathcal{O}(1)$. If kinematic dissipation is to balance the Coriolis

acceleration then the Ekman number must be order-one. The scale L_ν^* on which such a balance might occur requires

$$1 \ll \frac{1}{Ro_f} = \frac{L^{*2}}{L_\nu^{*2}} \frac{1}{Re}, \tag{3.14}$$

where typical values of Re are large and leading us to conclude that $L_\nu^* \ll L^*$. Therefore, frictional effects can rise to balance Coriolis accelerations only on scales $o(L^*)$, for example, like those found near viscous boundaries. In addition, such viscous small-scales are well-separated from scales of motion that are geostrophically balanced. The remaining balance given by equation (3.13) is most reasonable for the flows of interest, in fact, such a balance is approximately observed for large-scale flow in Earth's atmosphere and oceans. However, it is important retain the notion of approximation when discussing this balance for large-scale motions since neglecting this notion leads to one unrealistic constraints on geostrophically balanced dynamics.

From equation (3.13) we may deduce constraints on the flow that inhibit vertical variations, however this is made clear upon taking the curl of equation (3.6) to arrive at the vorticity equation

$$D_t \boldsymbol{\omega} = \left(\boldsymbol{\omega} + \frac{1}{Ro_f} \hat{\boldsymbol{z}} \right) \cdot \nabla \boldsymbol{u} + \nabla \times b\hat{\boldsymbol{z}} + \frac{1}{Re} \nabla^2 \boldsymbol{\omega}. \tag{3.15}$$

where $\omega = \nabla \times \boldsymbol{u}$ (note that in the Boussinesq approximation the "baroclinic" or "solenoidal" term $\nabla p \times \nabla b$ in the vorticity equation is identically zero). For $Ro_f \ll 1$ the leading-order balance is vertically invariant and (from incompressibility) horizontally non-divergent, that is, to leading-order

$$\partial_z \boldsymbol{u} = 0, \qquad \nabla_\perp \cdot \boldsymbol{u}_\perp = 0, \tag{3.16}$$

and is consistent with the leading-order geostrophic balance given by equation (3.13) with *strict* equality. This is the so-called Taylor-Proudman constraint and it restricts motions to planes perpendicular to the axis of rotation resulting in motions that are *strictly* two-dimensional (Taylor, 1923; Proudman, 1916). However, these relations are not precise and are merely approximations. In writing these leading-order balances we have neglected terms which are *not* identically zero. For example, when considering the vorticity equation it is best to express the leading-order balance

and its consequence for incompressibility as

$$\partial_z \boldsymbol{u} = \mathcal{O}(Ro_f), \qquad \nabla_\perp \cdot \boldsymbol{u}_\perp = \mathcal{O}(Ro_f) \tag{3.17}$$

and stresses that the degree to which the Taylor-Proudman constraint is satisfied depends directly on the smallness of the Rossby number. For example, regions near viscous boundary layers where fluid motions must quickly and continuously adjust to satisfy boundary conditions have advective time scales that are much shorter than the rotation period (due to decreasing characteristic length), therefore Ro_f is no longer small and the Taylor-Proudman constraint (3.16) is broken/relaxed.

The preceding arguments should convince us that the *strict* requirement (3.16) on geostrophically balanced flows is wholly unrealistic. In fact, such constraints are not not observed geophysically realized. Small departures from this balance do occur and are referred to as quasi-geostrophy, and result in turbulent three-dimensional fluid motions. To allow three-dimensional motions when $Ro_f \ll 1$ and ultimately relax Taylor-Proudman constraints for flow well-separated from viscous boundary layers equation (3.17) suggest that vertical variations be allowed on large vertical scales H^* such that $H^*/L^* = \mathcal{O}(Ro_f^{-1})$. In summary, for weak buoyancy, associated with weak stratification, one expects the dynamics to be tall and thin (where $L^* = Ro_f H^*$), whereas for strong buoyancy and strong stratification one expects the dynamics to display an order-one aspect ratio $(L^* = Fr^{*-2}H^*)$. The equations used in our the numerical experiments (described in §3.3) are geostrophically-balanced, yet break the Proudman-Taylor constraint at small horizontal scales by allowing long vertical variations. The equations also allow the Proudman-Taylor constraint to be broken on unit-aspect-ratio scales in the presence of sufficiently strong stratification.

3.2.2   Eddy-wave dispersion relation at $Ro_f \ll 1$

A linear analysis of the unforced and inviscid form of equations (3.6), for normal modes $\propto \exp[i(\omega t + \boldsymbol{k}_\perp \cdot \boldsymbol{x}_\perp + k_z z)]$, provides the inertia-gravity dispersion relation for the wave frequency of oscillation ω and the horizontal and vertical wavenumbers $\boldsymbol{k}_\perp, k_z$:

$$\omega_{\text{wave}}^2 = \frac{1}{Fr_f^2}\sin^2\theta + \frac{1}{Ro_f^2}\cos^2\theta, \quad \omega_{\text{eddy}}^2 = 0. \tag{3.18}$$

Here $\theta = \tan^{-1}(k_\perp/k_z)$ denotes the angle made with the positive z-axis. The dispersion relation (3.18) implies the following bound on the wave frequencies

$$\omega_{\text{wave}} \geq \min\left(\frac{1}{Fr_f}, \frac{1}{Ro_f}\right). \tag{3.19}$$

It is particularly interesting to interpret the wave dispersion relation in the $Ro_f \ll 1$ limit as a function of stratification which, as established in the previous section, is tied to the spatial anisotropy of the flow. In the presence of strong stratification where $Fr_f \ll 1$, the wave dispersion relation implies $\omega_{\text{wave}} \gg \mathcal{O}(1)$ for all θ. Hence wave and eddy turnover timescales are asymptotically separated for all waves. This is the classical quasi-geostrophic limit where it is well-established that fast inertia-gravity waves may be filtered from the Boussinesq equations. This reduction leads to the hydrostatic QG equations describing the evolution of eddies on a slow manifold.

For weakly stratified flows characterized by $Fr_f = \mathcal{O}(1)$ there are fast waves and slow waves, depending on the anisotropy of the wave given by θ. The dispersion relation (3.18) clearly shows that waves with $\theta \sim \pm(\pi/2 - \mathcal{O}(Ro_f))$ retain order-one frequencies in the limit $Ro_f \ll 1$. Waves with angle $\theta \sim \pm(\pi/2 - \mathcal{O}(Ro_f))$ have $k_\perp/k_z \sim Ro_f^{-1}$, where vertical scales are longer than horizontal scales. It is now seen that these anisotropic inertia-gravity waves are not fast compared to the nonlinear eddy dynamics; since there is no gap between the time scale of waves and the time scale of eddies, the idea of a slow manifold absent of inertia-gravity waves is no longer applicable.

An approximate dispersion relation for these slow waves is obtained by inserting $k_\perp/k_z \sim Ro_f^{-1}$ into the dispersion relation (3.18) and eliminating small terms; the result is

$$\omega_{\text{wave}}^2 \sim \frac{1}{Fr_f^2} + \left(\frac{k_z}{k_\perp Ro_f}\right)^2, \quad \frac{k_z}{k_\perp} \sim Ro_f. \tag{3.20}$$

The phase and group velocities $\boldsymbol{v}_\text{p}$ and $\boldsymbol{v}_\text{g}$ associated with these slow waves are given by

$$\boldsymbol{v}_\text{p} \quad \sim \quad \frac{\omega_{\text{wave}}}{k_\perp^2}(k_x, k_y, k_z) = \mathcal{O}(1, 1, Ro_f), \tag{3.21a}$$

$$\boldsymbol{v}_\text{g} \quad \sim \quad \left(\frac{k_z}{k_\perp Ro_f}\right)^2 \frac{1}{k_\perp^2 \omega_{\text{wave}}}\left(-k_x, -k_y, \frac{k_\perp^2}{k_z}\right) = \mathcal{O}(1, 1, Ro_f^{-1}) \tag{3.21b}$$

with $\boldsymbol{v}_\text{p} \cdot \boldsymbol{v}_\text{g} = 0$ and $|\boldsymbol{v}_\text{g}| \gg |\boldsymbol{v}_\text{p}|$. Hence, inertia-gravity waves have phase and group velocities that are perpendicular: the slow waves propagate predominantly in horizontal directions whilst wave-

energy propagated by the group velocity is transmitted predominantly in the vertical direction (Greenspan, 1968). We note that velocity magnitudes are such that information is transmitted on the $\mathcal{O}(1)$ eddy-turnover time in all directions; this follows from the fact that information in the horizontal propagates over $\mathcal{O}(1)$ horizontal scales while information in the vertical propagates over $\mathcal{O}(Ro_f^{-1})$ vertical scales. The consequences of wave-eddy interactions without a time scale separation are still not fully understood, primarily because the main approach has been the use of DNS where efficiency and accuracy becomes increasingly prohibitive in the $Ro \ll 1$ limit. In the following, we analyze, and simulate reduced equations that describe the nonlinear interactions of vortical modes and slow inertia-gravity waves.

3.3   Reduced NonHydrostatic QG equations

A detailed asymptotic derivation of the reduced NH-QG equations is given in appendix B, however the following highlights the mosts paramount features. As mentioned above we treat the Rossby number as a small parameter $0 < \varepsilon \equiv Ro_f \ll 1$ and introduce the asymptotic series expansions for all dependent fluid variables

$$\boldsymbol{v} = (\boldsymbol{u}, p, b)^T = \varepsilon^{-1}\boldsymbol{v}_{-1} + \boldsymbol{v}_0 + \varepsilon\boldsymbol{v}_1 + \varepsilon^2\boldsymbol{v}_3 + \mathcal{O}(\varepsilon^3) \tag{3.22}$$

together with a multiple time scale expansion and a rescaled, anisotropic vertical coordinate

$$\partial_z \to \partial_z + \varepsilon\partial_Z, \qquad \partial_t \to \partial_t + \varepsilon^2\partial_T \tag{3.23}$$

into the Boussinesq equations. The large vertical scale is precisely the scale at which deviations from the Proudman-Taylor constraint are allowed. As argued above vertical variations on small vertical scales are constrained by Taylor-Proudman effects and one may simply set $\partial_z \equiv 0$, but above we retain the appearance of ∂_z as a didactic reminder of the multiple scales approach utilized. The slow dimensional time scale T^* is the period over which the vertical buoyancy flux acts to modify the mean buoyancy profile, and is such that the ratio of the order-one time scale T_f^* to the slow time scale T^* is given by $A_T = T_f^*/T^* = \varepsilon^2$. The derivation procedure results in a sequence of

equation balances that must be solved in succession, each balance associated with a power of ε. The multiple scales approach of (3.23) requires that fluid variables be decomposed into mean and fluctuating components, separating explicit dependence on small $\mathcal{O}(L^*)$ spatial scales and fast $\mathcal{O}(1)$ time scale from the large $\mathcal{O}(\varepsilon^{-1})$ vertical scale and the slow $\mathcal{O}(\varepsilon^{-2})$ time scale, i.e.,

$$\boldsymbol{v}(\boldsymbol{x}, Z, t, T) = \overline{\boldsymbol{v}}(Z, T) + \boldsymbol{v}'(\boldsymbol{x}, Z, t, T), \tag{3.24}$$

where overbars denote small scale and fast time averages such that

$$\overline{\boldsymbol{v}}(Z, T) \equiv \frac{1}{\tau V} \int_{\tau, V} f(\boldsymbol{x}, Z, t, T) \mathrm{d}\boldsymbol{x} \mathrm{d}t, \quad \overline{\boldsymbol{v}'} \equiv 0. \tag{3.25}$$

The non-dimensional parameters and their distinguished relations to ε are now determined as (Julien et al., 2006)

$$Fr_f = \mathcal{O}(1), \qquad Eu \sim \varepsilon^{-1}, \quad Re_f = \mathcal{O}(1). \tag{3.26}$$

The Reynolds number in particular has an upper bound value $Re_f = o(Ro_f^{-2})$ that indicates fluid motions may be driven from laminar through to turbulent motions. Importantly, Fr_f serves as a control parameter that may be varied from the strong stratification regime ($Fr_f \to 0$) through to the pure rotation regime ($Fr_f \gg 1$).

The asymptotic perturbation analysis given in appendix B reveals the simplification $\overline{\boldsymbol{u}}_{-1} = \boldsymbol{v}'_{-1} \equiv \boldsymbol{0}$ together with a leading order mean hydrostatic balance, i.e.,

$$\partial_Z \overline{p}_{-1} = \overline{b}_{-1}. \tag{3.27}$$

The leading order dynamics captured by the NH-QG equations are found to be in pointwise geostrophic balance satisfying

$$\hat{z} \times \boldsymbol{u}'_0 + \nabla p'_0 = 0, \tag{3.28a}$$

$$\nabla \cdot \boldsymbol{u}'_0 = 0. \tag{3.28b}$$

This yields, on defining $\nabla_\perp = (\partial_x, \partial_y, 0)$, the diagnostic solution

$$\boldsymbol{u}'_0 = -\nabla_\perp \times \psi'_0 \hat{z} + w'_0 \hat{z}, \qquad p'_0 = \psi'_0, \qquad \overline{\boldsymbol{u}}_0 = 0. \tag{3.29}$$

The reduced NH-QG equations describing the flow evolution are deduced at the next order by application of asymptotic solvability conditions and are given by (dropping primes)

$$\partial_t \zeta_0 + J[\psi_0, \zeta_0] - \partial_Z w_0 = \frac{1}{Re_f} \nabla_\perp^2 \zeta_0, \tag{3.30a}$$

$$\partial_t w_0 + J[\psi_0, w_0] + \partial_Z \psi_0 = b_0 + \frac{1}{Re_f} \nabla_\perp^2 w_0 + f_{w_0}, \tag{3.30b}$$

$$\partial_t b_0 + J[\psi_0, b_0] + w_0 \left(\partial_Z \bar{b}_{-1} + \frac{1}{Fr_f^2} S(Z) \right) = \frac{1}{\sigma Re_f} \nabla_\perp^2 b_0, \tag{3.30c}$$

$$\partial_T \bar{b}_{-1} + \partial_Z \left(\overline{w_0 b_0} \right) = \frac{1}{\sigma Re_f} \partial_Z^2 \bar{b}_{-1}. \tag{3.30d}$$

This equation set gives the coupled evolution of vertical vorticity $\zeta_0 = \nabla_\perp^2 \psi_0$, vertical velocity w_0, and buoyancy $\bar{b}_{-1} + \varepsilon b_0$ (decomposed into its mean and fluctuating components). Note that Eu and Γ no longer appear, having been absorbed by a rescaling of the pressure ($p \to p/Eu$) and buoyancy ($b \to b/\Gamma$).

The NH-QG equations bear the enduring characteristics of quasi-geostrophic theory, specifically: leading-order pressure plays the role of the geostrophic streamfunction ($p_0' = \psi_0$); planetary rotation is solely responsible for axial vortex stretching ($\partial_Z w_0$ in equation (3.30a)); material advection occurs only in the horizontal direction with $\boldsymbol{u}_{0\perp} \cdot \nabla_\perp \equiv J[\psi_0, \cdot] = \partial_x \psi_0 \partial_y - \partial_y \psi_0 \partial_x$, vertical advection is a subdominant phenomenon with $w_0 \partial_Z \boldsymbol{v}_0 = \mathcal{O}(\varepsilon)$, where $\boldsymbol{v}_0 = (\boldsymbol{u}_0, p_0 = \psi_0, b_0)^T$.

In the presence of weak stratification, that is, when $Fr_f \sim 1$ vertical motions are now significant and result in the appearance of inertial acceleration terms in vertical momentum equation (3.30b). Notably, linearization about a constant stable stratification profile $S(Z) = -\partial_z \hat{\rho} = 1$ in the inviscid limit $Re \to \infty$ captures the dispersion relation for slow inertial-gravity waves and vortical eddies, both evolving on the order-one advective time scale. Therefore, the NH-QG equations for rapidly rotating ($Ro_f \ll 1$) and weakly stratified ($Fr_f \sim 1$) flow describe a regime in which inertial-gravity waves and eddies (evolving on similar time scales) interact nonlinearly.

3.3.1 Energetics and conserved quantities

Like the Boussinesq equations, the inviscid and unforced NH-QG equations conserve several positive quadratic functionals. The time-rate-of-change of horizontal kinetic (HKE), vertical kinetic energy (VKE) and potential energy (PE) are given[2] , respectively, by

$$\partial_t \text{HKE} \quad := \quad \partial_t \left[\frac{1}{2} \left(\langle \overline{|\nabla_\perp \psi_0|^2}^{\mathcal{A}} \rangle \right) \right] = \langle \overline{w_0 \partial_Z \psi_0}^{\mathcal{A}} \rangle, \tag{3.31a}$$

$$\partial_t \text{VKE} \quad := \quad \partial_t \left[\frac{1}{2} \langle \overline{w_0^2}^{\mathcal{A}} \rangle \right] = -\langle \overline{w_0 \partial_Z \psi_0}^{\mathcal{A}} \rangle + \langle \overline{w_0 b_0}^{\mathcal{A}} \rangle, \tag{3.31b}$$

$$\partial_t \text{PE} \quad := \quad \partial_t \left[\frac{1}{2} \left\langle \frac{\overline{b_0^2}^{\mathcal{A}}}{\left(\partial_Z \overline{b}_{-1}(Z) + Fr_f^{-2} S(Z) \right)} \right\rangle \right] = -\langle \overline{w_0 b_0}^{\mathcal{A}} \rangle, \tag{3.31c}$$

where $\langle \cdot \rangle$ and $\overline{\cdot}^{\mathcal{A}}$ denote vertical and horizontal averages, respectively, and the time-invariance of total energy $E = KE + PE = \text{HKE} + \text{VKE} + \text{PE}$ is clear. The equations also conserve a total buoyancy variance

$$\partial_t \overline{\langle (b_0^2 + (\overline{b}_{-1} + \Sigma(Z))^2}^{\mathcal{A}} \rangle = 0, \quad S(Z) := \partial_Z \Sigma(Z) = -Fr_f^{-2} \partial_Z \delta \hat{\rho}. \tag{3.32}$$

Finally, the NH-QG equations materially conserve a form of potential vorticity (PV)

$$\partial_t q + J[\psi_0, q] = 0, \tag{3.33a}$$

$$q = \zeta_0 + (\boldsymbol{\omega}_\perp \cdot \nabla_\perp + \partial_Z) \left(\frac{b_0}{(\partial_Z \overline{b}_{-1} + Fr_f^{-2} S(Z))} \right). \tag{3.33b}$$

Notably, it can be seen the potential vorticity q can be partitioned into a linear and nonlinear component dependent on vortical and vertical motions respectively.

3.3.2 Barotropic, baroclinic decompostion

Rapid rotation often induces a transfer of energy to the depth-independent component of horizontal velocity (Smith and Waleffe, 1999). It is useful therefore to examine pathways by which energy is converted to the depth-independent horizontal velocity with the remainder of the system. In quasigeostrophic theory, the velocity is often expanded as a sum over a basis of vertical modes,

---

[2] 'Potential energy' here is not an approximation to the gravitational potential energy $-g \langle \overline{\rho z}^{\mathcal{A}} \rangle$, but the terminology is conventional.

the first of which is depth-independent and is conventionally called the 'barotropic' mode (Rocha et al., 2016). More generally, the definition of a barotropic fluid is a fluid for which density is a function of pressure alone. A constant-density fluid is an example of a barotropic fluid, but a constant-density fluid need not be depth-independent – an apparent conflict with the conventional quasigeostrophic usage of the term.

To fix a particular usage of the terms 'baroclinic' and 'barotropic' in the context of a stratified Boussinesq fluid we take the following line of reasoning. In a Boussinesq fluid the deviation from the constant reference density is $-b^* \rho_0^*/g$, which is not generally a function of pressure alone unless $b^* = 0$. Because vertical velocity in the presence of a backckground stratification induces buoyancy perturbations, w is intimately associated with baroclinicity and we choose to consider it as part of the 'baroclinic' component of the dynamics. The barotropic component, having both $b_0 = 0$ and $w_0 = 0$, must also have no vertical pressure gradient $\partial_Z \psi_0 = 0$. This line of reasoning leaves the depth-independent part of the horizontal velocity as the only element of the barotropic component, with the baroclinic component comprising w_0, b_0, and the depth-dependent part of ψ_0. Our use of the terms is distinguished from an alternate use where 'barotropic' simply indicates the depth-independent component and includes both $\langle w_0 \rangle$ and $\langle b_0 \rangle$.

We thus arrive at the barotropic-baroclinic (bt-bc) decomposition

$$\boldsymbol{u}_{0,bt} = -\nabla_\perp \times \langle \psi_0 \rangle \hat{\boldsymbol{z}}, \qquad b_{0,bt} = 0, \tag{3.34}$$

$$\boldsymbol{u}_{0,bc} = -\nabla_\perp \times \psi_0' \hat{\boldsymbol{z}} + w_0 \hat{\boldsymbol{z}}, \qquad b_{0,bc} = b_0$$

where $\psi_0 = \langle \psi_0 \rangle + \psi_0'$. Partitioning the NH-QG equations thus reduces to decomposing the vorticity equation (3.30a), into its barotopic and baroclinic components. Namely

$$\partial_t \langle \zeta_0 \rangle + J[\langle \psi_0 \rangle, \langle \zeta_0 \rangle] = -\langle J[\psi_0', \zeta_0'] \rangle + \frac{1}{Re_f} \nabla_\perp^2 \langle \zeta_0 \rangle, \tag{3.35a}$$

$$\partial_t \zeta_0' + J[\langle \psi_0 \rangle + \psi_0', \zeta_0'] - \langle J[\psi_0', \zeta_0'] \rangle + J[\psi_0', \langle \zeta_0 \rangle] - \partial_Z w_0' = \frac{1}{Re_f} \nabla_\perp^2 \zeta_0'. \tag{3.35b}$$

Equation (3.35a) is the two-dimensional barotropic vorticity equation. Within the barotropic subspace kinetic energy $\overline{|\nabla_\perp \langle \psi_0 \rangle|^2}^{\mathcal{A}}$ and enstrophy $\overline{\langle \zeta_0 \rangle^2}^{\mathcal{A}}$ are conserved quantities in the absence

of dissipation and forcing. Forcing of barotropic vorticity occurs through nonlinear interactions between purely baroclinic fields in the form of advection of baroclinic vorticity by baroclinic horizontal velocities, i.e., $\langle J[\psi_0', \zeta_0'] \rangle = \langle \boldsymbol{u}_{0\perp}' \cdot \nabla \zeta_0' \rangle$. Therefore, this term acts as a source when $\boldsymbol{u}_{0\perp}'$ and $\nabla \zeta_0'$ are barotropically collinear.

Some comments are appropriate on the distinguishing features of the NH-QG equations in comparison with a recent and alternative formulation by Wingate et al. (2011). In Wingate et al. (2011) the asymptotic development is based strictly on a multiple-scales approach in time only with an isotropic scaling of the spatial coordinates. The resulting slow manifold is found to be one that strictly enforces the Proudman-Taylor constraint of the velocity field, i.e., $\partial_Z \boldsymbol{u}_0 = 0$. Consequently, the term coupling baroclinic and barotropic dynamics $\langle J[\psi_0', \zeta_0'] \rangle$ is predicted to be asymptotically small, therefore decoupling barotropic vorticity dynamics from the now Taylorized depth-independent baroclinic dynamics of $\langle w_0 \rangle$ and $\langle b_0 \rangle$. Stochastically forcing baroclinic dynamics therefore cannot influence barotropic motions (Whitehead and Wingate, 2014). We contend that the NH-QG equations demonstrate that slow inertial-gravity waves and baroclinic eddies are a vital leading-order component of the dynamics at low Rossby and moderate Froude numbers.

3.4 Numerical simulation for stably stratified NH-QG equations

Since the layer of stably stratified fluid is void of a natural instability capable of inducing fluid motion, artificial forcing is required. Previous studies have accomplished the task of forcing a stable layer through the controlled injection of motion inducing energy (Smith and Waleffe, 2002; Lindborg, 2006; Wingate et al., 2011). The present study induces fluid motions in a fashion similar to these past investigations. In particular, we perform numerical simulations where motion is induced by a controlled injection of *vertical* kinetic energy. By forcing the vertical momentum equation only this study differs from those in which all three components of momentum are forced (e.g. Sen et al., 2012; Marino et al., 2013). The forcing of vertical momentum has the desirable consequence that the energy injected manifests only as wave energy energy, i.e., only wave modes are directly excited. This is made clear by inspecting the amplitudes for the vortical and wave

Regime	$Fr_f(Re_f)$	$Fr_f(Re_f = 50)$	$Fr_f(Re_f = 100)$	$Fr_f(Re_f = 300)$
Ia	$\frac{1}{2}Re^{-1/2}$	0.0707	0.0500	0.0289
Ib*	$Re^{-1/2}$	0.1414	0.1000	0.0577
Ic	$\frac{1}{2}(1 + Re^{-1/2})$	0.5707	0.5500	0.5289
II*	1	1	1	1
IIIa	$\frac{1}{2}(1 + Re^{3/4})$	9.9015	16.311	36.542
IIIb*	$Re^{3/4}$	18.803	31.623	72.084
IIIc	$2Re^{3/4}$	37.606	63.246	144.17
Grid resolution	$N_x \times N_y \times N_z$	$96 \times 96 \times 96$	$192 \times 192 \times 192$	$384 \times 384 \times 384$

Table 3.1: Values of Fr_f as a function of Re_f used in simulations of the NH-QG equations based on the seven regimes identified in figure 3.1. Domain size for each simulation is $10L_f \times 10L_f \times 1$, where $L_f = 1$ is the imposed forcing length scale. To ensure sufficient resolution we use the convention that $\Delta x = 2L_K$, where $L_K = Re^{-3/4}$ is the dissipation length scale, giving the number of Fourier modes used in each Cartesian direction as $N_{x,y,z} = L_b Re^{3/4}/2$. The Prandtl number is fixed at $\sigma = 7$ for all simulations.

eigenmodes $C_{\boldsymbol{k}}^0$ and $C_{\boldsymbol{k}}^{\pm}$, respectively,

$$C_{\boldsymbol{k}}^0 = \frac{Fr_f^{-1}k_{\perp}\hat{\zeta}_{\boldsymbol{k}} + ik_Z k_{\perp} Fr_f \hat{b}_{\boldsymbol{k}}}{\omega_{\boldsymbol{k}} k_{\perp}}, \tag{3.36a}$$

$$C_{\boldsymbol{k}}^{\pm} = \frac{-ik_{\perp}^2 \omega_{\boldsymbol{k}} \hat{w}_{\boldsymbol{k}} \mp ik_Z \hat{\zeta}_{\boldsymbol{k}} \mp k_{\perp}^2 \hat{b}_{\boldsymbol{k}}}{2^{1/2}\omega_{\boldsymbol{k}} k_{\perp}}. \tag{3.36b}$$

It is clear that forcing any component of horizontal velocity or buoyancy directly induces vortical energy, yielding nonzero values for $C_{\boldsymbol{k}}^0$. Therefore, if system energy is injected through vertical kinetic energy by forcing the vertical momentum equation to induce non-zero values of $\hat{w}_{\boldsymbol{k}}$ (and therefore non-zero values of $C_{\boldsymbol{k}}^{\pm}$), then energy transfer to the vortical modes $C_{\boldsymbol{k}}^0$ must occur through nonlinear interactions among these linear eigenmodes that act to transfer wave energy to vortical energy. Why we desire vortical energy to originate from non-artificial means (i.e., nonlinear interactions) is due to an interest in the natural process for the formation of large-scale coherent vortices. Allowing such coherent structures to arise naturally allows for (in some sense) an uncontaminated study of the inverse cascade.

The energy source occurs through the vertical momentum equation (3.30b) through the physical-space forcing function f_{w_0}. The following describes the method for building the forcing function at each time-step in the numerical simulation of the NH-QG equations. An array holding the discretized from of the forcing function is seeded pointwise in physical-space with independent and identically distributed (i.i.d) spatial noise. For simulations performed here Gaussian distributions are used and we employ the methods by Marsaglia and Tsang (2000) to generate samples drawn from a normal distribution with zero mean and unit variance (these samples are assigned to each grid point in the numerical domain). The discretized forcing function holding the pointwise i.i.d. spatial noise is then Fourier transformed and then "shaped," or spatially-correlated, such that the forcing function f_{w_0} has a spherically symmetric spectrum given by

$$E_{f_{w_0}}(\boldsymbol{k}) = C\epsilon_f \exp\left(-\frac{1}{2}(|\boldsymbol{k}| - k_f)^2\right). \tag{3.37}$$

This is implemented by performing the Fourier-space pointwise product of the forcing function f_{w_0}

(holding the i.i.d Gaussian noise in Fourier-space) with

$$\sqrt{C\epsilon_f \exp\left(-\frac{1}{2}(|\boldsymbol{k}| - k_f)^2\right)}, \tag{3.38}$$

where ϵ_f is the flux of vertical kinetic energy into the system, k_f is the prescribed forcing wavenumber and the constant C is determined such that averaged energy injection is ϵ_f. This implementation ensure that the *vertical kinetic energy* is centered about k_f. For this study we set $k_f = 2\pi$ (setting the nondimensional horizontal length scale to $L_f = 1$) and $\epsilon_f = 1$ and we normalize the spectrum of the forcing function so that volume averaged energy flux becomes

$$\int_0^{2\pi} \int_0^{\pi} \int_0^{\infty} E_{f_{w_0}}^2(k)k^2 \sin\phi\, dk\, d\phi\, d\theta = 1. \tag{3.39}$$

The choice of L_f is important given the interest in studying the upscale energy transfer through inverse cascade. To this end, the choice for a forcing scale requires our box-scale to be significantly large (relative to the forcing scale) so as to allow room for the growth of large-scale fluid structures. Forcing at larger scales or the box-scale would directly influence the largest scales, not allowing for a natural inverse cascade through energy transfer via nonlinear interactions.

Numerical simulations of the NH-QG equations are performed in a triply-periodic box and solutions are expanded in Fourier series. Such an idealization is standard and simplifies the analysis. We note that the Fourier expansion employed here is distinct from the use of Chebyshev discretization in vertical as in §2 for the study of rapidly rotating Rayleigh-Bénard convection. The numerical box has dimensional size $L_b L_f Ro_f H^* \times L_b L_f Ro_f H^* \times H^*$, where $L_f = 1$ is the nondimensional forcing length scale and L_b is the nondimensional length of the horizontal domain, thus, the nondimensional domain size is $L_b \times L_b \times 1$ and we set $L_b = 10$. The numerical time-stepping scheme used is an implicit/explicit formally second-order Runge-Kutta scheme derived by Spalart et al. (1991a) and previously used by Sprague et al. (2006) for numerical simulation of the NH-QG equations for the rapidly rotating Rayleigh-Bénard problem.

While the spatially-correlated and normalized forcing function f_{w_0} is a smooth physical-space function it is, however *everywhere* discontinuous in time. That is, following the procedure

outlined above at each time-step gives f_{w_0} in Fourier-space (call this Fourier-space variable χ) as a stochastic process. In particular, the variable f_{w_0} satisfies the definition for a standard Wiener process (Higham, 2001). The consequence for such a variable is that it cannot be treated with standard numerical methods for time-stepping solutions to deterministic differential equations that assume some degree of temporal smoothness/differentiability. The stochastic dynamics in this investigation are treated with a simple splitting method where the deterministic dynamics are treated independently of the stochastic forcing. After completing a full time step of the deterministic dynamics a random forcing increment $\sqrt{dt}\chi$ is added to the deterministic solution for w_0 (or, in some initial tests, to b_0), effectively using the Euler-Maruyama method

$$w_0^{*n+1} = w_0^n + \sqrt{dt}\chi \tag{3.40}$$

for the stochastic forcing term $f_{w_0}(t)$ (Higham, 2001). In addition to respecting the stochastic nature of the dynamics, this approach has the desirable property that the mean rate of energy injection is independent of the system state, and is controlled a priori.

Fourier expansions are dealiased using the standard 2/3s rule. To ensure sufficient resolution we use the convention that $\Delta x = 2L_K$, where $L_K = Re^{-3/4}$ is the dissipation length scale for statistically steady flow. Use of this convention gives the number of Fourier modes used in each Cartesian direction as $N_{x,y,z} = L_b Re^{3/4}/2$. Resolutions used in our numerical simulations are given in table 3.1. The simulation parameters (Re_f, Fr_f, σ) are selected based on the regimes identified in figure 3.1. For a given Re_f we vary Fr_f so as to explore each of the seven regimes identified in figure 3.1. This process of selecting Fr_f is outlined in table 3.1. All simulations are computed with $\sigma = 7$.

In addition to forcing vertical velocity we have also performed numerical simulations with buoyancy forcing as in Whitehead and Wingate (2014), however, since the momentum equations decouple from the buoyancy equations for large Fr_f the injection of potential energy becomes unphysical. For this reason we only present results associated with the injection of vertical kinetic energy via the vertical velocity equation (3.30b).

Numerical simulations are accomplished through the use of Fortran code written in large part by Keith Julien, Edgar Knobloch and Joe Werne. For the parameters outlined in table 3.1 simulations are run on parallelized code using 16, 32, and 64 cores. The Janus supercomputer at the University of Colorado Boulder was used where compute nodes contain two hex-core 2.8Ghz Intel Westmere processors for 12 cores per node. These simulations were run with 96^3, 192^3 and 384^3 grid points, respectively. Run times vary from just a few hours for the smallest simulations with 96^3 grid points split among 16 processors to several days for the largest simulations with 384^3 grid points split among 64 processors. The method of parallelizing these simulations made use of MPI and was achieved by partitioning physical space grid points into horizontal blocks grouped into layers containing $N_{z_p} = N_z/ncpu$ vertical grid points (where $ncpu$ is the number of processors used). Blocks in Fourier-space are organized similarly, however, layers are split along the $\hat{x}$-direction for purposes of time-efficient communication.

3.5   Results

The nondimensional parameters defined in section 3.2 are based on a priori characteristic scales built from the energy injection rate ϵ_f and injection scale L_f. These scales are not necessarily the same as the scales that truly characterize the flow; certainly it is not the case that the large-scale flows observed here occur on the forcing scale $L_f = 1$. For this reason we give a summary of a posteriori nondimensional parameters that define the flows simulated. To do this we compute the centroid of energy spectra to get a characteristic wavenumber k_c and associated length scale L_c; we compute a characteristic velocity U_c from the volume-averaged horizontal kinetic energy (HKE), that is,

$$k_c = \frac{\int kE(k)dk}{\int E(k)dk}, \quad U_c = (2HKE)^{1/2}, \tag{3.41}$$

where $E(k)$, for example, are the curves in figure 3.9. These nondimensional measured values are then used to define a posteriori Reynolds and Froude numbers

$$Re_c = \frac{U_c^* L_c^*}{\nu} = \frac{U_f^* U_c L_f^* L_c}{\nu} = Re_f U_c L_c, \quad Fr_c = \frac{U_c^*}{N_0^* L_c^*} = \frac{U_f^* U_c}{N_0^* L_f^* L_c} = Fr_f \frac{U_c}{L_c} \tag{3.42}$$

A posteriori Fr_c and Re_c for a range of are parameters are summarized in table 3.2. Generally, characteristic horizontal scales are larger than L_f, and characteristic velocities are larger than U_f. This results in Reynolds numbers that are larger than Re_f. The larger measured horizontal scale L_c outweighs the increase in U_c, leading to Froude numbers that are smaller, in some cases by an order(s)-of-magnitude, than Fr_f, however, what was considered weakly stratified as measured by Fr_f remains so as measured by Fr_c.

Performing DNS of the NH-QG equations (with the nondimensional parameters outlined in table 3.1) two qualitatively identifiable regimes are observed, corresponding to strong and weak stratification: $Fr_f < 1$ and $Fr_f \geq 1$ respectively. The regime diagram in figure 3.2 partitions (Re_f, Fr_f)-space into two regimes based on volume renders of vertical vorticity. In both regimes the flow organizes into a large-scale, barotropic dipole with some additional small-scale turbulence. Figures 3.3 and 3.4 gives renders for vertical vorticity, buoyancy and vertical velocity for strong and weak stratifications when $Re_f = 300$.

The strong stratification regime ($Fr_f < 1$, figure 3.3) is distinguished by a tendency of the flow to form well-defined and sustained layers where small-scale turbulence is active and the local stratification is reduced. Layering is observed for $Re_f = 100$ and $Re_f = 300$, but not for $Re_f = 50$. We conclude that the instability responsible for layering is inhibited by viscous effects at lower Re_f. We note that layering, as observed in figure 3.3 is not observed for classical QG dynamics where energy rapidly transfers to large vertical scales (Smith and Vallis, 2001, 2002). In the second regime of weak stratification ($Fr_f \geq 1$, figure 3.4) the columnar structures are unobstructed by layers, and evolve in a sea of small-scale turbulence.

In both regimes the energy accumulates primarily in the barotropic mode and at large horizontal scales, indicating a robust inverse cascade of energy. At lower Reynolds numbers $Re_f \leq 100$ (Re_c up to ≈ 2000) the total energy in the system reaches a statistical equilibrium. In addition to
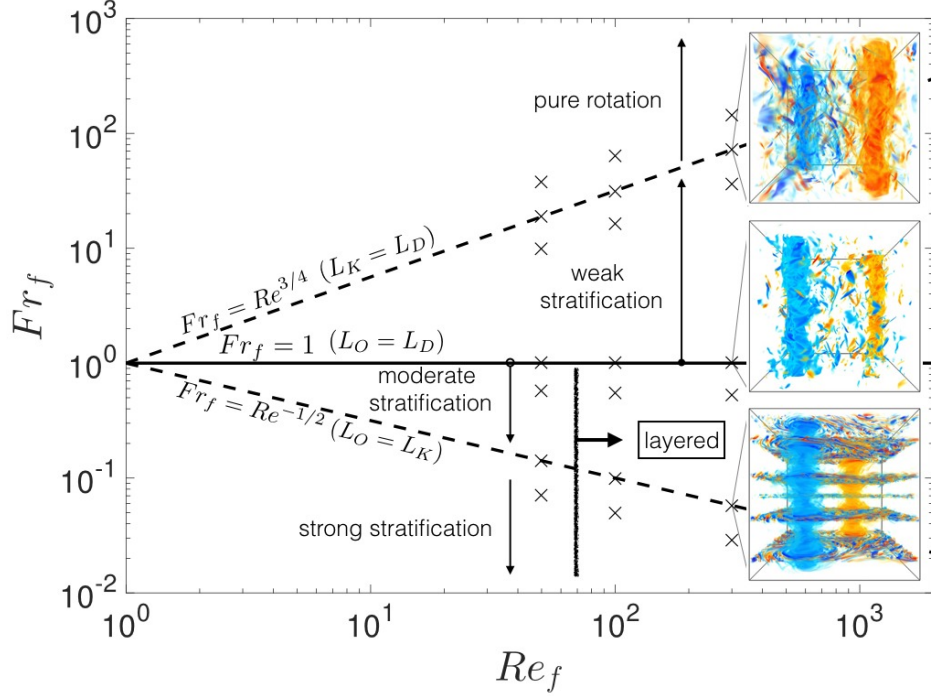
Figure 3.2: A qualitative partitioning of (Re_f, Fr_f)-space using volume renders of vorticity. Values of (Re_f, Fr_f) for which simulations were performed are denoted by an $\times$ (see Table 3.1). The flow is characterized by layering, barotropization and an inverse cascade. For $Fr_f < 1$ the flow organizes into well-defined layers (except at low-Re_f, e.g., $Re_f = 50$) and when $Fr_f \geq 1$ layering is absent. We emphasize the presence of a dominant barotropic component of energy and a clear inverse cascade for all Fr_f simulated. Similar flow characteristics are observed for buoyancy and vertical velocity (see Figures 3.3 and 3.4).

	$Fr_f =$	$Re_f^{-1/2}$				$Re_f^{3/4}$			
	subspace	L_c	U_c	Re_c	Fr_c	L_c	U_c	Re_c	Fr_c
	$BT + BC$	6.0	0.5	1.4×10^2	0.0115	7.1	1.7	5.9×10^2	4.5
$Re_f = 50$	BT	8.4	0.7	3.0×10^2	0.0122	8.6	2.5	1.0×10^3	5.3
	BC	3.3	0.2	33	0.0088	2.5	0.3	40	2.3
	$BT + BC$	7.0	1.4	9.6×10^2	0.0199	7.3	3.0	2.0×10^3	12.1
$Re_f = 100$	BT	8.4	2.0	1.6×10^3	0.0228	8.4	3.5	2.0×10^3	13.4
	BC	2.0	0.1	29	0.0077	2.2	0.3	66	4.3
	$BT + BC$	6.5	2.2	4.4×10^3	0.0199	6.6	2.9	5.7×10^3	31.3
$Re_f = 300$	BT	7.7	2.8	6.5×10^3	0.0209	8.0	4.0	9.6×10^3	35.8
	BC	2.2	0.2	1.5×10^2	0.0056	1.6	0.3	1.4×10^2	12.4

Table 3.2: Characteristic scales U_c and L_c computed from centroids of energy spectra and nondimensional quantities Re_c and Fr_c based on the measured values L_c and U_c. Scales that most closely resemble L_f are baroclinic, while L_c in the barotropic subspace are significantly larger and resemble the box-scale.

(a) Vertical vorticity, ζ (b) Buoyancy, b (c) Vertical velocity, w
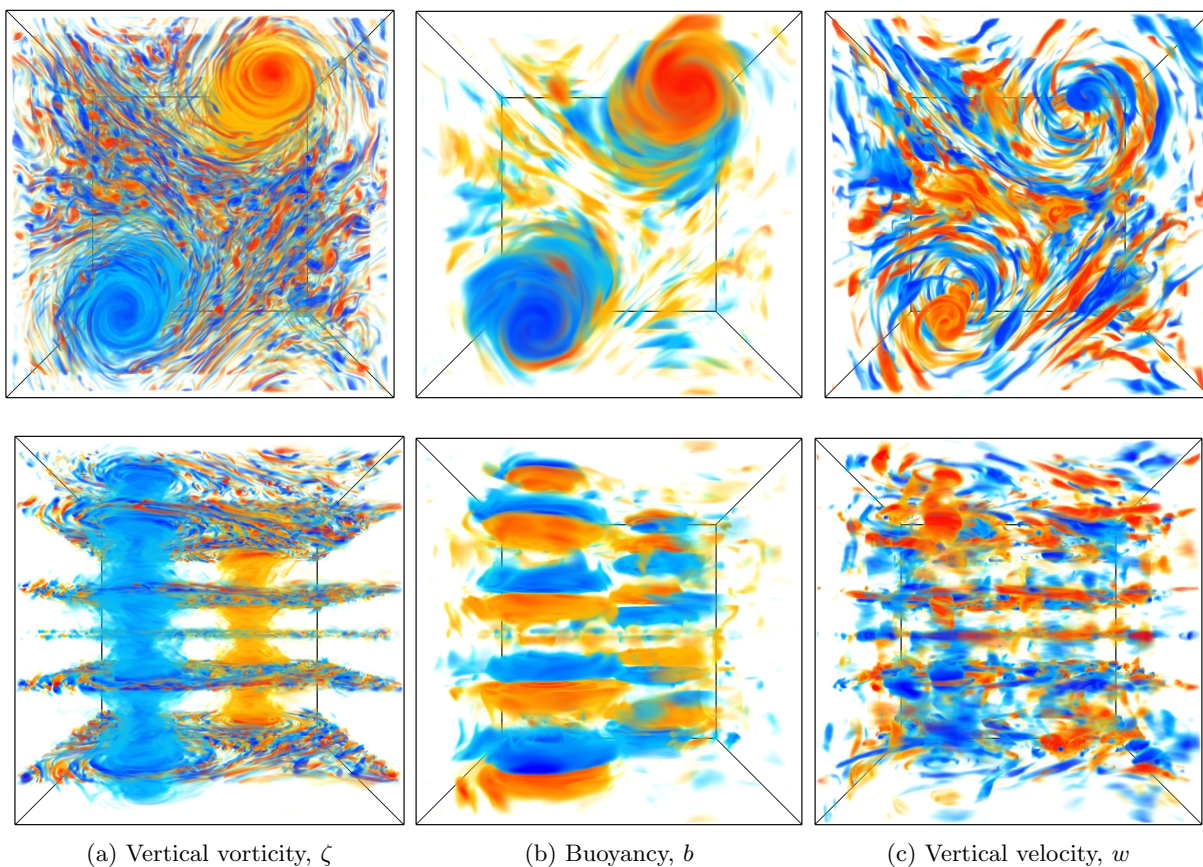
Figure 3.3: Volume renders of vertical vorticity ζ (left column), buoyancy b (middle column), and vertical velocity w (right column) for the case of strong stratification $Re_f = 300$, $Fr_f = Re_f^{-1/2}$. Top row (top view), bottom row (side view).

(a) Vertical vorticity, ζ (b) Buoyancy, b (c) Vertical velocity, w
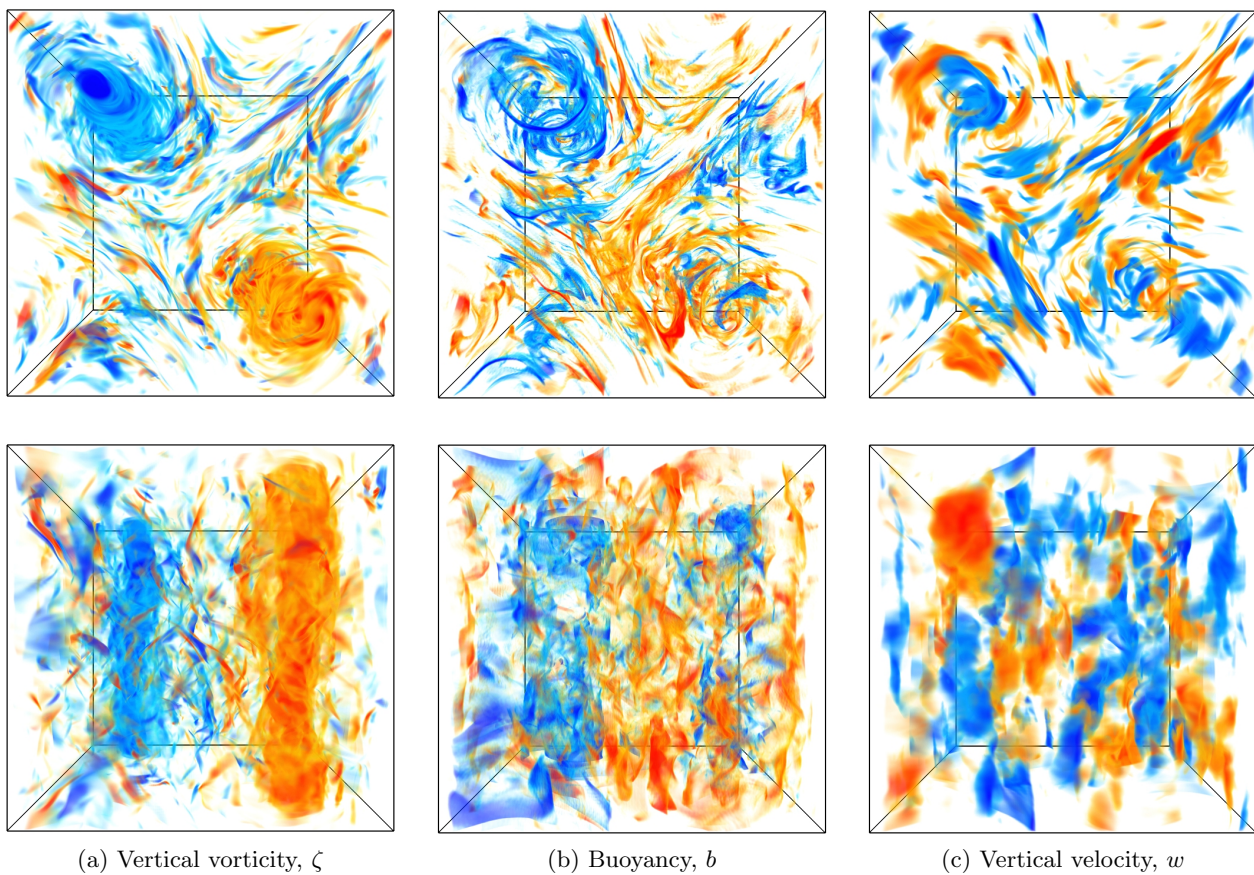
Figure 3.4: Volume renders of vertical vorticity ζ (left column), buoyancy b (middle column), and vertical velocity w (right column) for the case of weak stratification $Re_f = 300$, $Fr_f = Re_f^{3/4}$. Top row (top view), bottom row (side view).

the inverse energy transfer, we diagnose a robust *direct* transfer of kinetic energy in the barotropic mode, which allows the small amount of energy injected by the baroclinic motions to be balanced by small-scale dissipation, leading to energy saturation. At higher Reynolds numbers, $Re_f = 300$ (Re_c greater than ≈ 4000), the total energy shows no sign of saturation. These results are presented in more detail in the following subsections.

We note that these results do not necessarily represent universal properties of rotationally constrained stratified flow in every respect. Undoubtedly, the dynamic behavior depends significantly on the method by which external energy is injected to excite motion. As mentioned above, the forcing method employed here excites vertical motion, therefore, only excites wave modes and does not directly force the vortical mode. This approach to forcing aims to better understand the energetic pathway from three-dimensional baroclinic motions to two-dimensional barotropic motions.

3.5.1   Layering

Layering is observed in all fields though most distinct in the renders of vertical vorticity shown in figure 3.3. To clarify terminology, we define layers to be the localized planar regions home to small-scale turbulence and occurring for $Fr_f < 1$. Figure 3.5 shows the effect of strong stratification on the time-averaged vertical gradient of the total mean buoyancy profile and on the structure of $\zeta_{0,RMS}$ for simulations with $Re_f = 100$ and $Fr_f \leq 1$. Reduction of stratification within the layers is presumably associated with local turbulent mixing within the layers.

Some basic characteristics of the location and height of layers are given by the mean buoyancy gradient and vertical profiles of $\zeta_{0,RMS}$. The more informative of the two is the set of RMS profiles of vertical vorticity. The center locations for layers coincide with the location of local minima within the peaks for $\zeta_{0,RMS}$ and are obvious for $Fr_f = 0.05$ and $Fr_f = 0.1$. The neighboring local maxima may be used to give a reasonable metric for layer height and indicate the presence of top and bottom sublayers that make up an entire layer. As Froude number is increased layer height is observed to increase. This effect is illustrated in figure 3.5 as Fr_f is increased from 0.05 to 0.55. When
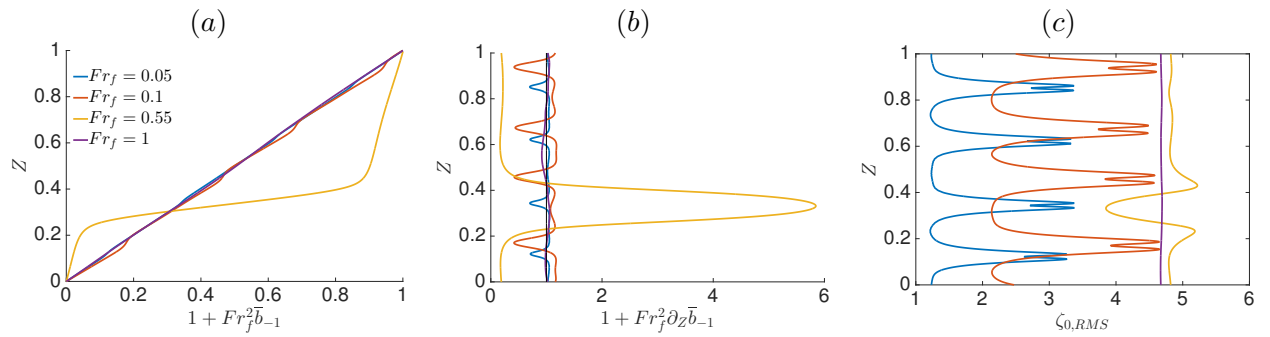
Figure 3.5: Time averaged vertical profiles for $Re_f = 100$. Profiles of (a) total mean buoyancy, (b) vertical gradient of mean buoyancy and (c) RMS vertical vorticity. Layering occurs in horizontal planes where mean stratification is locally minimized. The effect on the stratification profile is due to the nature of vertical buoyancy flux, similarly, layered structuring seen for vertical vorticity is due vortex stretching. Layer locations coincide with locations of sharp local minima within the peaks of $\zeta_{0,RMS}$. Layer height may be given by the distance between local maxima surrounding the singular local minima and indicate the presence of sublayers (jets). The vertical extent of layers and their sublayers is observed to increase with decreased stratification. Similar structuring is observed for vertical velocity, buoyancy, and dissipation.

$Fr_f = 0.55$ there is only one large layer of reduced stratification and increased turbulence, and one smaller less-turbulent region of increased stratification that occupies approximately $Z \in [0.2, 0.4]$.

Finally, we note that the instantaneous dissipation rate for energy is increased within the layers. The instantaneous dissipation rate for horizontal kinetic energy is $Re_f^{-1}\overline{\zeta^2}^{\mathcal{A}}$, and figure 3.5($c$) clearly shows that this is increased within the layers. The dissipation rates for vertical kinetic energy and buoyancy variance are also locally increased within the layers (not shown). The dynamics leading to the formation of the layers is as yet unknown.

3.5.2   Timeseries, equilibration and average energy conversions

We find that total energy is largely dominated by horizontal kinetic energy and this becomes increasingly true as stratification weakens and the system approaches purely rotating dynamics. For this reason we focus primarily on the horizontal kinetic energy, hereafter HKE. Figure 3.6 shows timeseries of volume averaged HKE for strong stratification ($Fr_f = Re_f^{-1/2}$, top row) and weak stratification ($Fr_f = Re_f^{3/4}$, bottom row) at $Re_f = 50$, 100, and 300; the panels correspond to places where dashed lines in figure 3.2 intersect with an $\times$. Each plot shows the volume averaged barotropic, baroclinic and total horizontal kinetic energy, denoted as $\langle HKE \rangle$, HKE', and HKE, respectively. In every case, the total HKE is dominated by the barotropic part; the only exception in our simulation suite being $Re_f = 50$ and $Fr_f = 0.0707$, where the energy accumulates in a large vertical scale, but not barotropic (not shown). At lower Reynolds numbers, $Re_f \leq 100$, the HKE saturates, while the simulations at $Re_f = 300$ show no indication of saturation, and it is not clear whether it will eventually saturate.

Equation (3.31) shows that vortex stretching and vertical buoyancy flux govern the conversion of VKE to HKE and PE to VKE, respectively. Furthermore, conversion of kinetic energy from the baroclinic component HKE' to the barotropic component $\langle HKE \rangle$ may be understood by multiplying inviscid equations (3.35a) and (3.35b) by $-\langle \psi_0 \rangle$ and $-\psi_0'$ to get
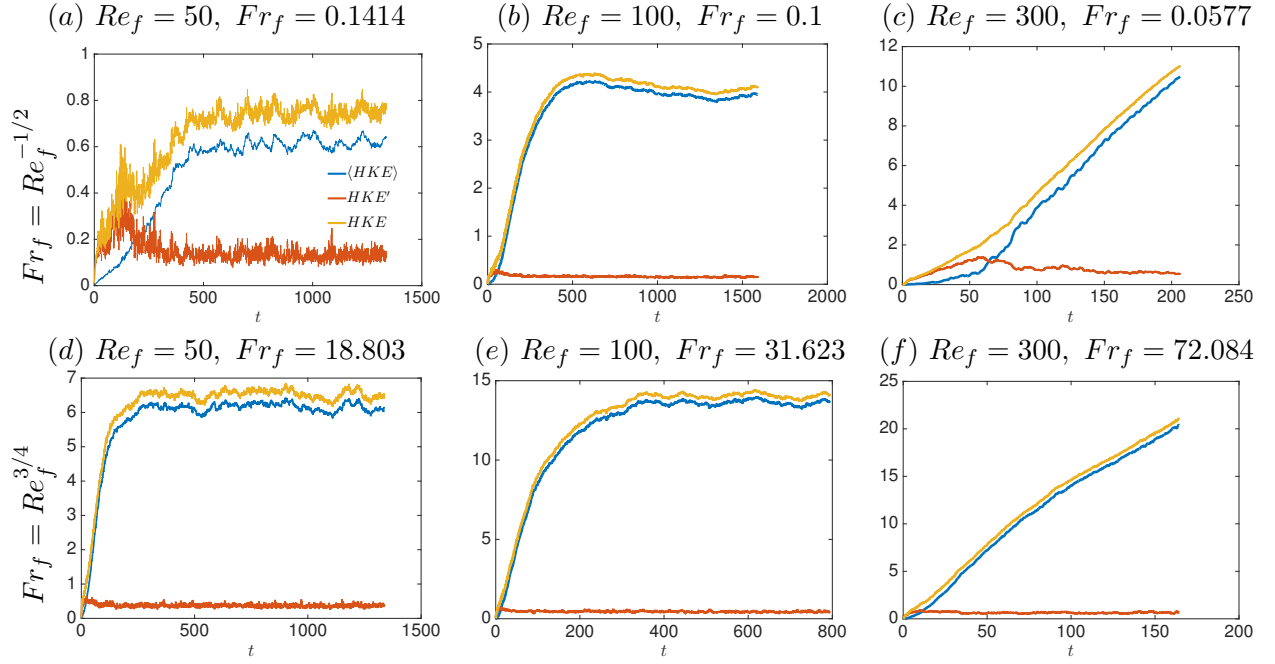
Figure 3.6: Timeseries of volume averaged barotropic, baroclinic and total horizontal kinetic energy at $Fr_f = Re_f^{-1/2}$ (a)-(c) and $Fr_f = Re_f^{3/4}$ (d)-(f). These timeseries correspond to points where an $\times$ sits on the dashed lines in figure 3.2(a). A notable feature is the saturation of HKE at $Re_f = 50$ and $Re_f = 100$. Computationally expensive simulations at $Re_f = 300$ have not equilibrated. The barotropic component $\langle HKE \rangle$ contains nearly all the horizontal kinetic energy after an initial spin-up time.

$$\partial_t \langle HKE \rangle \quad := \quad \partial_t \left[\frac{1}{2} \overline{|\nabla_\perp \langle \psi_0 \rangle|^2}^{\mathcal{A}} \right] = \overline{\langle \psi_0 \rangle \langle J[\psi_0', \zeta_0'] \rangle}^{\mathcal{A}} \tag{3.43a}$$

$$\partial_t HKE' \quad := \quad \partial_t \left[\frac{1}{2} \langle \overline{|\nabla_\perp \psi_0'|^2}^{\mathcal{A}} \rangle \right] = -\overline{\langle \psi_0 \rangle \langle J[\psi_0', \zeta_0'] \rangle}^{\mathcal{A}} + \langle \overline{w_0' \partial_Z \psi_0'}^{\mathcal{A}} \rangle \tag{3.43b}$$

From the above equations it is clear that vortex stretching occurs only within the baroclinic subspace from which the two-dimensional barotropic subspace derives its energy. Moreover, flows for which a dynamic equilibrium is obtained have volume averaged conversion rates that balance dissipation rates. Specifically, by including viscous terms in equations (3.31) and (3.43) and assuming steady states, the following expressions for dissipation rates result

$$\langle HKE_{\text{dissip}} \rangle \quad := \quad -\overline{\langle \psi_0 \rangle \langle J[\psi_0', \zeta_0'] \rangle}^{\mathcal{A}} = -\frac{1}{Re_f} \overline{\langle \zeta_0 \rangle^2}^{\mathcal{A}}, \tag{3.44a}$$

$$HKE'_{\text{dissip}} \quad := \quad \overline{\langle \psi_0 \rangle \langle J[\psi_0', \zeta_0'] \rangle}^{\mathcal{A}} - \langle \overline{w_0' \partial_Z \psi_0'}^{\mathcal{A}} \rangle = -\frac{1}{Re_f} \langle \overline{\zeta_0'^2}^{\mathcal{A}} \rangle, \tag{3.44b}$$

$$VKE_{\text{dissip}} \quad := \quad \langle \overline{w_0 \partial_Z \psi_0}^{\mathcal{A}} \rangle - \langle \overline{w_0 b_0}^{\mathcal{A}} \rangle - \epsilon_f = -\frac{1}{Re_f} \langle \overline{|\nabla_\perp w_0|^2}^{\mathcal{A}} \rangle, \tag{3.44c}$$

$$PE_{\text{dissip}} \quad := \quad \langle \overline{w_0 b_0}^{\mathcal{A}} \rangle = -\frac{1}{Pe_f} \left\langle \frac{\overline{|\nabla_\perp b_0|^2}^{\mathcal{A}}}{\partial_Z \overline{b}_{-1} + Fr_f^{-2} S(Z)} \right\rangle. \tag{3.44d}$$

Summing equations (3.44a) and (3.44b) gives the total dissipation rate of HKE, which matches the total energy conversion by vortex stretching. Summing all dissipation rates in (3.44) gives the total energy dissipation rate, which is precisely the rate ϵ_f at which energy is injected. Figure 3.7 shows volume and time averaged energy conversion rates as functions of Fr_f. These conversions are those given by equations (3.31) and (3.43). Additionally, for equilibrated flow, as is the case for simulations with $Re_f = 50$ and $Re_f = 100$, energy conversion rates in figure 3.7 also provide the dissipation rates given by equation (3.44). In the following we compare and contrast the ways in which energy is converted from one type to another before being eventually dissipated in the two regimes.

From figure 3.7(f) it is clear that in both regimes most of the energy input to VKE is dissipated as VKE. A greater percentage of the total energy input is dissipated as VKE in the
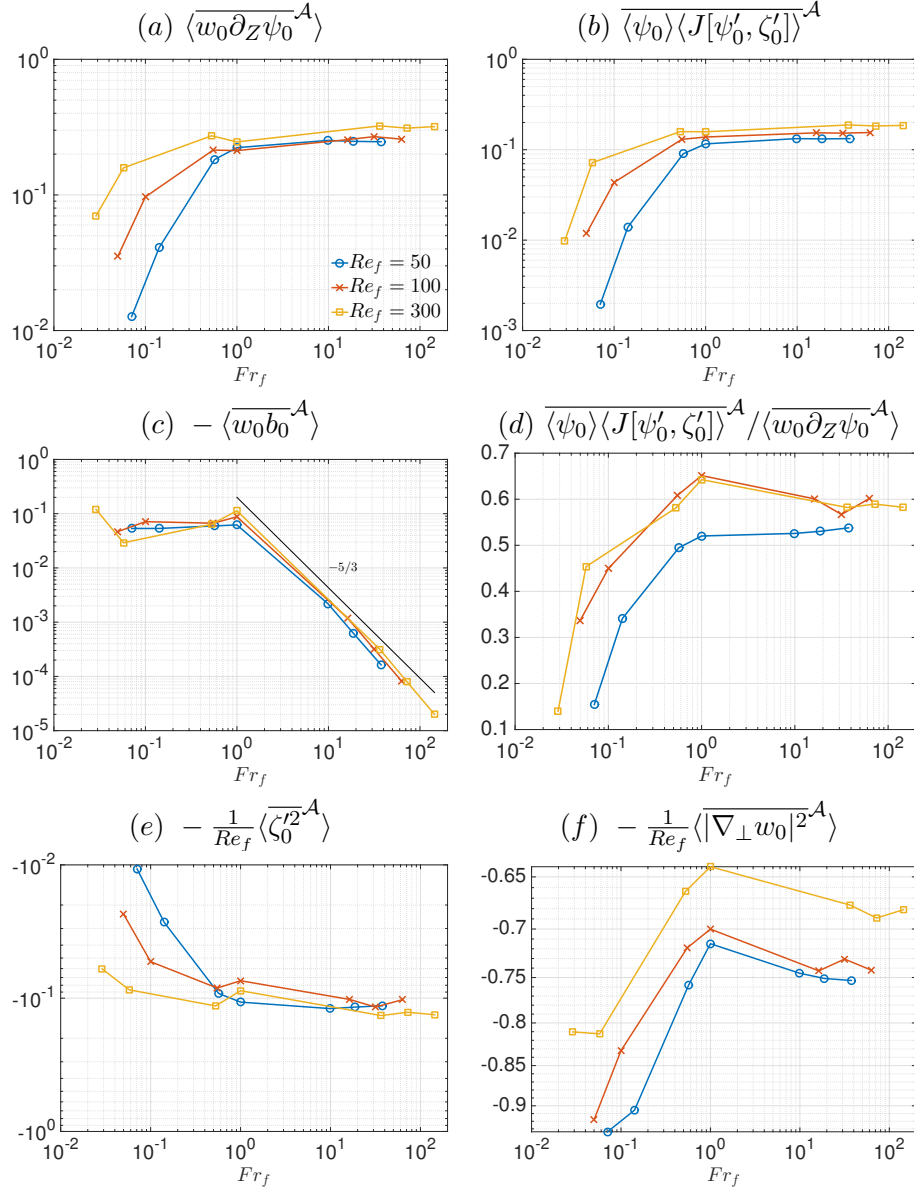
Figure 3.7: Volume and time averaged energy fluxes and dissipation rates for $Re = 50,\ 100,\ 300$ for strong ($Fr_f < 1$) and weak ($Fr_f \geq 1$) stratification. Conversion of kinetic energy via (a) vortex stretching (appearing to be most efficient at $Fr_f \geq 1$), (b) baroclinic forcing, and (c) vertical buoyancy flux (showing the decreased role of PE as Fr_f increases above $Fr_f = 1$). Curves in (d) give the ratio of fluxes due to baroclinic forcing to that due to vortex stretching. Dissipation of HKE' and VKE are given in (e) and (f), respectively. For small values of Fr_f roughly 90 percent of all energy dissipation is done on VKE while it accounts for about 75 percent of energy dissipation at the weakest stratifications.

strong-stratification regime (more than 80%), but a significant amount is still dissipated as VKE in the weak-stratification regime too (65–75%). The vortical mode lacks vertical velocity, and the fact that most of the energy injected to wave modes does not convert to horizontal kinetic or potential energy is an indication of the weakness of the wave-vortex interactions in the rapidly-rotating regime.

Figure 3.7(a) shows the mean energy conversion rate from VKE to HKE by vortex stretching. In the weakly-stratified regime the percentage of total energy injection that is converted to HKE remains around 20%, with a very weak sensitivity to the Reynolds and Froude numbers. By contrast, as the stratification increases past $Fr_f \approx 1$ the rate of conversion to HKE drops rapidly, with less conversion for lower Reynolds numbers. Indeed, of the total input, only approximately 3–4% is converted to HKE at the smallest Froude number at $Re_f = 100$. This is consistent with known results for the strongly-stratified, rapidly-rotating quasigeostrophic regime where wave modes interact extremely weakly with vortical modes.

We next examine conversion of baroclinic to barotropic HKE. From equation (3.35) it is clear that baroclinic motions are solely responsible for exciting barotropic motions. In both regimes of weak and strong stratification, we find that the conversion of baroclinic to barotropic energy ($F = \overline{\langle \psi_0 \rangle \langle J[\psi_0', \zeta_0'] \rangle}^{\mathcal{A}}$) is roughly statistically steady in time and positive. Time averaged values for the conversion F are summarized in figure 3.7(b). Like the rate of conversion from VKE to HKE, the rate of conversion from baroclinic to barotropic HKE is insensitive to Re_f and Fr_f in the weakly-stratified regime, and drops sharply with Fr_f in the strongly-stratified regime. Not only does the gross rate of energy injection to the barotropic mode decrease with Fr_f in the strongly-stratified regime, the percentage of conversion from VKE to HKE that further converts to barotropic HKE decreases too, as shown by figure 3.7(d). For example, at the smallest Froude number and at $Re_f = 100$ less than 40% of the conversion to HKE further converts to barotropic HKE. As mentioned above, the simulation with $Re_f = 50$ at the strongest stratification does not exhibit barotropization, which may be due to an insufficient $\mathcal{O}(10^{-3})$ energy flux into the barotropic mode compared to viscous dissipation (see figures 3.7(b) and 3.7(e)).

Clearly, the saturation of the barotropic energy observed at moderate Reynolds numbers is not the result of a shutdown of injection to the barotropic mode. The fact that the barotropic energy saturates despite a net positive energy injection indicates that there must be a net dissipation to balance the forcing. None of our simulations use a large-scale dissipation, so the barotropic dissipation must be viscous. In section 3.5.3 we diagnose a small yet robust **direct** cascade of barotropic kinetic energy that carries enough energy to small scale dissipation that the total barotropic energy is able to equilibrate at $Re_f \leq 100$.

Energy injected directly to VKE also converts to potential energy; the mean rate of conversion from VKE to PE is shown in figure 3.7(c). This conversion out of VKE displays somewhat opposite behavior to the conversion from VKE to HKE: in the strongly-stratified regime the conversion remains flat, insensitive to both Reynolds and Froude numbers, while in the weakly-stratified regime the conversion decreases rapidly as the stratification weakens and with little dependence on Reynolds number.

To summarize, in both regimes energy injected to VKE is primarily dissipated as VKE, and there is a net positive conversion to barotropic KE that is, for moderate Reynolds numbers, balanced by dissipation leading to total energy equilibration. In the strongly-stratified regime the conversion to baroclinic HKE decreases with Fr_f, as does the rate of conversion to barotropic HKE, while the rate of conversion to PE remains moderate and insensitive to Fr_f. In the weakly-stratified regime the conversion to baroclinic HKE remains moderate and insensitive to Fr_f, as does the rate of conversion to barotropic HKE, while the rate of conversion to PE decreases rapidly as Fr_f increases.

3.5.3   Cospectra and scales active in energy conversion

While illuminating, the discussion in section 3.5.2 is based on global scalars obtained from volume and time averages and is altogether lacking any spatial information. To improve on this, vertically and time averaged cospectra are computed. These one-dimensional cospectra are calculated by decomposing horizontal means of point-wise physical space products as a the sum of Fourier
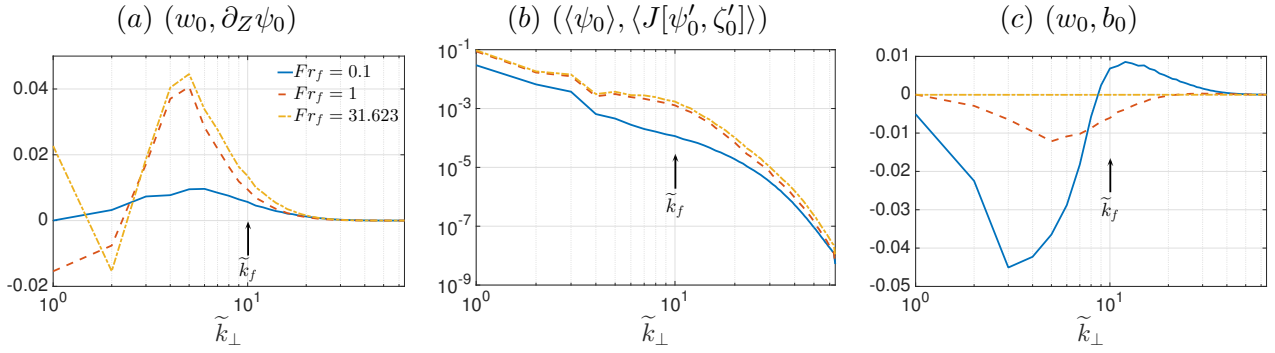
Figure 3.8: Vertically and time averaged horizontal cospectra of energy fluxes at $Re_f = 100$ for times proceeding energy saturation. Cospectra in (a) give conversions between HKE and VKE by vortex stretching, (b) give the barotropization of HKE and indicate a flux of HKE' into the gravest horizontal mode at $\widetilde{k}_\perp = 1$, and (c) give conversions between VKE and PE by vertical buoyancy flux and strongly indicate that these conversion become increasingly weak as Fr_f increases beyond unity.

space products, reordering sums over circular rings, binning, and averaging in the $\hat{z}$ direction, i.e.,

$$(f,g)(\widetilde{k}_\perp) = \langle \sum_{0<|\widetilde{k}'_\perp - \widetilde{k}_\perp|\leq 1} \overline{\hat{f}}(k'_\perp, Z)\hat{g}(k'_\perp, Z)\rangle, \quad \widetilde{k}_\perp = \frac{k_\perp}{k_0} = 1, 2, 3, \ldots \quad (3.45)$$

where $\widetilde{k}_\perp$ and $\widetilde{k}'_\perp$ are horizontal wavenumbers normalized by the box scale $k_0 = 2\pi/L_b$, the bar here denotes complex conjugation, hats denote horizontal Fourier amplitudes, and angle brackets denote a vertical average. Furthermore, the temporal mean of cospectra are computed to provide the scales active in energy conversion on average. Figure 3.8 shows cospectra of vortex stretching, barotropization of HKE, and vertical buoyancy flux for simulations with $Re_f = 100$ and with $Fr_f = Re_f^{-1/2}$, 1, $Re_f^{3/4}$. Similar cospectra are observed for $Re_f = 50$ and $Re_f = 300$. Although simulations with $Re_f = 300$ have not reached a dynamic equilibrium they too convey the trends observed for $Re_f = 100$ in figure 3.8.

For the strongest stratification, figure 3.8(a) indicates that conversion to HKE' by vortex stretching occurs at all available scales with a preference for $\widetilde{k}_\perp \approx 5$ (or $L \approx 2L_f$), and may hint at a preferred scale for wave-vortex interactions. The centroid (or the average wavenumber) active for this energy conversion by vortex stretching is just less than $\widetilde{k}_f = 10$ (or $L \approx L_f = 1$), however, the efficiency of vortex stretching is best at $L = 2L_f$. The barotropization of HKE in figure 3.8(b) shows that horizontal baroclinic motions act to force barotropic motions at all scales, however, with a strong preference for the largest available horizontal scale. That this baroclinic forcing is, on average, positive definite is consistent with equation (3.44a) and implies that this barotropized energy is trapped in the barotropic mode until it is viscously dissipated. Figure 3.8(c) shows that the conversion between PE and VKE depends on scale: VKE is converted to PE for $\widetilde{k}_\perp < \widetilde{k}_f$, and PE is converted back to VKE for $\widetilde{k}_\perp \gtrsim \widetilde{k}_f$ with a net conversion to PE and a peak efficiency at $\widetilde{k}_\perp = 3$ ($L \approx 3.3L_f$).

When stratification weakens and $Fr_f = 1$, there is still a net conversion from VKE to HKE by vortex stretching, but that for stronger stratification stretching converts horizontal kinetic energy back to vertical kinetic energy at the two largest available scales ($\widetilde{k}_\perp = 1$, 2). Vortex stretching

continues to most efficiently convert vertical to horizontal kinetic energy at $\widetilde{k}_\perp = 5$ $(L = 2L_f)$, and is nearly four times the conversion seen at stronger stratification. Baroclinic motions continue to drive barotropic motions in a fashion similar to that at stronger stratification, however, this is done with slightly increased efficiency especially for $5 < \widetilde{k}_\perp < 20$ (figure 3.8(b)). Potential energy becomes weak to the point were the feedback to vertical kinetic energy for $\widetilde{k}_\perp > \widetilde{k}_f$ is substantially reduced and a preference to convert vertical to potential energy at scales $\widetilde{k}_\perp = 5$ $(L = 2L_f)$ is smaller than that at $Fr_f = Re_f^{-1/2}$.

Finally, for the weakest stratification where $Fr_f = Re^{3/4}$, conversion from VKE to HKE is very similar to $Fr_f = 1$, with the exception that conversion back to vertical kinetic energy only occurs at $\tilde{k}_\perp = 2$ rather than both $\tilde{k}_\perp = 1$ and 2. At all other scales vortex stretching acts to move energy from vertical motions to baroclinic horizontal motions and does so most efficiently near $\tilde{k}_\perp = 5$. That the largest scale now plays a role via vortex stretching in converting vertical to horizontal energy (contrary to what occurs when $Fr_f = 1$) might be explained by an increased pool of energy made available by the decreased role of buoyancy (see figure 3.7(c)). Barotropization of horizontal kinetic energy, forced by baroclinic motions, is virtually identical to $Fr_f = 1$ and figure 3.8(c) iterates the insignificance of buoyancy and an approach to purely rotating dynamics.

3.5.4   Energy spectra

Vertically and time averaged horizontal energy spectra for simulations with $Re_f = 300$, $Fr_f = 0.0577$, and $Fr_f = 72.084$ are computed using equation (3.45) and are given in figure 3.9. Similar spectra are observed for remaining values of Fr_f and at lower Re_f. Both plots give barotropic, $\langle HKE \rangle = (-\langle \psi_0 \rangle, \langle \zeta_0 \rangle)$, and baroclinic, $HKE' = (-\psi_0', \zeta_0')$, components of the total horizontal kinetic energy spectrum, $HKE = (-\psi_0, \zeta_0)$.

For both strong and weak stratification a $\widetilde{k}_\perp^{-3}$ energy spectrum for $\widetilde{k}_\perp \in [1, 3]$ is dominated by barotropic energy. For strong stratification the barotropic energy drops off steeply as $\widetilde{k}_\perp^{-20/3}$ for $k_\perp \in [3, 8]$, and gives way to a $\widetilde{k}_\perp^{-3}$ scaling below the forcing scale. At weak stratification the steep scaling is short-lived and the barotropic spectrum quickly gives way to a $\widetilde{k}_\perp^{-3}$ scaling near the
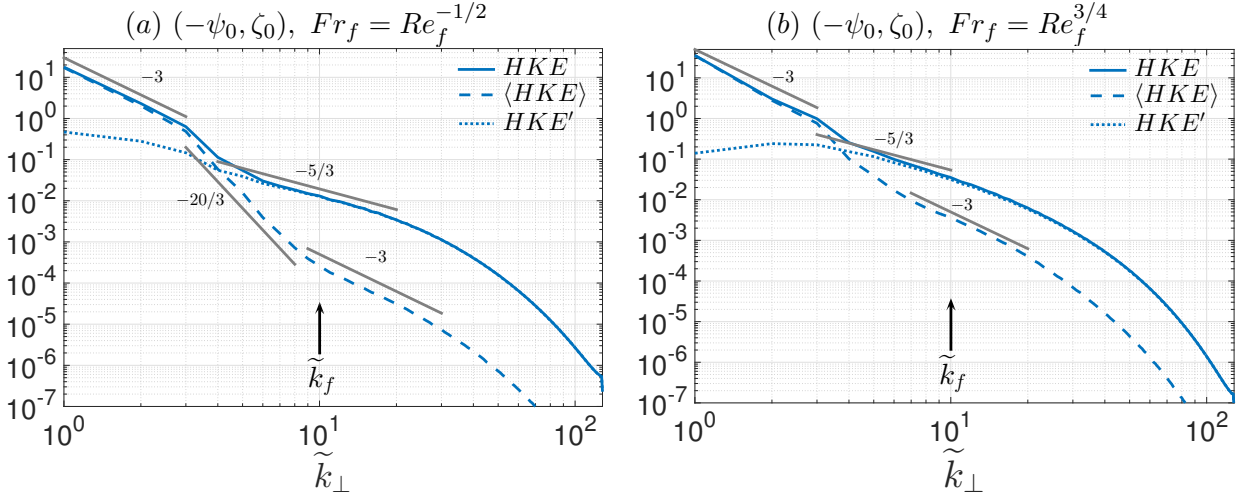
Figure 3.9: Vertically and temporally averaged horizontal energy spectra for $Re_f = 300$ with (a) $Fr_f = 0.0577$ and (b) $Fr_f = 72.084$. Each figure shows the barotropic, $\langle HKE \rangle = (-\langle \psi_0 \rangle, \langle \zeta_0 \rangle)$, and baroclinic, $HKE' = (-\psi_0', \zeta_0')$, components of horizontal kinetic energy spectra, $HKE = (-\psi_0, \zeta_0)$. A $k_\perp^{-3}$ energy spectra at small wavenumber is due to energy containing scales in the barotropic subspace for both strong and weak stratification. For strong stratification and larger wavenumber a steep $k_\perp^{-20/3}$ scaling for barotropic energy gives way to a $k_\perp^{-3}$ scaling near the dissipation range. For weak stratification the steep scaling is short-lived.

forcing scale. The presence (absence) of the steep drop-off in energy for strong (weak) stratification might be explained, to some extent, by the weaker (stronger) baroclinic forcing for $\widetilde{k}_\perp \in [3, 8]$ (see figure 3.8(b)), indeed, the shape of the forcing cospectrum decreases (sustains) in this range. In turn, the difference in behavior of baroclinic forcing might be explained by flow morphology. At strong stratification horizontal layers appear and are associated with increased viscous effects that may disrupt collinearity of baroclinic advection of the baroclinic vorticity with the barotropic streamfunction (figure 3.8(b)). When layers are absent at weaker stratification so are associated regions of increased viscous effects and the result is an increased efficiency of baroclinic forcing (figure 3.8(b)).

For strong stratification, as $\widetilde{k}_\perp$ increases and barotropic energy becomes subdominant, the baroclinic energy spectra scales as $\widetilde{k}_\perp^{-5/3}$ for $\widetilde{k}_\perp \in [4, \approx 20]$. When stratification is weaker this scaling range appears to narrow, which may be explained by increased vortex stretching which acts to force baroclinic energy most efficiency in the range $\widetilde{k}_\perp \in [4, 5]$.

3.5.5 Barotropization and inverse cascade

It is interesting to consider the barotropic dynamics since these motions are governed by the two-dimensional vorticity equation (3.35a). If two-dimensional dissipative flow is forced at scales well separated from frictional effects acting on energy and enstrophy then an upscale energy range and a downscale enstrophy range form where, in the limit of vanishing viscosity the downscale transfer of energy through the enstrophy range is expected to vanish. In our simulations, of the energy converted to baroclinic HKE by vortex stretching a fraction (which depends on Fr_f) acts to force the barotropic vorticity equation (see figure 3.7(d)). Figure 3.8(b) illustrates that baroclinic motions establish a natural injection of energy directly into the gravest barotropic mode, so that the accumulation of energy at large scales in the barotropic mode does not result primarily from a two-dimensional inverse-cascade process. Dissipation in the barotropic subspace, therefore, occurs through a nonzero forward energy cascade. Figure 3.10 gives a detailed map of the transfer of energy between barotropic Fourier modes performed by barotropic triad interactions for equilibrated flow
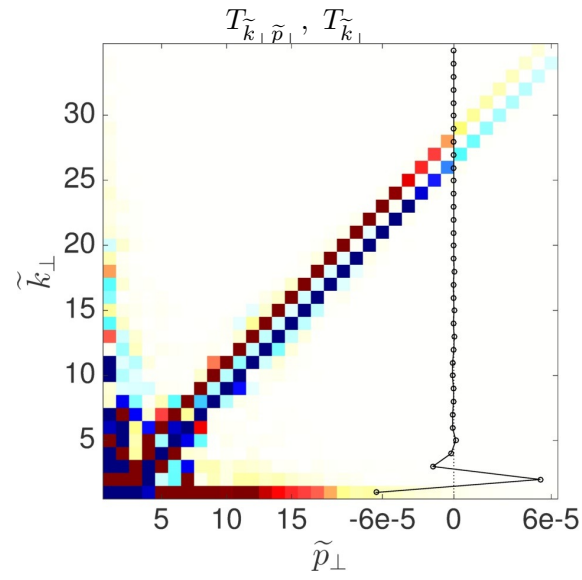
Figure 3.10: Energy transfer map showing how barotropic triad interactions move energy within the barotropic subspace for equilibrated dynamics where $Re_f = 100$ and $Fr_f = 0.1$. The vertical profile (on the right) is the result of summing the transfer map $T_{k_\perp p_\perp}$ over $p_\perp$ to get $T_{k_\perp}$. Note the scale for $T_{k_\perp}$ is $\mathcal{O}(10^{-5})$, an indication that energy transfer via triad interaction are weak relative to baroclinic forcing. Similar results are seen for weak stratification. Red (blue) shading indicates that energy is transferred into (out of) wavenumber $\widetilde{k}_\perp$ through interactions with wavenumber $\widetilde{p}_\perp$.

at $Re_f = 100$ (Rubio et al., 2014). The near-diagonal elements of this map at large wavenumber show a local forward transfer of energy to small scales coexisting with a non-local inverse cascade at larger scales. The accumulation of energy at large horizontal scales in the barotropic mode in these rapidly rotating flows is primarily the result of three-dimensional baroclinic motions interacting to directly induce large-scale and vertically-invariant structures; it is not primarily a result of baroclinic injection to an intermediate scale, followed by a purely-barotropic inverse cascade to larger scales.

3.6   Vortical and wave modes for $Ro_f \ll 1$ and $Fr_f \sim 1$

This section provides a brief introduction to the vortical and wave eigenmodes of the reduced NH-QG equations. Note that the terms "eigenmode," "eigenfunction," and simply "mode" are used interchangeably to refer to the decomposition of the fluid state at a prescribed wavenumber $\boldsymbol{k}$. In the literature, the vortical and wave modes are sometimes referred to as the geostrophic and ageostrophic modes, respectively, however in the context of the NH-QG equations where solutions satisfy a point-wise geostrophic balance such a categorization does not make sense. For this reason, when dealing with the NH-QG equations we will refer to these modes as vortical and wave modes. The initial goal here is to obtain a decomposition of solutions to the linear NH-QG equations similar to that obtained by Bartello (1995), however this is done for the NH-QG equations valid for $Ro \ll 1$ and $Fr = \mathcal{O}(1)$, a regime of increasing importance with increased attention to small-scale oceanic motions where non-hydrostatic effects become important. Once such a decomposition is obtained we take note of the linear independence of eigenvectors and use their basis expansion in the expression of nonlinear terms. It is noted that such an analysis is also carried out by (Warn, 1986) for the shallow water equations.

It is hard to emphasize enough that the NH-QG equations are valid for $Fr = \mathcal{O}(1)$.

We make use of the toroidal-poloidal decomposition which automatically satisfies leading-order geostrophy. We consider the an inviscid and unforced fluid linearized about a state of rest using the NH-QG equations with stable stratification $S(Z) = 1$ and in terms of the geostrophic

streamfunction ψ, velocity potential ϕ. Dropping subscripts indicating asymptotic order the equations become

$$\partial_t \nabla_\perp^2 \psi - \partial_Z \nabla_\perp^2 \phi = 0, \tag{3.46a}$$

$$\partial_t \nabla_\perp^2 \phi + \partial_Z \psi = b, \tag{3.46b}$$

$$\partial_t b + \frac{\nabla_\perp^2 \phi}{Fr^2} = 0, \tag{3.46c}$$

$$\partial_T \bar{b}_{-1} = 0. \tag{3.46d}$$

Here $\bar{b}_{-1}$ is slowly varying in time and decoupled from the remaining fluctuating quantities. We continue to work in a triply-periodic domain so that fluid variables are expressed as Fourier series

$$\begin{pmatrix} \psi \\ \phi \\ b \end{pmatrix} (x, y, Z, t) = \sum_{\boldsymbol{k}} \begin{pmatrix} \hat{\psi}_{\boldsymbol{k}} \\ \hat{\phi}_{\boldsymbol{k}} \\ \hat{b}_{\boldsymbol{k}} \end{pmatrix} (t) e^{i\boldsymbol{k}\cdot\boldsymbol{x}}, \tag{3.47}$$

where

$$\boldsymbol{k} = (\boldsymbol{k}_\perp, k_Z) = (k_x, k_y, k_Z) \in \mathbb{Z}^3. \tag{3.48}$$

The Fourier coefficients at a given wavenumber $\boldsymbol{k}$ satisfy one of three different systems depending on which set $\boldsymbol{k}$ belongs to: the barotropic set where $k_Z = 0$, the baroclinic set where $k_Z \neq 0$, and the horizontally averaged set where $k_\perp = 0$. Substituting (3.47) into (3.46) the linear NH-QG system at a single Fourier mode satisfies (assuming $k_\perp \neq 0$)

$$\partial_t \begin{pmatrix} -k_\perp^2 \hat{\psi}_{\boldsymbol{k}} \\ -k_\perp^2 \hat{\phi}_{\boldsymbol{k}} \\ \hat{b}_{\boldsymbol{k}} \end{pmatrix} = \begin{pmatrix} 0 & ik_Z & 0 \\ \frac{ik_Z}{k_\perp^2} & 0 & 1 \\ 0 & -\frac{1}{Fr^2} & 0 \end{pmatrix} \begin{pmatrix} -k_\perp^2 \hat{\psi}_{\boldsymbol{k}} \\ -k_\perp^2 \hat{\phi}_{\boldsymbol{k}} \\ \hat{b}_{\boldsymbol{k}} \end{pmatrix}. \tag{3.49}$$

However, when $k_\perp = 0$ (or $\theta = \tan^{-1}(k_\perp/kZ) = 0$) the system (3.46) is in hydrostatic balance where $(u, v, w) = (-\partial_y \psi, \partial_x \psi, \nabla_\perp^2 \phi) = \boldsymbol{0}$, b and ψ are *slowly* varying. For the Boussinesq equations such a state where $k_\perp = 0$ corresponds to pure inertial waves, however for the NH-QG equations

pure inertial waves are absent (a consequence of the large aspect ratio dynamics/scaling that filters these fast waves see §3.2.2). Given that flow described by the NH-QG equations trivializes to a quiescent state when $k_\perp = 0$ we no long consider this case. We may, if we wish, consider separately the dynamics associated with the case where $k_Z = 0$, however, this follows immediately from the results of the linear analysis with $k_\perp \neq 0$ and $k_Z \neq 0$. The following change of variables elucidates the linear wave solutions

$$
\begin{pmatrix} -k_\perp^2 \hat{\psi}_{\boldsymbol{k}} \\ ik_\perp^3 \hat{\phi}_{\boldsymbol{k}} \\ Frk_\perp \hat{b}_{\boldsymbol{k}} \end{pmatrix} = \begin{pmatrix} 1 & 0 & 0 \\ 0 & -ik_\perp & 0 \\ 0 & 0 & Frk_\perp \end{pmatrix} \begin{pmatrix} -k_\perp^2 \hat{\psi}_{\boldsymbol{k}} \\ -k_\perp^2 \hat{\phi}_{\boldsymbol{k}} \\ \hat{b}_{\boldsymbol{k}} \end{pmatrix},
\tag{3.50}
$$

where, $P_{\boldsymbol{k}} = \mathrm{diag}[1, -ik_\perp, Frk_\perp]$. Upon writing $(-k_\perp^2 \hat{\psi}_{\boldsymbol{k}}, ik_\perp^3 \hat{\phi}_{\boldsymbol{k}}, Frk_\perp \hat{b}_{\boldsymbol{k}})^T = (\hat{\zeta}_{\boldsymbol{k}}, -ik_\perp \hat{w}_{\boldsymbol{k}}, Frk_\perp \hat{b}_{\boldsymbol{k}})^T$, the linear system may be written as

$$
\partial_t \begin{pmatrix} \hat{\zeta}_{\boldsymbol{k}} \\ -ik_\perp \hat{w}_{\boldsymbol{k}} \\ Frk_\perp \hat{b}_{\boldsymbol{k}} \end{pmatrix} = i \begin{pmatrix} 0 & ik_Z/k_\perp & 0 \\ -ik_Z/k_\perp & 0 & -1/Fr \\ 0 & -1/Fr & 0 \end{pmatrix} \begin{pmatrix} \hat{\zeta}_{\boldsymbol{k}} \\ -ik_\perp \hat{w}_{\boldsymbol{k}} \\ Frk_\perp \hat{b}_{\boldsymbol{k}} \end{pmatrix},
\tag{3.51}
$$

which is *similar* to the system (3.49) (i.e., they share the same spectrum). It is worth noting that conditions for real-valued solutions become $\hat{\zeta}_{\boldsymbol{k}}^* = \hat{\zeta}_{-\boldsymbol{k}}$, $\hat{w}_{\boldsymbol{k}}^* = -\hat{w}_{-\boldsymbol{k}}$, and $\hat{b}_{\boldsymbol{k}}^* = \hat{b}_{-\boldsymbol{k}}$. Alternatively, we may write (3.51) as

$$
\partial_t \boldsymbol{v}_{\boldsymbol{k}} = i\mathcal{L}_{\boldsymbol{k}} \boldsymbol{v}_{\boldsymbol{k}}
\tag{3.52}
$$

where $\boldsymbol{v}_{\boldsymbol{k}} = (\hat{\zeta}_{\boldsymbol{k}}, -ik_\perp \hat{w}_{\boldsymbol{k}}, Frk_\perp \hat{b}_{\boldsymbol{k}})^T$. We note that $\mathcal{L}_{\boldsymbol{k}}$ is self-adjoint, therefore the operator $\mathcal{A} = i\mathcal{L}_{\boldsymbol{k}}$ is skew-adjoint and we expect solutions to display oscillatory behavior (i.e., the system has purely imaginary eigenvalues). The eigenvalues for $\mathcal{A} = i\mathcal{L}_{\boldsymbol{k}}$ are

$$
\lambda_{\boldsymbol{k}}^0 = 0, \quad \lambda_{\boldsymbol{k}}^\pm = \pm i\sqrt{\frac{1}{Fr^2} + \frac{k_Z^2}{k_\perp^2}} = \pm i\omega_{\boldsymbol{k}},
\tag{3.53}
$$

with associated eigenvectors

$$\boldsymbol{\xi}_{\boldsymbol{k}}^0 = \frac{1}{\omega_{\boldsymbol{k}} k_\perp} \begin{pmatrix} k_\perp/Fr \\ 0 \\ -ik_Z \end{pmatrix}, \quad \boldsymbol{\xi}_{\boldsymbol{k}}^\pm = \frac{1}{2^{1/2}\omega_{\boldsymbol{k}} k_\perp} \begin{pmatrix} \pm ik_Z \\ \omega_{\boldsymbol{k}} k_\perp \\ \mp k_\perp/Fr \end{pmatrix}. \tag{3.54}$$

where $\omega_{\boldsymbol{k}} = (1/Fr^2 + k_Z^2/k_\perp^2)^{1/2}$, and the eigenvectors are normalized to satisfy the orthogonality condition $\langle \boldsymbol{\xi}_{\boldsymbol{k}}^i, \boldsymbol{\xi}_{\boldsymbol{k}}^j \rangle \equiv \boldsymbol{\xi}_{\boldsymbol{k}}^{i\dagger} \boldsymbol{\xi}_{\boldsymbol{k}}^j = \omega_{i,j}$ (where $\dagger$ denotes complex-conjugate transpose), therefore eigenvectors form the columns of the unitary matrix $U_{\boldsymbol{k}} = (\boldsymbol{\xi}_{\boldsymbol{k}}^0, \boldsymbol{\xi}_{\boldsymbol{k}}^-, \boldsymbol{\xi}_{\boldsymbol{k}}^+)$. Moreover, the state of the system at any time t and wavenumber $\boldsymbol{k}$ can be uniquely expressed by the linear combination

$$\boldsymbol{v}_{\boldsymbol{k}} = \left(\boldsymbol{\xi}_{\boldsymbol{k}}^0, \boldsymbol{\xi}_{\boldsymbol{k}}^-, \boldsymbol{\xi}_{\boldsymbol{k}}^+ \right) \begin{pmatrix} C_{\boldsymbol{k}}^0 \\ C_{\boldsymbol{k}}^- \\ C_{\boldsymbol{k}}^+ \end{pmatrix} (t) = U_{\boldsymbol{k}} \boldsymbol{C}_{\boldsymbol{k}} = \sum_{i=0,\pm} C_{\boldsymbol{k}}^i(t) \boldsymbol{\xi}_{\boldsymbol{k}}^i. \tag{3.55}$$

Upon substituting this decomposition into (3.52) and using orthogonality gives the relation

$$\partial_t C_{\boldsymbol{k}}^i = \lambda_{\boldsymbol{k}}^i C_{\boldsymbol{k}}^i \tag{3.56}$$

for $i = 0, \pm$, therefore define

$$V_{\boldsymbol{k}} = C_{\boldsymbol{k}}^0, \qquad C_{\boldsymbol{k}}^\pm = G_{\boldsymbol{k}}^\pm e^{\lambda_{\boldsymbol{k}}^\pm t} \tag{3.57}$$

It is clear from (3.55) that solutions may either be built from or decomposed into the modal amplitudes $\boldsymbol{C}_{\boldsymbol{k}}$. Projections onto eigenvectors $\boldsymbol{\xi}_{\boldsymbol{k}}^i$ yields the the modal amplitudes via $\boldsymbol{C}_{\boldsymbol{k}} = U^\dagger \boldsymbol{v}_{\boldsymbol{k}}$ giving

$$C_{\boldsymbol{k}}^0 = \frac{Fr^{-1} k_\perp \hat{\zeta}_{\boldsymbol{k}} + ik_Z k_\perp Fr \hat{b}_{\boldsymbol{k}}}{\omega_{\boldsymbol{k}} k_\perp}, \tag{3.58a}$$

$$C_{\boldsymbol{k}}^\pm = \frac{-ik_\perp^2 \omega_{\boldsymbol{k}} \hat{w}_{\boldsymbol{k}} \mp ik_Z \hat{\zeta}_{\boldsymbol{k}} \mp k_\perp^2 \hat{b}_{\boldsymbol{k}}}{2^{1/2} \omega_{\boldsymbol{k}} k_\perp}. \tag{3.58b}$$

Inspection of these modal amplitudes and eigenvectors conveys the fluid motions they describe. The slowly evolving mode with zero frequency and amplitude corresponds to horizontal rotational

motions which is made obvious by considering the eigenfunction $\boldsymbol{\xi}_{\boldsymbol{k}}^{0}$ which lacks vertical velocity, therefore describes horizontal flow in hydrostatic balance. The remaining inertial-gravity mode with amplitudes $C_{\boldsymbol{k}}^{\pm}$ and eigenfunctions $\boldsymbol{\xi}_{\boldsymbol{k}}^{\pm}$ are referred to as such since these satisfy the inertial-gravity linear dispersion relation.

This analysis separates the dynamics at a given wavenumber $\boldsymbol{k}$ into components with *slow* variation (no linear/localized variation) and oscillatory (wave) dynamics that vary (relative to the slow dynamics) rapidly, denoted with subscripts $i = 0, \pm$ respectively. Moreover, the fluid state may now be expressed uniquely as

$$\boldsymbol{Y}(x,y,Z,t) = \sum_{\boldsymbol{k}} \sum_{s_{\boldsymbol{k}}=0,\pm} C_{\boldsymbol{k}}^{s_{\boldsymbol{k}}}(t) \boldsymbol{\xi}_{\boldsymbol{k}}^{s_{\boldsymbol{k}}} e^{i\boldsymbol{k}\cdot\boldsymbol{x}}, \tag{3.59}$$

where the modal amplitudes and eigenvectors satisfy the properties

$$C_{\boldsymbol{k}}^{s_{\boldsymbol{k}}*} = C_{-\boldsymbol{k}}^{s_{\boldsymbol{k}}}, \qquad \boldsymbol{\xi}_{\boldsymbol{k}}^{s_{\boldsymbol{k}}*} = \boldsymbol{\xi}_{-\boldsymbol{k}}^{s_{\boldsymbol{k}}}, \tag{3.60}$$

yielding real-valued solutions $\boldsymbol{Y}$ (where asterisks denote complex-conjugation).

3.6.1 Modal energy

Thus far the linear analysis of the reduced NH-QG bears strong similarities with the analysis presented by Bartello (1995), with the exception of differences due to aspect ratio and the simplification of the dynamics with $k_{\perp} = 0$. The energy at $k_{\perp} = 0$ has been observed to tend to zero with decreasing Ro in simulations by Waite and Bartello (2006) who claim that in such a regime energy transfer into this "shear" mode ceases, or at the very least, is significantly inhibited. From the perspective of the NH-QG equations we claim that transfer into this mode is asymptotically weak in the limit $Ro \ll 1$ for $Fr \sim 1$. Working forward from here we take note of contrasting definitions for the terms "barotropic" and "baroclinic" described in §3.3.2 from that implied by Bartello (1995). In the present study the baroclinic dynamics are entirely represented by vertical velocity, buoyancy and depth-dependent horizontal velocity, while barotropic dynamics are exactly the depth-independent component of horizontal velocity. The total energy $E = HKE + VKE + PE$,

decomposed as the sum of horizontal and vertical kinetic energy and potential energy, may be written as

$$E \quad = \quad \langle \overline{|\nabla_\perp \psi|^2} + \overline{w^2} + \overline{(Frb)^2} \rangle \tag{3.61a}$$

$$= \quad \sum_{\boldsymbol{k}} k_\perp^2 |\hat{\psi}_{\boldsymbol{k}}|^2 + |\hat{w}_{\boldsymbol{k}}|^2 + Fr^2 |\hat{b}_{\boldsymbol{k}}|^2 \tag{3.61b}$$

$$= \quad \sum_{\boldsymbol{k}} k_\perp^{-2} \left(|\hat{\zeta}_{\boldsymbol{k}}|^2 + k_\perp^2 |\hat{w}_{\boldsymbol{k}}|^2 + k_\perp^2 Fr^2 |\hat{b}_{\boldsymbol{k}}|^2 \right) \tag{3.61c}$$

$$= \quad \sum_{\boldsymbol{k}} k_\perp^{-2} \boldsymbol{v}_{\boldsymbol{k}}^\dagger \boldsymbol{v}_{\boldsymbol{k}} = \sum_{\boldsymbol{k}} k_\perp^{-2} \boldsymbol{C}_{\boldsymbol{k}}^\dagger \boldsymbol{C}_{\boldsymbol{k}} \tag{3.61d}$$

where the last line uses (3.55) and the fact that U is unitary and shows the manner in which energy at wavenumber $\boldsymbol{k}$ may be partitioned among slow and fast dynamics. Therefore, define the energy $E_{\boldsymbol{k}}$ at wavenumber $\boldsymbol{k}$ by

$$E_{\boldsymbol{k}} \quad = \quad k_\perp^{-2} \boldsymbol{C}_{\boldsymbol{k}}^\dagger \boldsymbol{C}_{\boldsymbol{k}} \tag{3.62a}$$

$$= \quad k_\perp^{-2} \left(|C_{\boldsymbol{k}}^0|^2 + |C_{\boldsymbol{k}}^-|^2 + |C_{\boldsymbol{k}}^+|^2 \right). \tag{3.62b}$$

3.6.2 Nonlinear wave-eddy interactions

As mentioned in §3.2.2, when $Ro \ll 1$ and $Fr \sim 1$ there is no clear time scale separation between wave periods and the eddy-turnover time, on the other hand these values for Ro and Fr allow for an increased range of resonant interactions. With this in mind we introduce the expression (3.59) into the inviscid and nonlinear NH-QG equations

$$\partial_t \boldsymbol{Y} = i\mathcal{L}\boldsymbol{Y} - \boldsymbol{N} \tag{3.63}$$

where, upon taking Fourier transforms and using orthogonality eigenvectors of $i\mathcal{L}$, the equation governing modal amplitudes $C_{\boldsymbol{k}}^{s_{\boldsymbol{k}}}$ at wavenumber $\boldsymbol{k}$ is given by

$$\left(\partial_t - \lambda_{\boldsymbol{k}}^{s_{\boldsymbol{k}}} \right) C_{\boldsymbol{k}}^{s_{\boldsymbol{k}}} = \sum_{\boldsymbol{k}=\boldsymbol{p}+\boldsymbol{q}} \sum_{s_{\boldsymbol{p}}=0,\pm} \sum_{s_{\boldsymbol{q}}=0,\pm} N_{\boldsymbol{k},\boldsymbol{p},\boldsymbol{q}}^{s_{\boldsymbol{k}},s_{\boldsymbol{p}},s_{\boldsymbol{q}}} C_{\boldsymbol{p}}^{s_{\boldsymbol{p}}} C_{\boldsymbol{q}}^{s_{\boldsymbol{q}}}, \tag{3.64}$$

where $s_{\boldsymbol{k}} = 0, \pm$, $\boldsymbol{k} = \boldsymbol{p} + \boldsymbol{q}$ gives the condition for triadic interactions where

$$N_{\boldsymbol{k},\boldsymbol{p},\boldsymbol{q}}^{s_{\boldsymbol{k}},s_{\boldsymbol{p}},s_{\boldsymbol{q}}} = N(\boldsymbol{p}_\perp, \boldsymbol{q}_\perp) \left(\hat{\boldsymbol{x}} \cdot \boldsymbol{\xi}_{\boldsymbol{p}}^{s_{\boldsymbol{p}}} \right) \left(P_{\boldsymbol{k}}^\dagger \boldsymbol{\xi}_{\boldsymbol{k}}^{s_{\boldsymbol{k}}} \right)^\dagger \boldsymbol{\xi}_{\boldsymbol{q}}^{s_{\boldsymbol{q}}}, \tag{3.65}$$

$$N(\boldsymbol{p}_\perp, \boldsymbol{q}_\perp) = N(\boldsymbol{q}_\perp, \boldsymbol{p}_\perp) = \frac{\hat{\boldsymbol{z}} \cdot \boldsymbol{p}_\perp \times \boldsymbol{p}_\perp}{2p_\perp^2 q_\perp^2}\left(p_\perp^2 - q_\perp^2\right). \tag{3.66}$$

Equation (3.67) exemplifies that linear wave dynamics and variation due nonlinearities occur on the same time scale. Specifically, when $Fr \sim 1$ (moderate stratification) or $Fr \gg 1$ (weak stratification) then corresponding wave frequencies are $\lambda_{\boldsymbol{k}}^\pm \sim 1$, i.e., wave motions and the nonlinear response (the right-hand-side of (3.67)) occur on the same time scale. However, in the presence of strong stratification, when $Fr \ll 1$, the linear wave frequency is such that $\lambda_{\boldsymbol{k}}^\pm \sim Fr^{-1} \gg 1$. In this strongly stratified regime the fast dimensional time scale τ_{wave}^* for temporal variations of wave modes and the slow time scale T_{L^*/U^*}^* for the temporal variations of the vortical mode are such that $T^*/\tau_{\text{wave}}^* \gg 1$. Therefore, a clear time scale separation between the fast weakly nonlinear evolution of wave modes and the slow evolutions of the vortical mode is abundantly evident when $Fr \ll 1$, and a multiple time scale analysis may be performed (Bartello, 1995).

These results are nearly identical to those of the full Boussinesq equations. In summary, when $k_\perp = 0$ the system is in hydrostatic balance and kinetic energy is identically zero and pure inertia waves have been filtered, in agreement with numerical simulations of Waite & Bartello (2006) where it is shown that kinetic energy tends to zero with Ro.

For the linearized equations (small-amplitude motions) potential vorticity (PV) becomes $q = \zeta + Fr^2 \partial_Z b$. Expressing conservation of linear PV in Fourier space, where field variables are linear combinations of $e^{i(\boldsymbol{k}\cdot\boldsymbol{x}+\omega_{\boldsymbol{k}}t)}$, gives

$$\begin{aligned}
0 &= \omega_{\boldsymbol{k}}\left(\hat{\zeta}_{\boldsymbol{k}} + iFr^2 k_Z \hat{b}_{\boldsymbol{k}}\right),\\
&= \omega_{\boldsymbol{k}} Fr\left(Fr^{-1} k_\perp \hat{\zeta}_{\boldsymbol{k}} + ik_\perp k_Z Fr\hat{b}_{\boldsymbol{k}}\right),\\
&= \omega_{\boldsymbol{k}}^2 Fr k_\perp C_{\boldsymbol{k}}^0.
\end{aligned}$$

If $\omega_{\boldsymbol{k}} \neq 0$ then linear PV must be zero, i.e., $q = 0$. Moreover, the vortical mode energy must vanish. Similarly, if linear PV is nonzero then it must be the case that $\omega_{\boldsymbol{k}} = 0$. Therefore, eigenmodes for which $\omega_{\boldsymbol{k}} \neq 0$ possess zero linear PV and the eigenmode with frequency $\omega_{\boldsymbol{k}} = 0$ carries all linear PV. For this reason the mode associated with $\omega_{\boldsymbol{k}} = 0$ is often referred to as the PV mode. We now take note that this PV mode is a conserved quantity. These results, which hold for the reduced

equations, are precisely those for the full Boussinesq equations (Smith & Waleffe (2002), Bartello (1995)).

3.6.3 Energetics

We may consider the energy exchanges that occur as a result on nonlinear response for both vortical and wave modes. From equation (3.67) we may form the evolution of vortical and wave energies (adopting the schematic notation used by Bartello (1995)):

$$
\begin{aligned}
\partial_t |V_{\boldsymbol{k}}|^2 &= \sum_{\boldsymbol{k}=\boldsymbol{p}+\boldsymbol{q}} N_{\boldsymbol{k},\boldsymbol{p},\boldsymbol{q}}^{0,0,0} V_{\boldsymbol{k}}^{\dagger} V_{\boldsymbol{p}} V_{\boldsymbol{q}} + N_{\boldsymbol{k},\boldsymbol{p},\boldsymbol{q}}^{0,0,\pm} V_{\boldsymbol{k}}^{\dagger} V_{\boldsymbol{p}} G_{\boldsymbol{q}}^{s_q} e^{\lambda_{\boldsymbol{q}}^{\pm} t} \qquad (3.67a) \\
&+ N_{\boldsymbol{k},\boldsymbol{p},\boldsymbol{q}}^{0,\pm,\pm} V_{\boldsymbol{k}}^{\dagger} G_{\boldsymbol{p}}^{\pm} G_{\boldsymbol{q}}^{\pm} e^{(\lambda_{\boldsymbol{p}}^{\pm}+\lambda_{\boldsymbol{q}}^{\pm})t}, \\
\left(\partial_t - \lambda_{\boldsymbol{k}}^{\pm}\right) |G_{\boldsymbol{k}}^{\pm}|^2 &= N_{\boldsymbol{k},\boldsymbol{p},\boldsymbol{q}}^{\pm,0,0} G_{\boldsymbol{k}}^{\pm\dagger} V_{\boldsymbol{p}} V_{\boldsymbol{q}} e^{-\lambda_{\boldsymbol{k}}^{\pm}} + N_{\boldsymbol{k},\boldsymbol{p},\boldsymbol{q}}^{\pm,0,\pm} G_{\boldsymbol{k}}^{\pm\dagger} V_{\boldsymbol{p}} G_{\boldsymbol{q}}^{\pm} e^{(\lambda_{\boldsymbol{q}}^{\pm}-\lambda_{\boldsymbol{k}}^{\pm})t} \qquad (3.67b) \\
&+ N_{\boldsymbol{k},\boldsymbol{p},\boldsymbol{q}}^{\pm,\pm,\pm} G_{\boldsymbol{k}}^{\pm\dagger} G_{\boldsymbol{p}}^{\pm} G_{\boldsymbol{q}}^{\pm} e^{(\lambda_{\boldsymbol{p}}^{\pm}+\lambda_{\boldsymbol{q}}^{\pm}-\lambda_{\boldsymbol{k}}^{\pm})t}.
\end{aligned}
$$

From the nonlinear interaction terms the manner in which energy is transferred among triadic wavenumbers may be determined through an analysis similar to that presented by Bartello (1995).

3.7 Conclusions

We have presented an investigation into stably stratified and rapidly rotating turbulence using the asymptotically reduced NH-QG equation set valid for $Ro \ll 1$ describing geostrophically balanced flow. Such a regime is relevant to abyssal oceans (where observations indicate the presence of weak stratification) as well as planetary and stellar interiors (in regions where stratification transitions from unstable to stable). Within this parameter regime the Proudman-Taylor constraint is relaxed/broken by allowing anisotropic dynamics with vertical scales $\mathcal{O}(Ro^{-1})$ larger than horizontal scales. In this setting slow inertia-gravity waves with order-one frequencies are retained and not filtered, moreover, timescales for nonlinear eddy dynamics and anisotropic inertia-gravity waves are not asymptotically separated (see §3.2.1). Numerical simulations with wave-eddy interactions are performed where motions are induced by a stochastic injection of vertical kinetic energy; do-

ing so only provides wave-energy and any emergence of vortical mode energy must originate from wave-eddy interactions (see §3.4).

Our results reveal two regimes corresponding to strong ($Fr < 1$) and weak ($Fr \geq 1$) stratification. These regimes are primarily distinguished by the presence at strong stratification of thin horizontal turbulent layers in which energy transfer and dissipation are most active. As Fr increases up to unity, layer thickness also increases until the layers occupy the entire vertical extent of the domain. We note such layer formation is not observed for classical QG dynamics for which inertia-gravity waves are entirely absent. Evidence of layering has been previously observed in experiments of decaying purely stratified turbulence (Billant and Chomaz, 2000) and numerical studies of decaying rotating-stratified turbulence (Cambon, 2001), but not in previous studies of rapidly-rotating, strongly-stratified, forced-dissipative turbulence. Unlike the 'pancake' structures that form in stratified turbulence (Kimura and Herring, 2009), the layers here are localized and long-lived. Also, vertical shear of the horizontal velocity $\partial_z u_\perp$ is absent from the reduced equations governing the dynamics, so layer formation cannot be associated with shear instabilities like Kelvin-Helmholtz or symmetric instability. Unlike the 'staircase' layering in doubly-diffusive convection (Stellmach et al., 2011) the layers consist of thin regions of *reduced* stratification. We conjecture that their existence is related to our use of vertical velocity forcing, in the sense that other kinds of forcing may disrupt the dynamics leading to layer formation. Here, layer formation at $Fr < 1$ is associated with mixing by vertical buoyancy flux and energy conversion by vortex stretching (evident in vertical profiles in figure 3.5). Additionally, vertical profiles of stratification and RMS vertical vorticity quantify layer location and thickness.

In addition to the presence or absence of layers, the regimes are distinguished by energetics. In the strongly-stratified regime only a small percentage of the energy injection rate to vertical kinetic energy is converted to horizontal kinetic energy, and a modest amount is converted to potential energy. In the weakly-stratified regime only a small percentage of the energy injection rate to vertical kinetic energy is converted to potential energy, and a modest amount is converted to horizontal kinetic energy.

Both regimes are characterized by the emergence of a large-scale barotropic dipole (see figure 3.2). When the Reynolds number is not too large ($Re_f \leq 100$, or $Re_c \leq 2000$) system energy reaches a statistically steady state, evidence that geostrophically balanced flow is capable of establishing a direct route to dissipation. The process leading to energy saturation is attributed to a downscale transfer of kinetic energy within the barotropic mode, which balances the injection of barotropic energy by baroclinic motions. Another distinct trait of the flows studied here is that three-dimensional baroclinic motions interact in such a way as to inject energy into the largest barotropic scales; therefore, the accumulation of energy at the largest scales in the barotropic mode is not the result of an upscale transfer within the barotropic mode.

Appendix A

Tables

Table A.1: Values of α for the half-width power-law fits, $L = \beta(RaE^{4/3} - Ra_cE^{4/3})^\alpha$, for each of the three intervals identified in figure 2.8(a).

	$Ra_cE^{4/3} < RaE^{4/3} \lesssim 20$	$20 \lesssim RaE^{4/3} \lesssim 55$	$55 \lesssim RaE^{4/3} \leq 70$
Equispaced	-0.7052	-0.2225	-4.6102
TBL	-1.2072	-0.2849	-5.8706

Table A.2: Values of α for the the power-law fits for velocity scale, $U = \beta(RaE^{4/3} - Ra_cE^{4/3})^\alpha$, for each of the three intervals identified in figure 2.8(a).

	$Ra_cE^{4/3} < RaE^{4/3} \lesssim 20$	$20 \lesssim RaE^{4/3} \lesssim 55$	$55 \lesssim RaE^{4/3} \leq 70$
Equispaced	0.7230	0.2601	4.4897
TBL	1.2323	0.2376	5.2038

Appendix B

Derivation of the Reduced NH-QG Equations

As mentioned above a detailed account of the asymptotic derivation of the reduced non-hydrostatic quasi-geostrophic (NH-QG) equations is given. Introduction of the multiple scale expansions (3.23) into the Boussinesq equation (3.6) with $\varepsilon \equiv Ro \ll 1$ gives the *multi-scale* equation set

$$
\left(D_t + \varepsilon^2 \partial_T + \varepsilon w \partial_Z \right) \boldsymbol{u} + \varepsilon^{-1} \hat{\boldsymbol{z}} \times \boldsymbol{u} = -Eu \left(\nabla + \hat{\boldsymbol{z}} \varepsilon \partial_Z \right) p + b \hat{\boldsymbol{z}} \tag{B.1}
$$

$$
+ \frac{1}{Re} \left(\nabla + \hat{\boldsymbol{z}} \varepsilon \partial_Z \right)^2 \boldsymbol{u},
$$

$$
\left(D_t + \varepsilon^2 \partial_T + \varepsilon w \partial_Z \right) b + \frac{w}{Fr^2} S = \frac{1}{\sigma Re} \left(\nabla + \hat{\boldsymbol{z}} \varepsilon \partial_Z \right)^2 b, \tag{B.2}
$$

$$
\nabla \cdot \boldsymbol{u} + \varepsilon \partial_Z w = 0. \tag{B.3}
$$

Decomposing each fluid variable in to mean and fluctuating components according to (3.24) and (3.25) and averaging the above multi-scale equations produces the mean equations

$$
\varepsilon^2 \partial_T \overline{\boldsymbol{u}} + \varepsilon \partial_Z \left(\overline{w' \boldsymbol{u}'} \right) + \varepsilon^{-1} \hat{\boldsymbol{z}} \times \overline{\boldsymbol{u}} = \left(\overline{b} - Eu \varepsilon \partial_Z \overline{p} \right) \hat{\boldsymbol{z}} + \frac{\varepsilon^2}{Re} \partial_Z^2 \overline{\boldsymbol{u}}, \tag{B.4}
$$

$$
\varepsilon^2 \partial_T \overline{b} + \varepsilon \partial_Z \left(\overline{w' b'} \right) = \frac{\varepsilon^2}{\sigma Re} \partial_Z^2 \overline{b}, \tag{B.5}
$$

$$
\partial_Z \overline{w} = 0. \tag{B.6}
$$

where the the continuity equation (B.3) is used in re-expressing the nonlinear terms in (B.4)–(B.6). Without loss of generality the mean continuity equation gives $\overline{w} \equiv 0$ such that $\overline{\boldsymbol{u}} = (\overline{\boldsymbol{u}}_\perp, 0)$.

Equations governing fluctuating quantities are obtained by subtracting (B.4)–(B.6) from

(B.1)– (B.3), giving

$$
\begin{aligned}
\left(D_t + \varepsilon^2 \partial_T + \varepsilon w \partial_Z\right) \boldsymbol{u}' \quad &+ \quad \varepsilon\left(w' \partial_Z \overline{\boldsymbol{u}} - \partial_Z\left(\overline{w'\boldsymbol{u}'}\right)\right) + \varepsilon^{-1} \hat{\boldsymbol{z}} \times \boldsymbol{u}' \\
&= \quad -Eu\left(\nabla + \hat{\boldsymbol{z}} \varepsilon \partial_Z\right) p' + b'\hat{\boldsymbol{z}} \\
&+ \quad \frac{1}{Re}\left(\nabla + \hat{\boldsymbol{z}}\varepsilon\partial_Z\right)^2 \boldsymbol{u}',
\end{aligned} \tag{B.7}
$$

$$
\begin{aligned}
\left(D_t + \varepsilon^2 \partial_T + \varepsilon w \partial_Z\right) b' \quad &+ \quad \varepsilon\left(w'\partial_Z \overline{b} - \partial_Z\left(\overline{w'b'}\right)\right) + \frac{w'S}{Fr^2} \\
&= \quad \frac{1}{\sigma Re}\left(\nabla + \hat{\boldsymbol{z}}\varepsilon\partial_Z\right)^2 b',
\end{aligned} \tag{B.8}
$$

$$
\nabla \cdot \boldsymbol{u}' + \varepsilon \partial_Z w' = 0. \tag{B.9}
$$

Simplification occurs upon introducing asymptotic series expansions (3.22) into the equations governing mean and fluctuating quantities, (B.4)–(B.6) and (B.7)–(B.9). At $\mathcal{O}(\varepsilon^{-2})$ in (B.4) and (B.7) we must have $\boldsymbol{u}_{-1} \equiv 0$. Note the horizontal component of (B.4) at order $\mathcal{O}(\varepsilon^{-2})$ yields $\overline{\boldsymbol{u}}_{\perp,-1} = 0$ and thus $\overline{\boldsymbol{u}}_{-1} = 0$, since $\overline{w} \equiv 0$ by (B.6). Thus, equations (B.7)–(B.9) are solely responsible for describing the leading-order fluid motions. The vertical component of (B.4) requires $Eu \sim \varepsilon^{-1}$ for mean hydrostatic balance (3.27). All non-dimensional parameters are now determined upon setting $Fr = \mathcal{O}(1)$ as discussed in section 3.2.1 for the non-hydrostatic regime, restricting $Re = o(\varepsilon^{-2})$ as discussed in section 3.2, and letting $\sigma = \mathcal{O}(1)$.

B.0.1   Perturbation theory and solvability

The end result of the multiple scale asymptotic approach is a sequence of linear partial differential equations (PDEs) to be solved order-by-order in ε. Equation (B.7) at $\mathcal{O}(\varepsilon^{-2})$ gives $\nabla p'_{-1} = 0$ permitting the choice $p'_{-1} \equiv 0$. From equation (B.8) we find that the variable $b'_{-1} \equiv 0$ satisfies the advection-diffusion equation

$$
D_t^0 b'_{-1} = \frac{1}{\sigma Re_f} \nabla^2 b'_{-1} \tag{B.10}
$$

where $D_t^0 = \partial_t + \boldsymbol{u}'_0 \cdot \nabla$. The variance over $\mathcal{O}(L^*)$ spatial scales satisfies $\lim_{t\to\infty} \overline{\left(b'_{-1}\right)^2} = 0$. Thus, we set $b'_{-1} \equiv 0$.

Equation (B.7) at $\mathcal{O}(\varepsilon^{-1})$ and the continuity equation (B.9) at $\mathcal{O}(1)$ give

$$\hat{\boldsymbol{z}} \times \boldsymbol{u}'_0 + \nabla p'_0 \;=\; 0, \tag{B.11}$$

$$\nabla \cdot \boldsymbol{u}'_0 \;=\; 0, \tag{B.12}$$

while equations (B.7) at $\mathcal{O}(1)$ and (B.9) at $\mathcal{O}(\varepsilon)$ yield

$$\hat{\boldsymbol{z}} \times \boldsymbol{u}'_1 + \nabla p'_1 \;=\; -D_t^0 \boldsymbol{u}'_0 + \left(-\partial_Z p'_0 + b'_0\right)\hat{\boldsymbol{z}} + \frac{1}{Re}\nabla^2 \boldsymbol{u}'_0, \tag{B.13}$$

$$\nabla \cdot \boldsymbol{u}_1 \;=\; -\partial_Z w'_0. \tag{B.14}$$

Equation (B.5) at $\mathcal{O}(\varepsilon)$ gives

$$\partial_T \bar{b}_0 + \partial_Z \left(\overline{w'_0 b'_0}\right) = \frac{1}{\sigma Re}\partial_Z^2 \bar{b}_0. \tag{B.15}$$

At $\mathcal{O}(1)$ equation (B.8) gives

$$D_t^0 b'_0 + w'_0 \left(\partial_Z \bar{b}_{-1} + \frac{S}{Fr^2}\right) = \frac{1}{\sigma Re}\nabla^2 b'_0. \tag{B.16}$$

Equations (B.11) through (B.16) represent the closed reduced system. Equations (B.11)-(B.14) constitute a sequence of linear PDEs in powers of ε and (B.11) and (B.12) may be expressed as

$$\mathcal{L}_{geo}\boldsymbol{v}_0 = \boldsymbol{0}, \tag{B.17}$$

where $\boldsymbol{v}'_0 = (\boldsymbol{u}'_0, p'_0)^T$ and $\mathcal{L}_{geo}$ is the geostrophic operator defined as

$$\mathcal{L}_{geo} \equiv \begin{bmatrix} 0 & -1 & 0 & \partial_x \\ 1 & 0 & 0 & \partial_y \\ 0 & 0 & 0 & \partial_z \\ \partial_x & \partial_y & \partial_z & 0 \end{bmatrix}. \tag{B.18}$$

At subsequent orders the systems to be solved are similar to (B.17) and are of the form

$$\mathcal{L}_{geo}\boldsymbol{v}_i = \boldsymbol{r}_i. \tag{B.19}$$

The next system in the sequence for $\boldsymbol{v}_1 = (u_1, v_1, w_1, p_1)^T$ has $\boldsymbol{r}_1$ given by equations (B.13)–(B.14) and may be written as

$$\boldsymbol{r}_1 = \begin{bmatrix} r_{u,1} \\ r_{v,1} \\ r_{w,1} \\ r_{p,1} \end{bmatrix} = \begin{bmatrix} -D_t^0 u_0 + Re_f^{-1} \nabla_\perp^2 u_0 \\ -D_t^0 v_0 + Re_f^{-1} \nabla_\perp^2 v_0 \\ -D_t^0 w_0 - \partial_Z p_0 + b_0' + Re_f^{-1} \nabla_\perp^2 w_0 \\ -\partial_Z w_0 \end{bmatrix}. \tag{B.20}$$

Note that $\boldsymbol{r}_1$ is determined from solutions to the system at previous asymptotic order. To ensure solvability of the linear system (B.19) conditions on $\boldsymbol{r}_i$ must be determined for solutions $\boldsymbol{v}_i$ to remain bounded in space and time which demands $\boldsymbol{r}_i$ be orthogonal to the null-space (solutions $\boldsymbol{v}^\dagger$ to $\mathcal{L}_{geo}\boldsymbol{v}^\dagger{=}0$) of the adjoint operator $\mathcal{L}_{geo}^\dagger$ defined as

$$\langle \boldsymbol{v}^\dagger, \mathcal{L}_{geo}\boldsymbol{v} \rangle = \langle \mathcal{L}_{geo}^\dagger \boldsymbol{v}^\dagger, \boldsymbol{v} \rangle. \tag{B.21}$$

where the inner-product is defined as $\langle \boldsymbol{v}^\dagger, \boldsymbol{u} \rangle \equiv \int \boldsymbol{v}^\dagger \boldsymbol{u} \, \mathrm{d}x \mathrm{d}y \mathrm{d}z$. The procedure to determine $\mathcal{L}_{geo}^\dagger$ is straightforward: start with equation (B.21) and integrate by parts until all derivatives no longer operate on $\boldsymbol{v}$ and operate exclusively on $\boldsymbol{v}^\dagger$, that is,

$$\begin{aligned} \langle \boldsymbol{v}^\dagger, \mathcal{L}_{geo}\boldsymbol{v} \rangle &= \int \left[u^\dagger(\partial_x p - v) + v^\dagger(\partial_y p + u) + w^\dagger \partial_z p + p^\dagger(\nabla \cdot \boldsymbol{u}) \right] d\boldsymbol{x} \\ &= -\int \left[(\partial_x p^\dagger - v^\dagger)u + (\partial_y p^\dagger + u^\dagger)v + (\partial_z p^\dagger)w + (\nabla \cdot \boldsymbol{u}^\dagger)p \right] d\boldsymbol{x} \\ &= \langle \mathcal{L}_{geo}^\dagger \boldsymbol{v}^\dagger, \boldsymbol{v} \rangle. \end{aligned}$$

The geostrophic operator is found to be skew-adjoint, i.e., $\mathcal{L}_{geo}^\dagger = -\mathcal{L}_{geo}$, therefore the null-space of the adjoint operator is related to solutions of homogeneous problem (B.17) by $\boldsymbol{v}^\dagger = -\boldsymbol{v}_0$. Or-

thogonality of $\boldsymbol{v}^\dagger$ and $\boldsymbol{r}_1$ follows

$$
\begin{aligned}
0 &= \langle \boldsymbol{v}^\dagger, \boldsymbol{r}_1 \rangle, \\
&= \int \left[u^\dagger r_{u,1} + v^\dagger r_{v,1} + w^\dagger r_{w,1} + p^\dagger r_{p,1} \right] \mathrm{d}x\mathrm{d}y\mathrm{d}z, \\
&= \int \left[(\partial_y \psi) r_{u,1} - (\partial_x \psi) r_{v,1} - w r_{w,1} - \psi r_{p,1} \right] \mathrm{d}x\mathrm{d}y\mathrm{d}z, \\
&= \int \left[\psi \left(\partial_x r_{r,1} - \partial_y r_{u,1} - r_{p,1} \right) - w r_{w,1} \right] \mathrm{d}x\mathrm{d}y\mathrm{d}z, \\
&= \int \psi \left[\int (\partial_x r_{v,1} - \partial_y r_{u,1} - r_{p,1}) \, \mathrm{d}z \right] \mathrm{d}x\mathrm{d}y - \int w \left[\int r_{w,1} \mathrm{d}z \right] \mathrm{d}x\mathrm{d}y,
\end{aligned}
$$

using integration by parts, periodic boundary conditions, and the geostrophic streamfunction ($p_0^\dagger = -p_0 = -\psi_0$). With ψ and w independent of z the above integrals vanish provided the following solvability conditions hold

$$
\int (\partial_x r_{v,1} - \partial_y r_{u,1} - r_{p,1}) \, \mathrm{d}z = 0, \quad \int r_{w,1} \mathrm{d}z = 0. \tag{B.22}
$$

Conditions in (B.22) provide equations governing leading-order vertical vorticity ζ_0 and velocity w_0. Coupling between vertical velocity and buoyancy occurs through the z-averaged fluctuating variable defined as

$$
b' \equiv \langle b_0' \rangle_z = \lim_{\lambda \to \infty} \frac{1}{\lambda} \int_\lambda b_0' \mathrm{d}z, \tag{B.23}
$$

as required by the second integral condition in (B.22). From equation (B.8), we find that rapid variations $b_0' - \langle b_0' \rangle_z$ on the Taylor-Proudman scale satisfies an advection-diffusion equation. Thus, if unforced, its variance decreases monotonically to zero and $b_0' - \langle b_0' \rangle_z \equiv 0$. Fluctuating buoyancy b', therefore, satisfies Taylor-Proudman constraints on vertical scales L^*. Solutions to the leading-order geostrophic balance (B.17) may be written in toroidal-poloidal form Chandrasekhar (1961); Julien et al. (2006)

$$
\boldsymbol{u}_0' = -\nabla \times \psi_0 \hat{\boldsymbol{z}} + w_0' \hat{\boldsymbol{z}}, \tag{B.24}
$$

Due to Taylor-Proudman constraints we may write $D_t^0 = \partial_t + \boldsymbol{u}_{0\perp}' \cdot \nabla_\perp = \partial_x \psi_0 \partial_y - \partial_y \psi_0 \partial_x \equiv J[\psi_0, \cdot]$. The reduced equations become those given in (3.30).

We note that vertical velocity forcing or buoyancy forcing may be included from the onset of this derivation. The condition that $b'_{-1} \equiv 0$ indicates that forcing equation (B.8) at $\mathcal{O}(\varepsilon^{-1})$ should be absent. Moreover, similar to previous studies where stochastic white noise forcing is used, any such forcing present in (B.1)–(B.3) vanishes upon horizontal averaging over small spatial scales and fast temporal scales. Hence, stochastic white noise forcing necessarily occurs through the fluctuating equations.

Appendix C

Code Validation

Before running numerical simulations of stably stratified and rapidly rotating flow some validation of the numerical scheme is in order. For numerical simulations of rapidly rotating Rayleigh-Bénard convection a third-order mixed implicit/explicit Runge-Kutta scheme was used for numerical time-stepping. In that framework the domain was horizontally periodic, and therefore used Fourier expansions in the horizontal directions. Given the impenetrable vertical boundary conditions for this problem Chebychev expansions are used to expand fluid variables in the $\hat{z}$-direction. The stable layer study makes use of the same time-stepper, however, in this framework the aim is to perform numerical simulations in a triply-periodic domain. This requires the use of subroutines not used or validated for simulations of the reduced NH-QG equations in the stable layer configuration, we take a moment to show the numerical scheme laid out by Spalart et al. (1991a) and used by Sprague et al. (2006) for the Rayleigh-Bénard problem gives valid results when applied to a triply-periodic stably stratified fluid. It is noted that no modification is made to the numerical scheme itself, but only calls to routines responsible for computing discrete Fourier transforms. Validation is accomplished by imposing initial conditions at a single-wavenumber for fixed Re, Fr and $\sigma = 1$ and allowing the simulation to decay. Numerical solutions are then compared to analytic solutions of the linearized NH-QG equations. Once the linear problem is validated, nonlinear terms are included to ensure that single-mode solutions behave correctly.

In what follows we make use of the toroidal-poloidal decomposition

$$\boldsymbol{u}_0 = -\nabla_\perp \times \psi_0 \hat{\boldsymbol{z}} - \nabla_\perp \times \nabla_\perp \times \phi_0 \hat{\boldsymbol{z}} \tag{C.1}$$

where $\nabla_\perp = (\partial_x, \partial_y, 0)$ and which automatically satisfies leading-order geostrophy (additionally, numerical scheme is evolved using this decomposition). The linearized and unforced equations in terms of ψ_0, ϕ_0, and b_0 become

$$\partial_t \nabla_\perp^2 \psi_0 - \partial_Z \nabla_\perp^2 \phi_0 = \frac{1}{Re} \nabla_\perp^4 \psi_0 \tag{C.2a}$$

$$\partial_t \nabla_\perp^2 \phi_0 + \partial_Z \psi_0 = \frac{b_0}{Fr^2} + \frac{1}{Re} \nabla_\perp^4 \phi_0 \tag{C.2b}$$

$$\partial_t b_0 + \nabla_\perp^2 \phi_0 = \frac{1}{\sigma Re} \nabla_\perp^2 b_0 \tag{C.2c}$$

where $w_0 = \nabla_\perp^2 \phi_0$, buoyancy has been scaled such that $b_0 \to b_0/Fr^2$, and $S(Z) = 1$. The domain is triply-periodic (i.e., $f(\boldsymbol{x} + L_i \boldsymbol{e}_i) = f(\boldsymbol{x})$, where L_i is the length of periodicity and $\boldsymbol{e}_i$ is the ith unit vector for $i = 1, 2$ and 3) so that a fluid variable f is expressed as Fourier series

$$f(\boldsymbol{x}, t) = \sum_{\boldsymbol{k}} \hat{f}_{\boldsymbol{k}}(t) e^{i \boldsymbol{k} \cdot \boldsymbol{x}} \tag{C.3}$$

Wavenumbers take the form

$$\boldsymbol{k} = (\boldsymbol{k}_\perp, k_Z) = (2\pi n_x/L, 2\pi n_y/L, 2\pi n_Z), \tag{C.4}$$

where $\boldsymbol{n} = (n_x, n_y, n_Z) \in \mathbb{Z}^3$. For real-valued solutions we require $\hat{f}_{-\boldsymbol{k}} = \overline{\hat{f}_{\boldsymbol{k}}}$, where the overbar denotes complex conjugation. Substituting Fourier series in the linear system (C.2) yields a linear system of first-order differential equations. A given wavenumber $\boldsymbol{k} = (\boldsymbol{k}_\perp, k_Z)$, where $\boldsymbol{k}_\perp = (k_x, k_y)$, will satisfy one of three different systems depending on which set $\boldsymbol{k}$ belongs to: the barotropic set where $k_Z = 0$, $k_\perp \neq 0$, the baroclinic set where $k_Z \neq 0$, $k_\perp \neq 0$, and the horizontally averaged set where $k_\perp = 0$. This is nearly identical to the analysis by Bartello (1995). Solutions to the linear systems can be expressed as a linear combination of eigenvectors $\boldsymbol{\xi}_i$ with associated eigenvalues λ_i and are of the form

$$\hat{\boldsymbol{f}}_{\boldsymbol{k}}(t) = \begin{pmatrix} \hat{\psi}_{0,\boldsymbol{k}}(t) \\ \hat{\phi}_{0,\boldsymbol{k}}(t) \\ \hat{b}_{0,\boldsymbol{k}}(t) \end{pmatrix} = \sum_{i=1}^{3} \alpha_i \boldsymbol{\xi}_i e^{\lambda_i t} \tag{C.5}$$

Since the code is pseudospectral and performs real fast Fourier transforms (real FFTs in terms of

sine and cosine coefficients), the eigenvectors $\boldsymbol{\xi}_i$ must be re-expressed to give cosine sine coefficients. Before giving the eigenvectors in real form the following outlines the three linear systems that a single-wavenumber may satisfy. For simplicity only the case where $\sigma = 1$ is considered.

C.1   Case I: vertical variability: $k_\perp = 0$, $k_Z \neq 0$

When $k_Z \neq 0$ and $k_\perp = 0$ the Fourier coefficients at wavenumber $\boldsymbol{k}$ satisfy the system

$$\partial_t \begin{pmatrix} 0 \\ 0 \\ \hat{b} \end{pmatrix} = \begin{pmatrix} 0 & 0 & 0 \\ ik_Z & 0 & \frac{-1}{Fr^2} \\ 0 & 0 & 0 \end{pmatrix} \begin{pmatrix} \hat{\psi} \\ \hat{\phi} \\ \hat{b} \end{pmatrix}. \tag{C.6}$$

The single eigenvalue $\lambda_{1,2,3} = 0$ has algebraic multiplicity three and geometric multiplicity two. The linearly independent eigenvectors corresponding to the two-dimensional eigenspace are

$$\boldsymbol{\xi}_{1,2} = \begin{pmatrix} \hat{\psi} \\ 0 \\ iFr^2 k_Z \hat{\psi} \end{pmatrix}_1, \begin{pmatrix} 0 \\ \hat{\phi} \\ 0 \end{pmatrix}_2. \tag{C.7}$$

Solutions to this system represent a state of hydrostatic balance in which $\boldsymbol{u}_0 = (-\partial_y \psi_0, \partial_x \psi_0, \nabla_\perp^2 \phi) = \boldsymbol{0}$ and $\partial_Z \psi = b/Fr^2$.

C.2   Case II: barotropic mode: $k_\perp \neq 0$, $k_Z = 0$

When $k_Z = 0$, the Fourier coefficients at wavenumber $\boldsymbol{k}$ satisfy the system

$$\partial_t \begin{pmatrix} \hat{\psi} \\ \hat{\phi} \\ \hat{b} \end{pmatrix} = \begin{pmatrix} -\frac{k_\perp^2}{Re} & 0 & 0 \\ 0 & -\frac{k_\perp^2}{Re} & \frac{-1}{Fr^2 k_\perp^2} \\ 0 & k_\perp^2 & -\frac{k_\perp^2}{Re} \end{pmatrix} \begin{pmatrix} \hat{\psi} \\ \hat{\phi} \\ \hat{b} \end{pmatrix}. \tag{C.8}$$

with the following eigenvalues and eigenvectors:

$$\lambda_1 = -\frac{k_\perp^2}{Re} \tag{C.9}$$

$$\lambda_{2,3} = -\frac{k_\perp^2}{Re} \pm i\frac{1}{Fr} \tag{C.10}$$

$$\boldsymbol{\xi}_{1,2,3} = \begin{pmatrix} \hat{\psi} \\ 0 \\ 0 \end{pmatrix}_1, \begin{pmatrix} 0 \\ \hat{\phi} \\ \mp i\hat{\phi}Frk_\perp^2 \end{pmatrix}_{2,3}. \tag{C.11}$$

C.3 Case III: baroclinic mode: $k_\perp \neq 0$, $k_Z \neq 0$

When both $k_\perp \neq 0$ and $k_Z \neq 0$ the Fourier coefficients now satisfy

$$\partial_t \begin{pmatrix} \hat{\psi} \\ \hat{\phi} \\ \hat{b} \end{pmatrix} = \begin{pmatrix} -\frac{k_\perp^2}{Re} & ik_Z & 0 \\ \frac{ik_Z}{k_\perp^2} & -\frac{k_\perp^2}{Re} & \frac{-1}{Fr^2 k_\perp^2} \\ 0 & k_\perp^2 & -\frac{k_\perp^2}{Re} \end{pmatrix} \begin{pmatrix} \hat{\psi} \\ \hat{\phi} \\ \hat{b} \end{pmatrix}. \tag{C.12}$$

The eigenvalues and eigenvectors of this linear system are

$$\lambda_1 = -\frac{k_\perp^2}{Re} \tag{C.13}$$

$$\lambda_{2,3} = -\frac{k_\perp^2}{Re} \pm i\sqrt{\frac{1}{Fr^2} + \frac{k_Z^2}{k_\perp^2}} \tag{C.14}$$

$$\boldsymbol{\xi}_{1,2,3} = \begin{pmatrix} \hat{\psi} \\ 0 \\ iFr^2 k_Z\hat{\psi} \end{pmatrix}_1, \begin{pmatrix} \hat{\psi} \\ \pm\sqrt{\frac{1}{Fr^2} + \frac{k_Z^2}{k_\perp^2}}k_Z^{-1}\hat{\psi} \\ -ik_\perp^2 k_Z^{-1}\hat{\psi} \end{pmatrix}_{2,3}. \tag{C.15}$$

These systems provide three eigenvalues and three linearly independent eigenvectors (with exception of the case where $k_\perp = 0$). For the first and second cases the first of eigen pairs $(\boldsymbol{\xi}_1, \lambda_1)$ has zero temporal frequency and corresponds to the PV mode, while the remaining eigen pairs pairs correspond to wave-modes. Any vector belonging to $\mathbb{C}^3$ can be expressed as a linear combination of eigenvectors as in equation (C.5) yielding generalized time-dependent solutions to the appropriate linear system.

C.4   Code compatibility

Again, since the code works in spectral space and performs real FFTs the eigenvectors above must be decomposed to give cosine coefficients $\boldsymbol{a(k)} = \hat{\boldsymbol{f}}_{\boldsymbol{k}} + \overline{\hat{\boldsymbol{f}}}_{\boldsymbol{k}} = 2\mathrm{Re}(\hat{\boldsymbol{f}}_{\boldsymbol{k}})$ and sine coefficients $\boldsymbol{b(k)} = i(\hat{\boldsymbol{f}}_{\boldsymbol{k}} - \overline{\hat{\boldsymbol{f}}}_{\boldsymbol{k}}) = -2\mathrm{Im}(\hat{\boldsymbol{f}}_{\boldsymbol{k}})$. In physical space the single-wavenumber solution to a real-valued field variable $f(\boldsymbol{x}, t)$ takes the following form:

$$f(\boldsymbol{x}, t) = \overline{\hat{f}}_{\boldsymbol{k}} e^{-i\boldsymbol{k}\cdot\boldsymbol{x}} + \hat{f}_{\boldsymbol{k}} e^{i\boldsymbol{n}\cdot\boldsymbol{x}} \tag{C.16}$$

$$= 2\mathrm{Re}(\hat{f}_{\boldsymbol{k}})\cos(\boldsymbol{k}\cdot\boldsymbol{x}) - 2\mathrm{Im}(\hat{f}_n)\sin(\boldsymbol{k}\cdot\boldsymbol{x}) \tag{C.17}$$

Therefore, the evolution of the Fourier coefficients of a real-valued single-wavenumber solution is determined by

$$2\mathrm{Re}(\hat{\boldsymbol{f}}_{\boldsymbol{k}}(t)) = 2\mathrm{Re}(\sum_{i=1}^{3}\alpha_i\boldsymbol{\xi}_i e^{\lambda_i t})$$

$$= (\alpha_1\boldsymbol{a}_1 + (\alpha_2\boldsymbol{a}_2 + \alpha_3\boldsymbol{a}_3)\cos(\delta t) + (\alpha_2\boldsymbol{b}_2 - \alpha_3\boldsymbol{b}_3)\sin(\delta t))\exp\left(\frac{-k_\perp^2}{Re}t\right), \tag{C.18}$$

$$-2\mathrm{Im}(\hat{\boldsymbol{f}}_{\boldsymbol{k}}(t)) = 2\mathrm{Im}(\sum_{i=1}^{3}\alpha_i\boldsymbol{\xi}_i e^{\lambda_i t})$$

$$= (\alpha_1\boldsymbol{b}_1 + (\alpha_2\boldsymbol{b}_2 + \alpha_3\boldsymbol{b}_3)\cos(\delta t) + (\alpha_3\boldsymbol{a}_3 - \alpha_2\boldsymbol{a}_2)\sin(\delta t))\exp\left(\frac{-k_\perp^2}{Re}t\right), \tag{C.19}$$

where $\delta = \sqrt{1/Fr^2 + k_Z^2/k_\perp^2}$, $\boldsymbol{a}_i = 2\mathrm{Re}(\boldsymbol{\xi}_i)$, and $\boldsymbol{b}_i = -2\mathrm{Im}(\boldsymbol{\xi}_i)$. In general $\boldsymbol{\alpha} \in \mathbb{C}^3$ and are determined by initial conditions, however, since the current aim is to validate the code, without loss of generality, we take $\boldsymbol{\alpha} \in \mathbb{R}^3$ in the above. In particular, we focus on the special cases when $\boldsymbol{\alpha} = \boldsymbol{e}_i$, for $i = 1, 2, 3$. For reference, the real form of the eigenvectors are summarized below where Fourier coefficients are decomposed into real and imaginary parts as $\hat{f} = \hat{f}_r + i\hat{f}_i$.

C.5   Case II: barotropic mode: $k_\perp \neq 0$, $k_Z = 0$

$$\boldsymbol{a}_1(\boldsymbol{k}) = \begin{pmatrix} 2\hat{\psi}_r \\ 0 \\ 0 \end{pmatrix} \qquad \boldsymbol{b}_1(\boldsymbol{k}) = \begin{pmatrix} -2\hat{\psi}_i \\ 0 \\ 0 \end{pmatrix} \tag{C.20}$$

$$\boldsymbol{a}_2(\boldsymbol{k}) = \begin{pmatrix} 0 \\ 2\hat{\phi}_r \\ 2\hat{\phi}_i Fr k_\perp^2 \end{pmatrix} \qquad \boldsymbol{b}_2(\boldsymbol{k}) = \begin{pmatrix} 0 \\ -2\hat{\phi}_i \\ 2\hat{\phi}_r Fr k_\perp^2 \end{pmatrix} \tag{C.21}$$

$$\boldsymbol{a}_3(\boldsymbol{k}) = \begin{pmatrix} 0 \\ 2\hat{\phi}_r \\ -2\hat{\phi}_i Fr k_\perp^2 \end{pmatrix} \qquad \boldsymbol{b}_3(\boldsymbol{k}) = \begin{pmatrix} 0 \\ -2\hat{\phi}_i \\ -2\hat{\phi}_r Fr k_\perp^2 \end{pmatrix} \tag{C.22}$$

C.6   Case III: baroclinic mode: $k_\perp \neq 0$, $k_Z \neq 0$

$$\boldsymbol{a}_1(\boldsymbol{k}) = \begin{pmatrix} 2\hat{\psi}_r \\ 0 \\ -2Fr^2 k_Z \hat{\psi}_i \end{pmatrix} \boldsymbol{b}_1(\boldsymbol{k}) = \begin{pmatrix} -2\hat{\psi}_i \\ 0 \\ -2Fr^2 k_Z \hat{\psi}_r \end{pmatrix} \tag{C.23}$$

$$\boldsymbol{a}_2(\boldsymbol{k}) = \begin{pmatrix} 2\hat{\psi}_r \\ 2\delta k_Z^{-1}\hat{\psi}_r \\ 2k_\perp^2 k_Z^{-1}\hat{\psi}_i \end{pmatrix} \qquad \boldsymbol{b}_2(\boldsymbol{k}) = \begin{pmatrix} -2\hat{\psi}_i \\ -2\delta k_Z^{-1}\hat{\psi}_i \\ 2k_\perp^2 k_Z^{-1}\hat{\psi}_r \end{pmatrix} \tag{C.24}$$

$$\boldsymbol{a}_3(\boldsymbol{k}) = \begin{pmatrix} 2\hat{\psi}_r \\ -2\delta k_Z^{-1}\hat{\psi}_r \\ 2k_\perp^2 k_Z^{-1}\hat{\psi}_i \end{pmatrix} \qquad \boldsymbol{b}_3(\boldsymbol{k}) = \begin{pmatrix} -2\hat{\psi}_i \\ 2\delta k_Z^{-1}\hat{\psi}_i \\ 2k_\perp^2 k_Z^{-1}\hat{\psi}_r \end{pmatrix} \tag{C.25}$$

C.7 Validation examples for the barotropic mode (case II)

To illustrate the process of code validation we consider the barotropic case ($k_\perp \neq 0$ and $k_Z = 0$). Furthermore, the linear evolution of each eigen-mode is considered by setting $\boldsymbol{\alpha} = \boldsymbol{e}_i$, for $i = 1, 2, 3$ and validating separately. When $\boldsymbol{\alpha} = \boldsymbol{e}_1$, the Fourier coefficients evolve according to (C.18) and (C.19) with eigenvalue $\lambda_1 = -k_\perp^2/Re$, and are given by the cosine and sine coefficients

$$\boldsymbol{a}_1 \exp\left(\frac{-k_\perp^2}{Re}t\right) = \begin{pmatrix} 2\hat{\psi}_r \\ 0 \\ 0 \end{pmatrix} \exp\left(\frac{-k_\perp^2}{Re}t\right), \tag{C.26}$$

$$\boldsymbol{b}_1 \exp\left(\frac{-k_\perp^2}{Re}t\right) = \begin{pmatrix} -2\hat{\psi}_i \\ 0 \\ 0 \end{pmatrix} \exp\left(\frac{-k_\perp^2}{Re}t\right), \tag{C.27}$$

respectively. When provided an initial conditions the the code evolves correctly and tracks the analytic solutions as illustrated in figure C.1 (dashed lines are solutions from the code and solid lines are analytic solutions outlined above).

Figure C.1: Barotropic solutions corresponding to the parameters $Re = 5$, $Fr = .01$, $(kx, ky, kz) = 2\pi(1, 1, 0)$ and where $\boldsymbol{\alpha} = \boldsymbol{e}_1$ corresponding to the vortical mode.

Similar results are obtained when one sets $\boldsymbol{\alpha} = \boldsymbol{e}_2$. The associated eigenvalue is now $\lambda_{2,3} =$

$-k_\perp^2/Re + i/Fr$ and the evolution of cosine and sine coefficients, respectively, are given by:

$$(\boldsymbol{a}_2 \cos(\delta t) + \boldsymbol{b}_2 \sin(\delta t)) \exp\left(\frac{-k_\perp^2}{Re}t\right) = 2\begin{pmatrix} 0 \\ |\hat{\phi}| \cos(t/Fr - \theta_1) \\ Frk_\perp^2|\hat{\phi}| \cos(t/Fr - \theta_2) \end{pmatrix} \exp\left(\frac{-k_\perp^2}{Re}t\right)$$

$$(\boldsymbol{b}_2 \cos(\delta t) - \boldsymbol{a}_2 \sin(\delta t)) \exp\left(\frac{-k_\perp^2}{Re}t\right) = 2\begin{pmatrix} 0 \\ |\hat{\phi}| \cos(t/Fr + \theta_3) \\ Frk_\perp^2|\hat{\phi}| \cos(t/Fr + \theta_4) \end{pmatrix} \exp\left(\frac{-k_\perp^2}{Re}t\right)$$

where $|\hat{\phi}| = \sqrt{\hat{\phi}_r^2 + \hat{\phi}_i^2}$, $\theta_1 = \tan^{-1}(-\hat{\phi}_i/\hat{\phi}_r)$, $\theta_2 = \tan^{-1}(\hat{\phi}_r/\hat{\phi}_i)$, $\theta_3 = \tan^{-1}(-\hat{\phi}_r/\hat{\phi}_i)$, and $\theta_4 = \tan^{-1}(\hat{\phi}_i/\hat{\phi}_r)$. When provided the initial conditions the code correctly tracks the analytic solutions
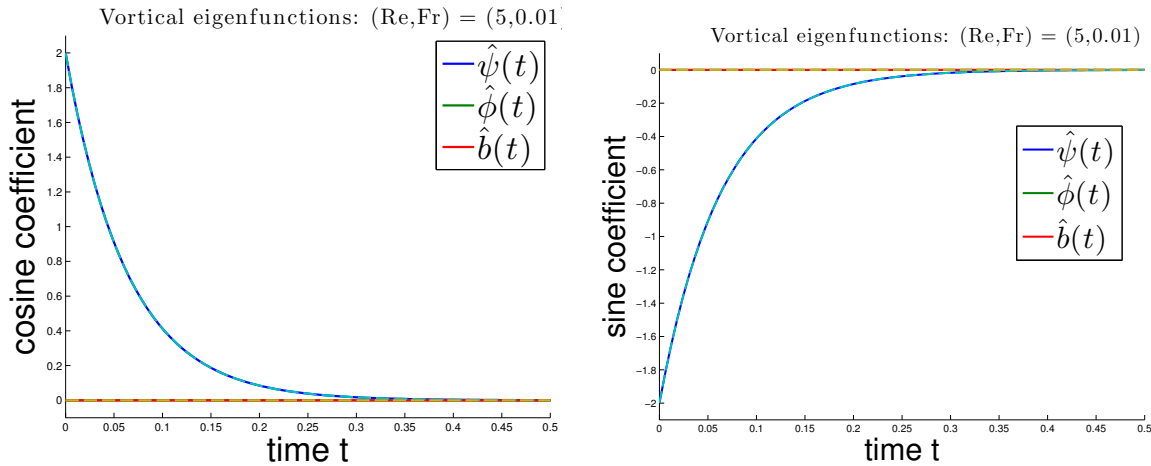

Figure C.2: Barotropic solutions corresponding to the parameters $Re = 5$, $Fr = .01$, $(kx, ky, kz) = 2\pi(1, 1, 0)$ and where $\boldsymbol{\alpha} = \boldsymbol{e}_2$ corresponding to wave modes.

as illustrated in figure C.2 (dashed lines are solutions from the simulation and solid lines are analytic solutions). When setting $\boldsymbol{\alpha} = \boldsymbol{e}_3$. The associated eigenvalue is now $\lambda_{2,3} = -k_\perp^2/Re - i/Fr$ and the evolution of cosine and sine coefficients, respectively, are given by:

$$(\boldsymbol{a}_3\cos(\delta t) - \boldsymbol{b}_3\sin(\delta t))\exp\left(\frac{-k_\perp^2}{Re}t\right) = 2\begin{pmatrix} 0 \\ |\hat\phi|\cos(t/Fr + \theta_1) \\ Frk_\perp^2|\hat\phi|\cos(t/Fr + \theta_2) \end{pmatrix}\exp\left(\frac{-k_\perp^2}{Re}t\right)$$

$$(\boldsymbol{b}_3\cos(\delta t) + \boldsymbol{a}_3\sin(\delta t))\exp\left(\frac{-k_\perp^2}{Re}t\right) = 2\begin{pmatrix} 0 \\ |\hat\phi|\cos(t/Fr - \theta_3) \\ Frk_\perp^2|\hat\phi|\cos(t/Fr - \theta_4) \end{pmatrix}\exp\left(\frac{-k_\perp^2}{Re}t\right)$$

where $|\hat\phi| = \sqrt{\hat\phi_r^2 + \hat\phi_i^2}$, $\theta_1 = \tan^{-1}(-\hat\phi_i/\hat\phi_r)$, $\theta_2 = \tan^{-1}(\hat\phi_r/\hat\phi_i)$, $\theta_3 = \tan^{-1}(-\hat\phi_r/\hat\phi_i)$, and $\theta_4 = \tan^{-1}(\hat\phi_i/\hat\phi_r)$. When provided the initial condition $\boldsymbol{a}_3$ and $\boldsymbol{b}_3$, the code correctly tracks the analytic
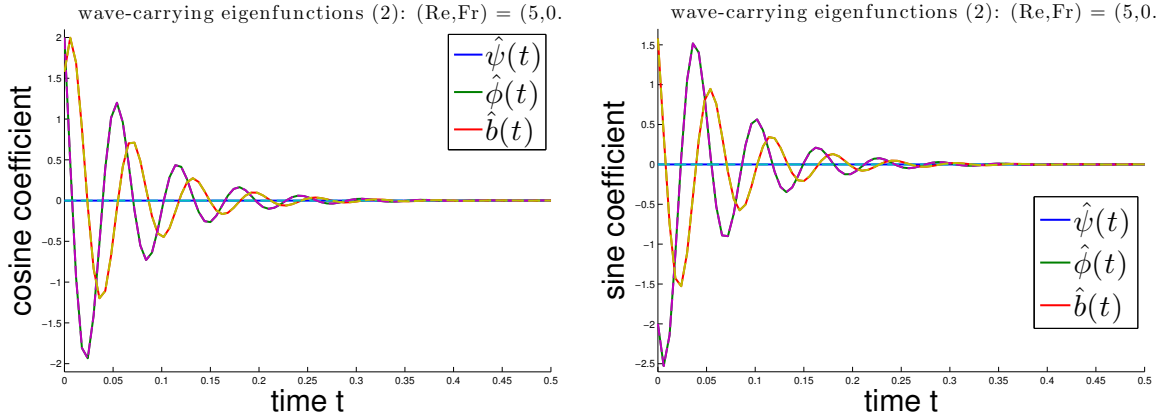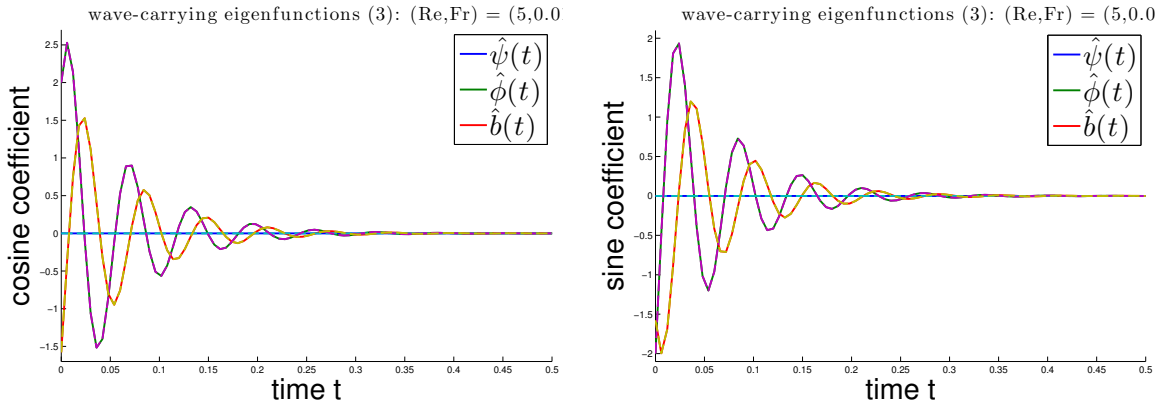

Figure C.3: Barotropic solutions corresponding to the parameters $Re = 5$, $Fr = .01$, $(kx, ky, kz) = 2\pi(1,1,0)$ and where $\boldsymbol{\alpha} = \boldsymbol{e}_3$ corresponding to wave modes.

solutions as illustrated in figure C.3 (dashed lines are solutions from simulations and solid lines are analytic solutions outlined above).

Similar results are seen for the baroclinic case and for varying values of the controlling parameters. These results validate the code. Physical space solutions have also been checked and verified against analytic solutions mentioned above (equation (C.17)). For future reference a description of how spectral-space amplitudes are handled and organized in the code is described here. In each of the Cartesian directions the sine amplitudes (b_i) and cosine amplitudes (a_i) are

organized as follows:

$$
kx : \quad \begin{pmatrix} a_0 & a_N & a_1 & b_1 & a_2 & b_2 & \ldots & a_{N_x-1} & b_{N_x-1} \end{pmatrix}
$$

$$
ky : \quad \begin{pmatrix} a_0 & a_1 & b_1 & a_2 & b_2 & a_3 & \ldots & a_{N_y-1} & b_{N_y-1} & a_{N_y} \end{pmatrix}
$$

$$
kz : \quad \begin{pmatrix} a_0 & a_1 & b_1 & a_2 & b_2 & a_3 & \ldots & a_{N_Z-1} & b_{N_Z-1} & a_{N_Z} \end{pmatrix}
$$

At a single wavenumber $\boldsymbol{k}$, the arrays that hold ψ, ϕ, and b in the code are v3, ww, and tt, respectively, and are organized in Fourier space as illustrated below:
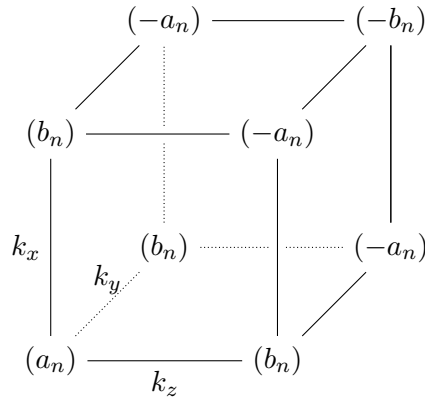
If one wishes to introduce energy into one of the field variables at wavenumber $\boldsymbol{k}$, then the sine and cosine amplitudes at $\boldsymbol{k}$ must be arranged into eight entries of the array holding that variable's Fourier space coefficients. This Fourier space structure is such that the cyclic property of $\{\sin, \cos\}$ under differentiation is preserved.

Bibliography

Hussein Aluie and Susan Kurien. Joint downscale fluxes of energy and potential enstrophy in rotating stratified boussinesq flows. Europhys. Lett., 96(4):44006, 2011.

Peter Bartello. Geostrophic adjustment and inverse cascades in rotating stratified turbulence. Journal of the Atmospheric Sciences, 52(24):4410–4428, 2015/08/07 1995.

G. K. Batchelor. Small-scale variation of convected quantities like temperature in turbulent fluid. part 1. general discussion and the case of small conductivity. J. Fluid Mech., 5:113–133, 1971.

Paul Billant and Jean-Marc Chomaz. Experimental evidence for a new instability of a vertical columnar vortex pair in a strongly stratified fluid. Journal of Fluid Mechanics, 418:167–188, 9 2000. ISSN 1469-7645.

Paul Billant and Jean-Marc Chomaz. Self-similarity of strongly stratified inviscid flows. Physics of Fluids, 13(6):1645–1651, 2001. doi: http://dx.doi.org/10.1063/1.1369125.

Guido Boffetta and Robert E Ecke. Two-dimensional turbulence. Annual Review of Fluid Mechanics, 44:427–451, 2012.

Guilhem Bordes, Frdric Moisy, Thierry Dauxois, and Pierre-Philippe Cortet. Experimental evidence of a triadic resonance of plane inertial waves in a rotating fluid. Physics of Fluids (1994-present), 24(1):014105, 2012.

B. M. Boubnov and G. S. Golitsyn. Experimental study of convective structures in rotating fluids. JFM, 167:503–531, 1986. ISSN 1469-7645.

C. J. Brownell and L. K. Su. Planar measurements of differential diffusion in turbulent jets. AIAA Paper 2004-2335, 2004.

C. J. Brownell and L. K. Su. Scale relations and spatial spectra in a differentially diffusing jet. AIAA Paper 2007-1314, 2007.

F. H. Busse. Thermal instabilities in rapidly rotating systems. Journal of Fluid Mechanics, 44: 441–460, 11 1970. ISSN 1469-7645.

Michael A. Calkins, Keith Julien, and Philippe Marti. Three-dimensional quasi-geostrophic convection in the rotating cylindrical annulus with steeply sloping endwalls. Journal of Fluid Mechanics, 732:214–244, 10 2013. ISSN 1469-7645.

Michael A. Calkins, Kevin Hale, Keith Julien, David Nieves, Derek Driggs, and Philippe Marti. The asymptotic equivalence of fixed heat flux and fixed temperature thermal boundary conditions for rapidly rotating convection. Journal of Fluid Mechanics, 784, 12 2015. ISSN 1469-7645.

Claude Cambon. Turbulence and vortex structures in rotating and stratified flows. European Journal of Mechanics - B/Fluids, 20(4):489 – 510, 2001. ISSN 0997-7546. doi: http://dx.doi.org/10.1016/S0997-7546(01)01126-8.

S. Chandrasekhar. Hydrodynamic and Hydromagnetic Stability. Oxford University Press, 1961.

Jule G. Charney. On the scale of atmospheric motions. Geofys. Publ., 17:1–17, 1948.

Jule G. Charney. Geostrophic turbulence. Journal of the Atmospheric Sciences, 28(6):1087–1095, 1971.

Dudley B. Chelton, Roland A. deSzoeke, Michael G. Schlax, Karim El Naggar, and Nicolas Siwertz. Geographical variability of the first baroclinic rossby radius of deformation. JPC, 28(433-460): 33–52, 1998. doi: http://dx.doi.org/10.1175/1520-0485(1998)028¡0433:GVOTFB¿2.0.CO;2.

C.J. Davies, D. Gubbins, and P.K. Jimack. Convection in a rotating spherical fluid shell with an imposed laterally varying thermal boundary condition. J. Fluid Mech., 641:335–358, 2009.

S. C. R. Dennis. Compact explicit finite difference approximations to the Navier–Stokes equation. In Soubbaramayer and J. P. Boujot, editors, Ninth Intl Conf. on Numerical Methods in Fluid Dynamics, volume 218 of Lecture Notes in Physics, pages 23–51. Springer, 1985.

E. T. Eady. Long waves and cyclone waves. Tellus, 1(3):33–52, 1949. ISSN 2153-3490. doi: 10.1111/j.2153-3490.1949.tb01265.x.

R. E. Ecke and J. J. Niemela. Heat transport in the geostrophic regime of rotating Rayleigh-Bénard convection. ArXiv e-prints, September 2013.

Pedro F. Embid and Andrew J. Majda. Averaging over fast gravity waves for geophysical flows with arbitrary potential vorticity. Commun. Partial Diff. Eq., 21:619–658, 1996.

Pedro F. Embid and Andrew J. Majda. Low froude number limiting dynamics for stably stratified flow with small or finite rossby numbers. Geophysical & Astrophysical Fluid Dynamics, 87(1-2): 1–50, 1998.

WJ Emery, WG Lee, and L Magaard. Geographic and seasonal distributions of brunt-väisälä frequency and rossby radii in the north pacific and north atlantic. Journal of Physical Oceanography, 14(2):294–317, 1984.

U. Frisch. Turbulence: The legacy of A. N. Kolmogorov. Cambridge University Press, 1995.

Ferran Garcia, Juan Sánchez, and Marta Net. Antisymmetric polar modes of thermal convection in rotating spherical fluid shells at high taylor numbers. Phys. Rev. Lett., 101:194501, Nov 2008. doi: 10.1103/PhysRevLett.101.194501.

T. Gerkema, J. T. F. Zimmerman, L. R. M. Maas, and H. van Haren. Geophysical and astrophysical fluid dynamics beyond the traditional approximation. Reviews of Geophysics, 46(2):n/a–n/a, 2008. ISSN 1944-9208. doi: 10.1029/2006RG000220. URL http://dx.doi.org/10.1029/2006RG000220. RG2004.

H.P. Greenspan. The Theory of Rotating Fluids. Cambridge University Press, 1968.

Ian Grooms, Keith Julien, Jeffrey B. Weiss, and Edgar Knobloch. Model of convective Taylor columns in rotating Rayleigh-Bénard convection. PRL, 104:224501, 2010.

Desmond J Higham. An algorithmic introduction to numerical simulation of stochastic differential equations. SIAM review, 43(3):525–546, 2001.

S. Horn and O. Shishkina. Toroidal and poloidal energy in rotating Rayleigh-Bénard convection. J. Fluid Mech., 762:232–255, 2015.

W. B. Hubbard, A. Burrows, and J. I. Lunine. Theory of giant planets. Annu. Rev. of Astron. and Astrophys., 40(1):103–136, 2002.

L.-S. Hwang and E. O. Tuck. On the oscillations of harbours of arbitrary shape. J. Fluid Mech., 42:447–464, 1970.

Andrew Jackson. Intense equatorial flux spots on the surface of the earth's core. Nature, 424(6950): 760–763, 08 2003.

H. Johnston and C. R. Doering. Comparison of turbulent thermal convection between conditions of constant temperature and constant flux. Phys. Rev. Lett., 102(064501), 2009.

Chris A. Jones, Andrew M. Soward, and Ali I. Mussa. The onset of thermal convection in a rapidly rotating sphere. J. Fluid Mech., 405:157–179, 2 2000. ISSN 1469-7645.

K. Julien and E. Knobloch. Fully nonlinear three-dimensional convection in a rapidly rotating layer. Phys. Fluids, 11:1469–1483, 1999.

K. Julien and E. Knobloch. Reduced models for fluid flows with strong constraints. J. Math. Phys., 48(065405), 2007.

K. Julien, S. Legg, J. C. McWilliams, and J. Werne. Rapidly rotating turbulent Rayleigh-Bénard convection. J. Fluid Mech., 322:243–273, 1996.

K. Julien, E. Knobloch, and J. Werne. A new class of equations for rotationally constrained flows. Theoretical and Computational Fluid Dynamics, 11(3-4):251–261, 1998.

K. Julien, A.M. Rubio, I. Grooms, and E. Knobloch. Statistical and physical balances in low Rossby number Rayleigh-Bénard convection. Geophys. Astrophys. Fl. Dyn., 106(4-5):392–428, 2012a.

Keith Julien, Edgar Knobloch, Ralph Milliff, and Joseph Werne. Generalized quasi-geostrophy for spatially anisotropic rotationally constrained flows. JFM, 555:233–274, 2006.

Keith Julien, Edgar Knobloch, Antonio M. Rubio, and Geoffrey M. Vasil. Heat transport in low-Rossby-number Rayleigh-Bénard convection. PRL, 109:254503, 2012b.

Y. Kimura and J. R. Herring. Energy spectra of stably stratified turbulence, pages 449–452. Springer Berlin Heidelberg, 2009.

E. M. King, S. Stellmach, J. Noir, U. Hansen, and J. M. Aurnou. Boundary layer control of rotating convection systems. Nature, 457:301–304, 2009.

E. M. King, S. Stellmach, and J. M. Aurnou. Heat transfer by rapidly rotating Rayleigh-Bénard convection. Journal of Fluid Mechanics, 691:568–582, 1 2012. ISSN 1469-7645.

Eric M. King and Jonathan M. Aurnou. Thermal evidence for Taylor columns in turbulent rotating Rayleigh-Bénard convection. Phys. Rev. E, 85:016313, 2012.

W. Koch. Resonant acoustic frequencies of flat plate cascades. J. Sound Vib., 88:233–242, 1983.

R. Kunnen. Turbulent rotating convection. Eindhoven : Technische Universiteit Eindhoven, 2008.

R. P. J. Kunnen, H. J. H Clercx, and B. J. Geurts. Heat flux intensification by vortical flow localization in rotating convection. Phys. Rev. E, 74(056306), 2006.

J.-J. Lee. Wave-induced oscillations in harbours of arbitrary geometry. J. Fluid Mech., 45:375–394, 1971.

M. Lesieur. Turbulence in Fluids. Springer, 2008.

Erik Lindborg. The energy cascade in a strongly stratified fluid. Journal of Fluid Mechanics, 550: 207–242, 3 2006. ISSN 1469-7645.

C. M. Linton and D. V. Evans. The radiation and scattering of surface waves by a vertical circular cylinder in a channel. Phil. Trans. R. Soc. Lond., 338:325–357, 1992.

Andrew J. Majda and Pedro F. Embid. Averaging over fast gravity waves for geophysical flows with unbalanced initial data. Theor. Comp. Fluid Dyn., 11:155–169, 1998.

R. Marino, P. D. Mininni, D. Rosenberg, and A. Pouquet. Inverse cascades in rotating stratified turbulence: Fast growth of large scales. Europhys. Lett., 102(4):44006, 2013.

George Marsaglia and Wai Wan Tsang. The ziggurat method for generating random variables. Journal of Statistical Software, 5(8):1–7, 2000. ISSN 1548-7660. doi: 10.18637/jss.v005.i08.

John Marshall and Friedrich Schott. Open-ocean convection: Observations, theory, and models. Rev. Geophys., 37(1):1–64, 1999. ISSN 1944-9208.

P. A. Martin. On the null-field equations for the exterior problems of acoustics. Q. J. Mech. Appl. Maths, 33:385–396, 1980.

Mark S. Miesch. Large-scale dynamics of the convection zone and tachocline. Living Reviews in Solar Physics, 2(1), 2005. doi: 10.12942/lrsp-2005-1.

P. L. Miller. Mixing in high Schmidt number turbulent jets. PhD thesis, California Institute of Technology, 1991.

M. Jeroen Molemaker, James C. McWilliams, and Xavier Capet. Balanced and unbalanced routes to dissipation in an equilibrated eady flow. Journal of Fluid Mechanics, 654:35–63, 7 2010. ISSN 1469-7645. doi: 10.1017/S0022112009993272.

P. P. Niiler and F. E. Bisshopp. On the influence of Coriolis force on onset of thermal convection. J. Fluid Mech., 22:753–761, 1965. doi: doi:10.1017/S002211206500112X.

Maxim Nikurashin and Geoffrey Vallis. A theory of deep stratification and overturning circulation in the ocean. Journal of Physical Oceanography, 41(3):485–502, 2011.

Peter Olson. Laboratory experiments on the dynamics of the core. Physics of the Earth and Planetary Interiors, 187(34):139 – 156, 2011. ISSN 0031-9201. doi: http://dx.doi.org/10.1016/j.pepi.2011.08.006. Special Issue: Planetary Magnetism, Dynamo and Dynamics.

RV Ozmidov. On the turbulent exchange in a stably stratified ocean. Atmos. Oceanic Phys, 1: 861–871, 1965.

Joseph Pedlosky. Geophysical Fluid Dynamics. Springer-Verlag New York, 1987.

Stephen B. Pope. Turbulent Flows. Cambridge University Press, 2000.

A. Pouquet and R. Marino. Geophysical turbulence and the duality of the energy flow across scales. Phys. Rev. Lett., 111:234501, Dec 2013.

Monica Pozzo, Chris Davies, David Gubbins, and Dario Alfè. Thermal and electrical conductivity of iron at earth/'s core conditions. Nature, 485(7398):355–358, 2012.

J.G. Proakis and D.G. Manolakis. Digital signal processing. Pearson Prentice Hall, 2007.

Gilbert Proctor. Atmospheric and Oceanic Fluid Dynamics. Cambridge University Press, Cambridge, U.K., 1994.

J. Proudman. On the motion of solids in a liquid possessing vorticity. Proceedings of the Royal Society of London. Series A, 92(642):408–424, 1916. doi: 10.1098/rspa.1916.0026.

Cesar B Rocha, William R Young, and Ian Grooms. On galerkin approximations of the surface active quasigeostrophic equations. Journal of Physical Oceanography, 46(1):125–139, 2016.

R. S. Rogallo. Numerical experiments in homogeneous turbulence. Technical Report 81835, NASA Tech. Mem., 1981.

Antonio M. Rubio, Keith Julien, Edgar Knobloch, and Jeffrey B. Weiss. Upscale energy transfer in three-dimensional rapidly rotating turbulent convection. Phys. Rev. Lett., 112:144501, Apr 2014.

Satoshi Sakai. The horizontal scale of rotating convection in the geostrophic regime. J. Fluid Mech., 333:85–95, 1997.

A. Sakuraba and P. H. Roberts. Generation of a strong magnetic field using uniform heat flux at the surface of the core. Nature Geoscience, 2:802–805, 2009.

A. Sakuraba and P. H. Roberts. On thermal driving of the geodynamo. In E. Petrovský et al., editor, The Earth's Magnetic Interior, IAGA Special Sopron Book Series 1, pages 117–129. Springer, 2011.

S. Schmitz and A. Tilgner. Transitions in turbulent rotating Rayleigh-Bénard convection. Geophys. Astrophys. Fluid Dyn., 104(5-6):481–489, 2010.

Amrik Sen, Pablo D Mininni, Duane Rosenberg, and Annick Pouquet. Anisotropy and nonuniversality in scaling laws of the large-scale energy spectrum in rotating turbulence. Physical Review E, 86(3):036319, 2012.

K Shafer Smith and Geoffrey K Vallis. The scales and equilibration of midocean eddies: Freely evolving flow. J. Phys. Oceanogr., 31(2):554–571, 2001.

K Shafer Smith and Geoffrey K Vallis. The scales and equilibration of midocean eddies: Forced-dissipative flow. J. Phys. Oceanogr., 32(6):1699–1720, 2002.

Leslie M Smith and Youngsuk Lee. On near resonances and symmetry breaking in forced rotating flows at moderate rossby number. Journal of Fluid Mechanics, 535:111–142, 2005.

Leslie M Smith and Fabian Waleffe. Transfer of energy to two-dimensional large scales in forced, rotating three-dimensional turbulence. Phys. Fluids, 11:1608–1622, 1999.

Leslie M. Smith and Fabian Waleffe. Generation of slow large scales in forced rotating stratified turbulence. J. Fluid Mech., 451:145–168, 1 2002. ISSN 1469-7645.

Krista M. Soderlund, Eric M. King, and Jonathan M. Aurnou. The influence of magnetic fields in planetary dynamo models. Earth and Planetary Science Letters, 333–334:9 – 20, 2012.

Philippe R Spalart, Robert D Moser, and Michael M Rogers. Spectral methods for the navier-stokes equations with one infinite and two periodic directions. Journal of Computational Physics, 96 (2):297 – 324, 1991a. ISSN 0021-9991. doi: http://dx.doi.org/10.1016/0021-9991(91)90238-G.

P.R. Spalart, R.D. Moser, and M.M. Rogers. Spectral methods for the Navier–Stokes equations with one infinite and two periodic directions. J. Comput. Phys., 96:297–324, 1991b.

Michael Sprague, Keith Julien, Edgar Knobloch, and Joseph Werne. Numerical simulation of an asymptotically reduced system for rotationally constrained convection. Journal of Fluid Mechanics, 551:141–174, 3 2006. ISSN 1469-7645.

S Stellmach, A Traxler, P Garaud, N Brummell, and T Radko. Dynamics of fingering convection. part 2 the formation of thermohaline staircases. J. Fluid Mech., 677:554–571, 2011.

S. Stellmach, M. Lischper, K. Julien, G. Vasil, J. S. Cheng, A. Ribeiro, E. M. King, and J. M. Aurnou. Approaching the asymptotic regime of rapidly rotating convection: boundary layers versus interior dynamics. Phys. Rev. Lett., 113(254501), 2014.

Jai Sukhatme and Leslie M Smith. Vortical and wave modes in 3d rotating stratified flows: random large-scale forcing. Geophys. Astrophys. Fl. Dyn., 102(5):437–455, 2008.

G. I. Taylor. Experiments on the motion of solid bodies in rotating fluids. Proceedings of the Royal Society of London. Series A, 104(725):213–218, 1923. doi: 10.1098/rspa.1923.0103.

R. Temam and D. Wirosoetisno. Stability of the slow manifold in the primitive equations. SIAM J Math. Anal., 42:427–458, 2010.

R. Temam and D. Wirosoetisno. Slow manifolds and invariant sets of the primitive equations. J. Atmo. Sci., 68:675–682, 2011.

Mary-Louise Timmermans, Chris Garrett, and Eddy Carmack. The thermohaline structure and evolution of the deep waters in the canada basin, arctic ocean. Deep Sea Research Part I: Oceanographic Research Papers, 50(10):1305–1321, 2003.

Mary-Louise Timmermans, H Melling, and Luc Rainville. Dynamics in the deep canada basin, arctic ocean, inferred by thermistor chain time series. Journal of physical oceanography, 37(4): 1066–1076, 2007.

F. Ursell. Surface waves on deep water in the presence of a submerged cylinder i. Proc. Camb. Phil. Soc., 46:141–152, 1950.

G. K. Vallis. Lectures on Solar and Planetary Dynamos. Cambridge University Press, Cambridge, U.K., 2006a.

G. K. Vallis. Atmospheric and Oceanic Fluid Dynamics. Cambridge University Press, Cambridge, U.K., 2006b.

L. J. A. van Bokhoven, H. J. H. Clercx, G. J. F. van Heijst, and R. R. Trieling. Experiments on rapidly rotating turbulent flows. Physics of Fluids (1994-present), 21(9):096601, 2009.

E. P. van der Poel, R. Ostilla-Mónico, R. Verzicco, and D. Lohse. Effect of velocity boundary conditions on the heat transfer and flow topology in two-dimensional rayleigh-bénard convection. Phys. Rev. E, 90(013017), 2014.

Hans van Haren and Claude Millot. Gyroscopic waves in the mediterranean sea. Geophysical Research Letters, 32(24), 2005. ISSN 1944-8007. doi: 10.1029/2005GL023915. L24614.

L. van Wijngaarden. On the oscillations near and at resonance in open pipes. J. Engng Maths, 2: 225–240, 1968.

Peter Vorobieff and Robert E. Ecke. Turbulent rotating convection: an experimental study. JFM, 458:191–218, 2002.

Michael L Waite and Peter Bartello. The transition from geostrophic to stratified turbulence. Journal of Fluid Mechanics, 568:89–108, 2006.

T. Warn. Statistical mechanical equilibria of the shallow water equations. Tellus A, 38A(1):1–11, 1986. ISSN 1600-0870. doi: 10.1111/j.1600-0870.1986.tb00448.x. URL http://dx.doi.org/10.1111/j.1600-0870.1986.tb00448.x.

Jared P. Whitehead and Beth A. Wingate. The influence of fast waves and fluctuations on the evolution of the dynamics on the slow manifold. Journal of Fluid Mechanics, 757:155–178, 10 2014. ISSN 1469-7645.

Beth A. Wingate, Pedro Embid, Miranda Holmes-Cerfon, and Mark A. Taylor. Low rossby limiting dynamics for stably stratified flow with finite froude number. Journal of Fluid Mechanics, 676: 546–571, 6 2011. ISSN 1469-7645. doi: 10.1017/jfm.2011.69.

M. G. Worster. The dynamics of mushy layers. In S. H. Davis, H. E. Huppert, W. Muller, and M. G. Worster, editors, In Interactive dynamics of convection and solidification, pages 113–138. Kluwer, 1992.

O Zeman. A note on the spectra and decay of rotating homogeneous turbulence. Phys. Fluids, 6 (10):3221–3223, 1994.

K. Zhang and P. H. Roberts. Thermal inertial waves in a rotating fluid layer: exact and asymptotic solutions. Phys. Fluids, 9(7):1980–1987, 1997.

K. K. Zhang and D. Gubbins. Convection in a rotating spherical fluid shell with inhomogeneous temperature boundary condition at infinite Prandtl number. J. Fluid Mech., 250:209, 1993.

Junwei Zhao, R. S. Bogart, A. G. Kosovichev, Jr. T. L. Duvall, and Thomas Hartlep. Detection of equatorward meridional flow and evidence of double-cell meridional circulation inside the sun. The Astrophysical Journal Letters, 774(2):L29, 2013.